Ph. D. DISSERTATION

Plasmonic Organic Solar Cells Employing Nanobump Assembly

나노범프 구조를 이용한 플라즈모닉
유기태양전지에 대한 연구

By

Hyung-Jun Song

February 2015

DEPARTMENT OF
ELECTRICAL AND COMPUTUER ENGINEERING
COLLEGE OF ENGINEERING
SEOUL NATIONAL UNIVERSITY

PLASMONIC ORGANIC SOLAR CELLS EMPLOYING NANOBUMP ASSEMBLY

나노범프 구조를 이용한 플라즈모닉 유기 태양전지에 대한 연구

지도교수 이 창 희

이 논문을 공학박사 학위논문으로 제출함

2015 년 2 월

서울대학교 대학원

전기컴퓨터공학부

송 형 준

송형준의 공학박사 학위논문을 인준함

2015 년 2 월

위 원 장 : _____ (인)
부위원장 : _____ (인)
위 원 : _____ (인)
위 원 : _____ (인)
위 원 : _____ (인)

Abstract

PLASMONIC ORGANIC SOLAR CELLS EMPLOYING NANOBUMP ASSEMBLY

HYUNG-JUNSONG

DEPARTMENT OF ELECTRICAL AND COMPUTER ENGINEERING
COLLEGE OF ENGINEERING

SEOUL NATIONAL UNIVERSITY

Plasmonic organic solar cells (OSCs) have attracted attention in recent years because of their superior optical properties, increasing light absorption inside the device. Plasmonic OSCs are normally consisted with small sized metallic nano particles (NPs) and structures, whose size is smaller than the wavelength of light. These nano structures lead to elongated light paths inside the active layer of OSCs and boosting electrical field near them, thereby resulting in increased light absorption and photocurrent.

For generating NPs, two different methods, the wet-based and the thermal evaporation process, have been widely used. In the case of wet based method, NPs are mixed with the solution processed buffer layer. It is very important to prevent NPs from the aggregation of each other, which works as exciton quenching sites and leakage sources, so that the careful handling for the generation and dispersion of NPs is mandatory. On the other hands, the size of thermally deposited NPs is limitedbecause of the trade-off relationship between transparent of layer and plasmonic effects. Therefore, it is imperative to introduce new method to form uniformly sized NPs without aggregation, which is much more beneficial for the fabrication ofOSC module.

In this thesis, a novel plasmonic OSC incorporating a nanobump assembly (NBA) is demonstrated. Here, the NBA is consisted of aerosol derived silver NPs covered by thermally evaporated hole extraction layer (HEL), MoO_3. The size of NPs generated evaporation and condensation method via aerosol process is precisely controlled with small deviation of their size. Additionally, the aggregation between NPs is negligible compared to the conventional NPs, synthesized by wet process. Moreover, thermally evaporated MoO_3 follows underlying structure, so that the NBA has oval shaped structure, Thus the NBA provide precisely size controlled plasmonic structure with textured surface.

In the polymer based OSC, the device performance of OSC with NBA (6.07%) shows higher power conversion efficiency compared to the device without it (5.20%). This is mainly originated to the enhancement in the photo current without deteriorating other photovoltaic parameters. Especially, the improvement in spectral response to the light at the region from 500 to 600 nm leads to the better device performance of OSC with NBA. This wavelength region is in a good agreement with calculated plasmonic effect from NBA, which is derived from 3D finite domain time

difference method. Moreover, the undulated structure arising from NBA provides better carrier transport. What's more, it is possible to tune the main peak of plasmonic effect by managing the size of NPs. As the size of NP increase, the plasmonic peak wavelength is red-shifted, with increasing the scattering intensity.

Compared to the widely used conventional method, where NPs are incorporated to the solution processed PEDOT:PSS, the NBA provides better electrical and optical effect to the device. Since the NPs are covered by oval shaped high refractive index material (n= ~ 2.0 at 550 nm), the plasmonic effect from NBA is higher and occurred at longer wavelength than that of conventional structure, NPs embedded in flat low index material, PCDOT:PSS (n= ~ 1.8 at 550 nm). Besides, fully covered NPs by dielectric layer minimize NP induced exciton annihilation, which facilitate the generation of free carrier. Furthermore, the undulated active layer allows free carrier to extract effectively to the electrode. As a result, the efficiency of OSC with NBA (6.07%) is higher than that of OSC with NPs embedded in PEDOT:PSS (5.63%), while performances of devices without NPs are similar to each other regardless of change of buffer layer (MoO_3: 5.20%, PEDOT:PSS: 5.16%).

To estimate the effect of NP's encapsulation status, electrical and optical properties of NBA is studied by changing the thickness of dielectric layer, MoO_3. The UV-visible absorption spectrum shows that the enhancement in absorption of film with partially encapsulated NPs is higher than that of film with fully encapsulated one. This can be understood by the short penetration length of plasmonic effect induced by NPs. However, the transient photoluminescence and impedance analysis illustrated that the partially encapsulated NPs work as the exciton quenching and the recombination centers, which mitigates the transfer of enhanced absorption to the photo-current. Considering these factors, the maximum

enhancement of device performance is achieved, when the thickness of MoO_3 is 20 nm for 40 nm Ag NPs. Therefore, it is mandatory for highly efficient plasmonic OSCs to employ fully covered NPs with minimum thickness of dielectric layer.

This thesis demonstrates the practical approaches to enhance power conversion efficiency of plasmonic polymer solar cells, employing nanobump assembly. Additionally, the optical and electrical effect of NBA is studied by varying the thickness of encapsulation layer and size of NP. This approach is guideline for plasmonic solar cell for organic device as well as other type one polymer-NC hybrid, dye-sensitized solar and perovskite based solar cells. And this technique can be extended to optoelectronic devices.

Keywords: Organic solar cell, Plasmonics, optical engineering, nano particles, nanobump assembly, exciton quenching, recombination losses, multi-reflection, aerosol process

Student Number: 2011-30238

Contents

List of Figures

List of Tables

Chapter 1

Introduction

Recently, there has been an enormous increase of the global energy demand due to world population growth and industrial development. Until now, the main energy source is fossil fuels, such as coal, petroleum, natural gases, and so on. It is well known that these kinds of fossil fuels emit greenhouse gases such as carbon dioxide (CO_2), when they change into electricity. Thereby, the burning of fossil fuels and extensive clearing of native forests has contributed to a 40% increase in the atmospheric concentration of carbon dioxide, from 280 to 400parts per million (ppm) in the northern hemisphere [1].Under ongoing greenhouse gas emissions, available Earth System Models project that the Earth's surface temperature could exceed historical analogs as early as 2047 affecting most ecosystems on Earth and the livelihoods of over 3 billion people worldwide.[2] The risk associated with global warming and greenhouse effect from CO_2has spurred interest in renewable energy sources such as geothermal, winds, hydropower, bio-mass, photovoltaics, and so on.

Among the renewable energy sources, the solar cell, utilizing the sun power, is

expected the most important renewable energy source owing to enormous amount of energy from the sun light (Approximately 100,000 TW). Traditionally, the sun has provided energy for practically all living creatures on earth, through the process of photosynthesis, in which plants absorb solar radiation and convert it into stored energy for growth and development. Because of this advantage, it is forecasted that the energy from the solar power grows rapidly, increasing nearly 7-fold by 2035 compared to the present status. (See Figure 1.1)Moreover, the solar energy is utilized anywhere in the earth, so that solar cells can be installed near the energy demanding places, the end-use sector, resulting in decreasing the energy losses from the transmission of electricity. Furthermore, the construction of large sized solar power plant has increased. Therefore, the research of solar cell is imperative to solve the global warming and future energy crisis.

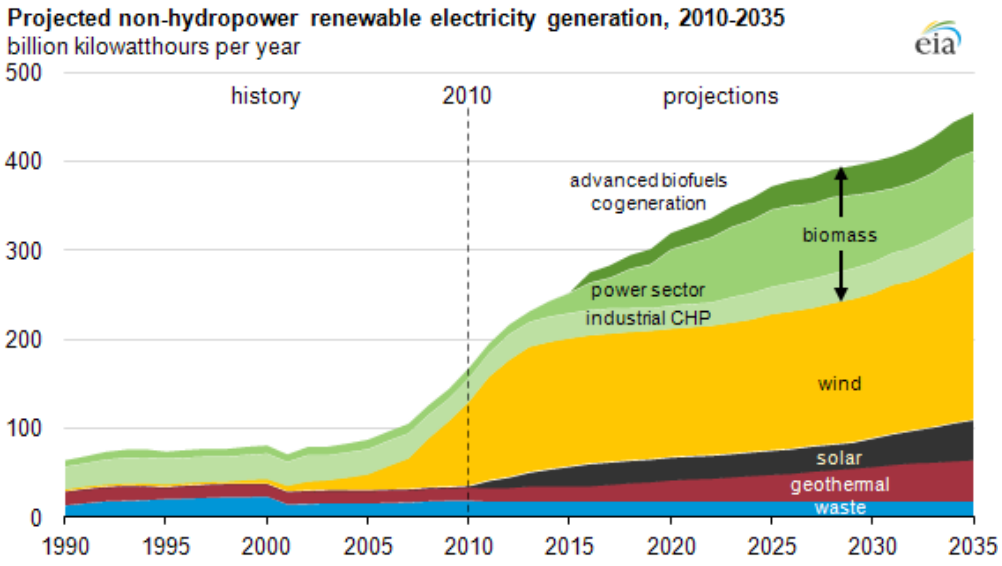

Figure 1.1 Projected non-hydropower renewable electricity generation, 2010 - 2035

(Source : U. S. Energy Information Administration (Feb 2012))

1.1 Overview of Organic Solar Cells

The solar cell, which is called as a photovoltaic cell can be categorized into three different generation, which is determined by the cost and efficiency. Figure 1.2 shows the definition of three type solar cell. [3]The 1st generation solar cell is consisted of crystalline silicon and GaAs employing p-n junction, which dominate the commercial market. These type solar cells show quiet high efficiency (~30%), which almost reaches the Shokley-Queisser limit (33.7% for single p-n junction device) [4] However, the high fabrication cost, caused by the high temperature crystalline process and purity of materials, hampers this type solar cells to compete with other energy sources. To provide a truly widespread primary energy source, solar cells must be cost-competitive with fossil based electricity at utility scale. Therefore, reducing the cost for solar cells is key factor to acquire competitive edge as an energy source. For decreasing the cost by reducing the consumption of materials, the 2nd generation solar cells based on thin film technology have been developed, which is 2nd generation solar cells. Chalcogenide based solar cell, such as Copper Indium Gallium Selenide and Copper zinc tin sulfide, as well as amorphous Si cells belong to this type of photovoltaic device. Additionally, the advantage of 2nd generation solar cells is low cost due to thin active layer, while the efficiency of them (<23%) is lower than 1st generation one.

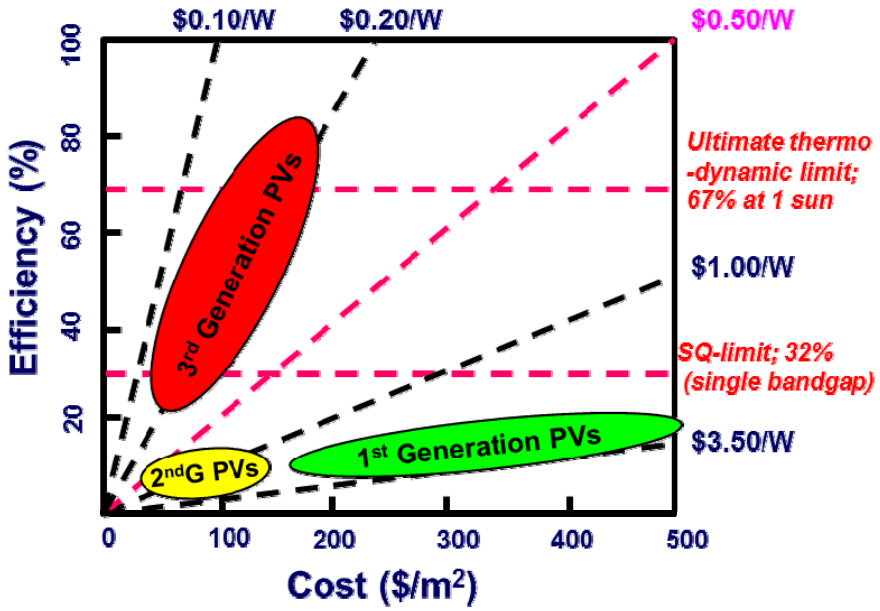

Figure 1.2 Electricity cost vs power conversion efficiency of solar cells.

(Figure was redrawn from [3])

To realize high cost-effective and efficient solar cells, technical breakthroughs are required in the point of process as well as materials. The aim of 3rd generation is to demonstrating low-cost and high efficiency solar cells. For low cost device, the solution process is needed to minimize the loss of material. In addition, the low energy consumption during the manufacturing process can be achieved in the solution process, so called truly eco-friendly energy sources. Moreover, materials for solar cell should be earth abundant ones. As a result, new emerging technologies based solar cells, have attracted considerable attention as a promising alternative 3rd generation-solar cell.

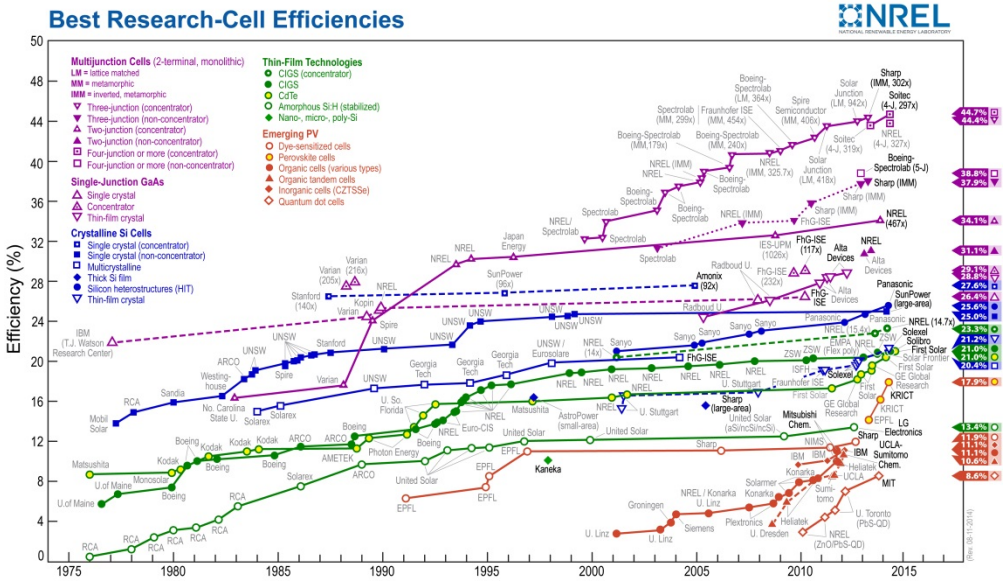

Figure 1.3 Best research solar cell efficiencies record (Source: The National Center for Photovoltaics (NCPV) at NREL)

Among these, the organic solar cell(OSC)is one of the candidate to realize 3rd generation solar cells, because of their potential for solution process at low temperature with carbon based materials. Additionally, advantages of OSC, large-scale fabrication, lightweight, and flexibility, can open a new market. [4,5,6]. Despite low efficiency of OSC, the efficiency of organic solar cell have continually increased since C. Tang introduced first bilayer solar cells as shown in Figure 1.3 [7]. Recently, the power conversion efficiency (PCE) of OSCs exceeds more than 11 %, using the bulk heterojunction tandem device [8,9]. It is expected the PCE of OSC will be reached more than 15% in a few years, which is compatible with already commercialized PVs in the market owing to low process cost of OSC. Moreover, the energy payback time of OSC (less than 0.5 year) is very short than that of others. [10] Furthermore, organic solar cell is very light, so that it can be used as an off-grid energy source for outdoor activities. Therefore, the research and development for OSC is important for demonstrating truly eco-friendly 3rd generation solar cells.

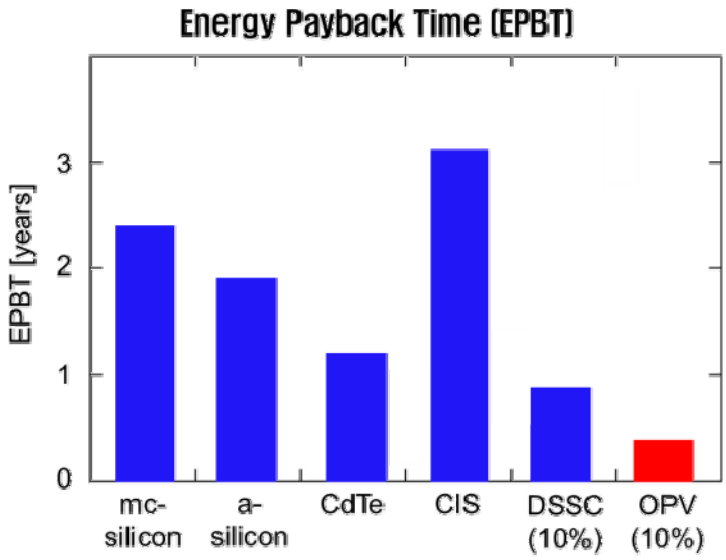

Figure 1.4 Energy pay-back time (EPBT) of different type of solar cells

(Figure was redrawn from [10])

1.2 Light Management in Organic Solar Cells

One key challenge issue for highly efficient OSC is the insufficient light absorption of active layer. This is originated from different operating mechanism of OSC in comparison to other photovoltaic energy sources, as shown in Figure 1.5[11]. In inorganic solar cells, electron-hole pairs are generated throughout the bulk in solar cells owing to high dielectric constant of the material [12]. The active-layer thickness of conventional wafer-based crystalline Si solar cells is approximately several hundreds of micrometer in order to achieve efficient light absorption and carrier generation. However, excitons, loose bounded hole-electron pairs are generated rather than free carriers, when the light is irritated into organic films, owing to low dielectric constant, increased columbic force between electron and holes. The diffusion length of these photo-generated excitons is ~10 nm in organic semiconducting films [13, 14]. Additionally, the donor-acceptor interface is the place where these excitons only dissociate into free holes and electrons.[15].As a result, OSC is generally consisted of bulk heterojunction of donor and acceptors, which enlarge the interface between two materials for charge generation. However, the islands of donor and acceptor molecules inside bulk heterojunction, where the generated holes and electrons do not move to the electrode, works as recombination centers. Besides, electron and holes move to the electrode by hopping in organic films, which increase electrical losses during the transport process [16].Recognizing, carrier generation and transport in OSCs, the thickness of the active layer is limited less than ~300nm, which causes insufficient light absorption. Hence, the effective

light management for increasing the absorption of the incident sunlight is essential for highly efficient OSCs.

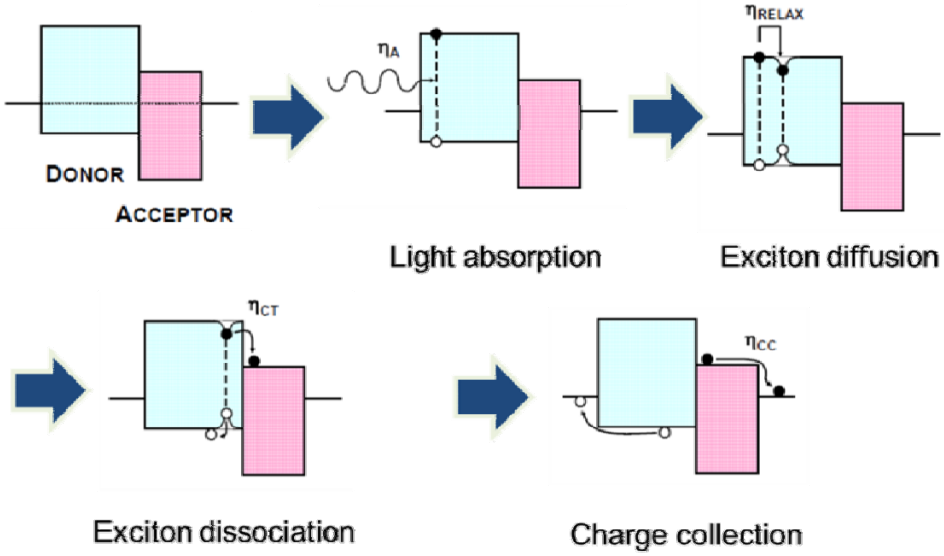

Figure 1.5 Working principle of organic solar cells

Various strategies for harvesting more light in in the active layer of OSC have been suggested during the last decade, such as surface texturing, photonic crystals, and lens array [17, 18]. By the diffraction, interference, and lens effect from the structures, the incident light can be concentrated into the active layer, thereby the generation of photo-current increase, which leads to higher efficiency of device. However, in these methods, the structure should be smaller than the wavelength of sunlight in the visible and near-infrared (NIR) spectral regions. For satisfy this requirements, high resolution E-beam photo-lithography process is mandatory, which increases manufacturing cost. However, the substrate size for E-beam photo-lithography is much smaller than that of solar cell module. Consequently,

researchers have been working hard to develop new strategies that can be easily adopted in thin film devices.

1.3 Plasmonic Organic Solar Cells

Plasmonics, the interaction between metallic film and nanoparticles (NPs), is a very interesting technology to modify the local electric field density ($|E|^2$). When the incident light irradiates the metallic structure, smaller than the wavelength of the light, the electric polarization of free carrier, hole and electron, is occurred. This polarization leads to the change of local $|E|^2$at the resonance wavelength. According to the H.A. Atwater and A. Poleman, three methods to increase light intensity inside thin film solar cell using plasmonic effects have been suggested [19]. The plasmonic effects can be categorized three ways: scattering, localized surface plasmons, and surface plasmon polaritons. The research progress in OSC using plasmonic effect has also been reported which increases the PCE significantly, as shown in Figure 1.6.The two main types of patterned nanostructures frequently used to introduce plasmonic enhancement in OSCs are metallic nanoparticles, and 1D and 2D periodic nano-patterned array, as shown in Figure 1.7[11].

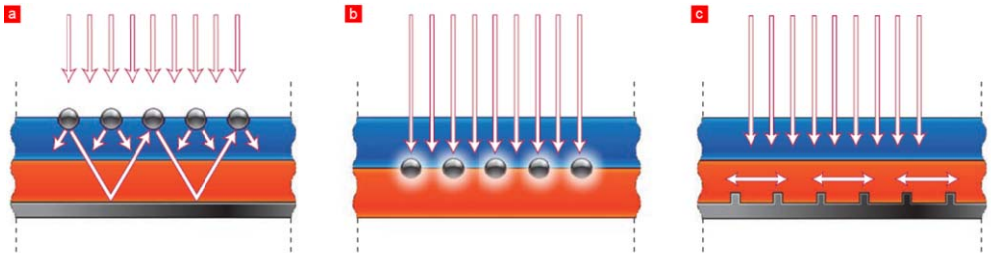

Figure 1.6 Light management methods for thin film solar cells:a) Scattering from nanoparticles, b) Localized surface plasmons of nanoparticles, and c) surface plasmon polaritons from nanostructure. (Figure was redrawn from [19])

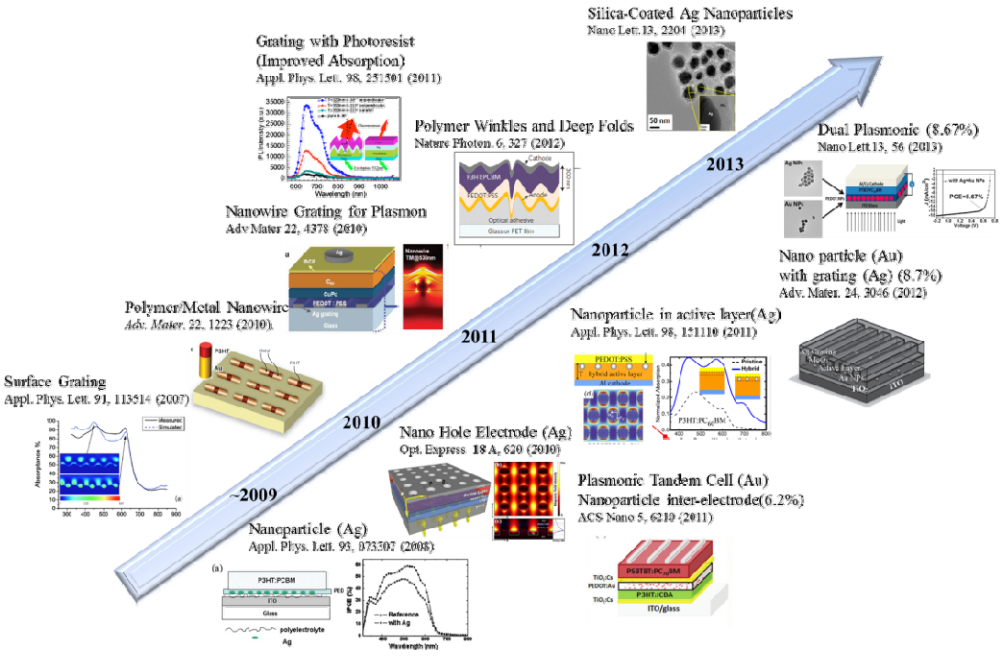

Figure 1.7 Recent progress of plasmonic OSC with nanoparticles and periodic structure

1.3.1 Plasmonic OSC with nanoparticles

Due to the ease process of Metallic NPs, OSC devices with them are probably the most popular and widely used for improving the efficiency. Since the resonance wavelength of plasmonic effect can be tuned as controlling materials, concentrations, shapes, sizes, distributions, etc, metallic NPs have been introduced in various layers and interfaces within the OSCs. Here, the NPs are generally located on the active layer or buffer layers, as shown in Figure 1.8. First, NPs have been inside the buffer layer of OSCs by vapor phase deposition, electro-deposition, thermal annealing, and chemical synthesis [20-22].Here, NPs are surrounded by the polymer or insulating layer to reduce the electrical side effects arose from inserting them into active layer. Moreover, the carrier extraction efficiency increased by the inserting of NPs owing to high mobility of metallic NPs as well as the band alignment between active layer and buffer layer[23,24].However, the distance between the NPs and active layer is farther than effective resonance length of localized surface plasmon (~10 nm). As a result, the enhancement in the device performance is mainly originated from scattering effect as well as enhanced carrier extraction. On the other hand, NPs in active layer allows us to utilize localized surface plasmon resonance, which increase the absorption of active layer. But, the encapsulation of NPs is very important issue to transfer increased absorption to energy harvesting. Despite the pros and cons of both cases, there has been reported that the incorporation of NPs to OSC leads to the enhancement in the efficiency by increasing light absorption at the specific wavelength of light and extracting more carrier to electrode with small losses.

Table1.1 summarizes the previous reported results of enhancing the performance of OSCs with NPs in active layer and buffer layer. In both cases, the size of NPs are in the range of 10 to 100nm, considering the thickness of OSCs and extinction/scattering ratio of metallic NPs. Here metallic NPs are generally consisted of Ag, Au, and Cu. Regardless the active layer, the efficiency of OSC with NPs increase approximately 20% compared to that of device without NPs. Moreover, the improvement in device performance of OSC was reported in the device with tandem structure and fully vacuum deposited one [25,27]. Recently, the enhancement in light management by applying NPs to active as well as buffer layer led to dual plasmonic effect.

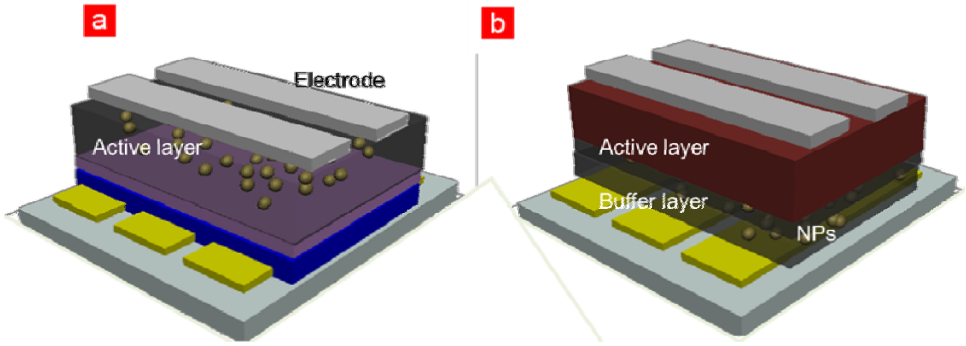

Figure 1.8 Plasmonic OSC with nanoparticles located in a) the active and b) buffer layer of devices.

Table 1.1 Selected device performance of plasmonic OSCs with NPs

Nanoparticles		Active layer	Efficiency (%)		Enhancement ratio (%)	Ref
			w/o NPs	NPs		
Buffer layer	40 nm Au	P3HT:PCBM	3.5	4.2	20	[24]
	60 nm Ag	P3HT:PCBM	1.7	2.8	64	[26]
	70 nm Au	Tandem (P3HT:IPCA &PSBTBT:PCBM)	5.2	6.2	19	[25]
	13 nm Ag	P3HT:PCBM	3.0	3.6	20	[21]
	10nm Ag	ZnPC: C60	2.7	3.5	30	[27]
	20nm Au	PTB7:PCBM	8.0	8.7	10	[28]
	25nm Au & 25nm Cu	P3HT:PCBM	3.0	3.4	14	[29]
	40 nm Au & 40nm Ag	PTB7:PCBM	7.3	8.7	20	[30]
Active layer	40nm Ag	PCDTBT :PCBM	5.6	6.5	16	[31]
	70nm Au	PCDTBT :PCBM	6.3	7.1	13	[32]
	110nm Ag	P3HT:PCBM	3.5	3.9	18	[33]

	40nm Ag	PCDTBT: PCBM	6.0	6.4	8	[34]
	50nm Au	PBDTT-DPP:PCBM	4.9	5.6	15	[35]
Combination	18nm Au (buffer) & 35 nm Au (active layer)	P3HT:PCBM	3.3	3.9	22	[36]
	50nm Ag (Buffer & active layer)	PTB7:PCBM	7.5	8.9	20	[37]

1.3.2 Plasmonic OSC with nanostructure

Although the inserting NPs into OSCs is very simple process, the careful handling for NPs is required to control their size, and distribution. The other suggested approach to enhance the light harvest in the OSCs is employing periodically patterned nanostructures. This approach enables the light to interact with the nano-structure, so called surface plasmonic polaritons, which strongly confine the light at the interface of metal and organic layer. Additionally, the diffraction induced by patterned structure provides scattering effect, which elongated light paths inside active layer. Hence, periodic nanostructures have been explored in various OSC designs to achieve unique and remarkable features.

The well-known approach is using 1Dmetallic nano-gratings which are applied to the anodes, [38]back reflector cathodes. Here, the resonance wavelength of the plasmonic effect can be tuned by controlling the period of structure from visible to

near infrared range. Recently, periodic cathode with grating nanostructures fabricated by soft-lithography was suggested. According to the report, the improvement of efficiency, from 7.2% to 7.73%, was achieved in inverted type solar cell with low band gap polymer [39]. The external quantum efficiency of this report indicated that the enhancement was originated from the waveguide modes and plasmonic effects. Moreover, it is clear that the enlarged interface between active layer and electrodes lead to better carrier transport, which decrease carrier losses and series resistance [40].Not only the plasmonic effect from cathode layer, but also optical enhancement from buffer layer and anodes were also presented[41].

For overcoming the polarization dependence of the 1D nanostructures, which differentiate the light-trapping behavior for transverse electric and magnetic modes, 2D plasmonic structures have been also suggested [42,43]. The optical and experimental result showed that the implication of 2D structure leads to polarization independence, broadband absorption enhancement in polymer and small molecule based OSCs. Besides, the combination of nanostructure and NPs in OSCs has been reported, which increase light absorption from surface plasmon polaritons as well as localized surface plasmon resonance [44].

Despite the potential benefits of plasmonic light trapping from nano structure discussed in the above, the realization of plasmonic effect in OSC is very difficult for the following reason. First, the over-fill of polymer in thin structure decreases the optical effect of it due to flat active layer [17]. Moreover, the leakage current induced by thick structure is sometimes caused by under fill and air gaps in active layer. So the thickness of structure should be lower than that of the active layer, which hampers the various plasmonic effects in OSCs. Lastly, the structure is generally fabricated by e-beam process, which raises manufacturing cost and limits the size of device.

Meanwhile, in the plasmonic OSC with NPs, it is very difficult to control the size of NPs from wet synthesis method. Besides, the dispersion of NPs in solution layer is a very challenging issue, since NPs are tend to aggregate each other. For overcoming this problem, the surfactant for NPs are introduced, however, which increase contamination of layer and decrease plasmonic effect. Moreover, the refractive indices (n) of surfactant and encapsulating layer (i.e. n of SiO_2 =1.5) is smaller than that of active layer (n= 1.8). This discrepancy confines plasmonic effect within the NPs. Therefore, it is imperative to find new approaches and fabrication methods for plasmonic OSCs with low cost and suitable for mass production.

1.4 Outline of Thesis

This thesis consists of five chapters including **Introduction** and **Conclusion**. In **Chapter 1**, the brief overview of OSCs and the previously suggested light management methods are provided. In addition, the current research status of plasmonic solar cells is reviewed. In **Chapter 2,** basic theory for plasmonic and organic solar cells is described. Furthermore, the experimental setup, the device characterization and analysis methods are introduced. In **Chapter 3**, the method for demonstrating plasmonic organic solar cells is suggested by employing nanobump assembly (NBA) which is consisted of metallic nanoparticles generated aerosol method and thermally evaporated molybdenum oxide. And then, the device performance of OSC with NBA compared with the device with conventional wet-based plasmonic structure in the view of optical and electrical properties. Moreover, the effect of nano particle's size on the device is studied. In **Chapter 4**, the carrier dynamics and optical effect of nanoparticles are investigated in the plasmonic OSC implementing NBA with different thickness of buffer layer. The electrical properties of devices are studied by impedance and equivalent circuit model, while the optical characteristics are analyzed by absorption and photoluminescence. Finally, In **Chapter 5**our studies are summarized and concluding remarks of this thesis are highlighted.

Chapter 2

Theory and Experimental Methods

2.1 Principles of plasmonic effect

2.1.1 Scattering

The scattering is a general physical process when the light collides with other particles, which change the path of straight direction to random direction in the medium. This can be happened where light irritated to the nanoparticles and obliquely radiate the metal film, so called diffuse reflections. Scattering of electromagnetic waves, light, are one of the widely known phenomenon. The scattering between light and NPs can be categorized into three sections, depending on the size of NPs. First one is geometric scattering (size of NP >> wavelength of incident light) when the light interacts with micro scale particles. The other major forms of elastic light scattering are Rayleigh scattering (size of NP < wavelength of incident light) and Mie scattering (size of NP ≈ wavelength of incident light), which occur when the size of NPs are comparable to the wavelength of light. Here, resonant light scattering in nanoparticles can produce many different highly saturated and vibrant hues, especially when surface plasmon resonance is

involved[45]. Due to thin thickness of OSC, smaller than several hundreds of nanometer, the Rayleigh scattering is main source to increase absorption of light harvesting organic materials.

Rayleigh scattering, which is generally shown in OSC with NPs, is a process in which light is scattered by a small spherical volume of metal and dielectric material, whose refractive index is different from that of surrounding media. This model is only valid in the NPs whose diameter is smaller than the wavelength (λ) of the scattered wave (1/10 of the wavelength). In visible light, the size of NPs for Rayleigh scattering is from few nanometers to 80 nm, which is one-tenth of red light. Along with absorption, such scattering is a major cause of the attenuation of radiation by the atmosphere. The intensity of scattering varies depending on the ratio of the NP's size to the wavelength of the light. Besides, polarization of light and surrounding media plays an important role to determine the scattering effect.

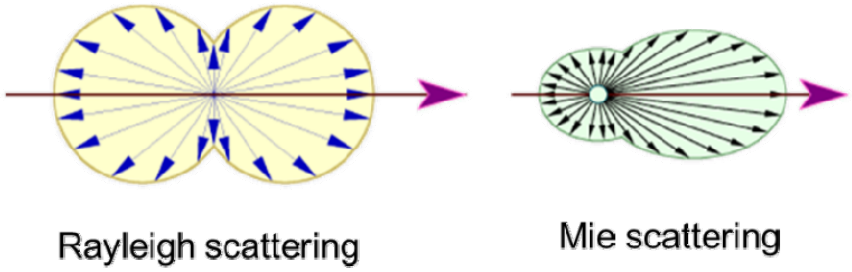

Figure 2.1 Electrical field patterns of Rayleigh and Mie scattering.

For large size NPs (~100 nm), Mie showed the range of scattering by large particles is larger than that of the Rayleigh effect [46]. This phenomenon is called as Mie scattering. The direction of scattering can be changed to the spheroids and

ellipsoids shape by changing the media in this type of scattering. By the modification of the scattering direction, it will be possible to concentrate more light inside active layer.

In summary, the Mie and Rayleigh scattering are generally occurred when sub hundred nanometer sized NPs are incorporated in dielectric materials. And this scattering effect change the directionality of incident light, which elongated light paths inside the active layer. This increased beam path allows organic molecule to harvest more light owing to increased possibility to excite molecules. Therefore, the scattering effect from NPs is one of ways to improve light absorption in OSCs.

2.1.2 Localized surface plasmon resonance

Noble metallic NPs are known to exhibit a strong absorption band in the visible light, which overlap with the optical absorption band of the organic materials for the active layer of OSCs. When the oscillation of the free electrons in NPs is matched with an incident light, the intensity of local electric field can be enhanced. This is called as a localized surface plasmon resonance (LSPR). Figure 2.1 illustrates the origin of LSPR in the media with NPs. Aforementioned the resonance peak of LSPR can be solved by the Mie theory, when the NP size is shorter than the wavelength of incident light[46]. This is a model consists of the rigorous resolution of Maxwell's equation by taking both the electromagnetic field diminished in NPs and the field scattered by the NPs into account. The extinction coefficient σ(ω), "absorption-scattering cross-section", is calculated by following equation [47]

$$\sigma(\omega) = \frac{9N\omega V\varepsilon_m^{\frac{3}{2}}}{c}\left(\frac{\varepsilon_2(\omega)}{|\varepsilon_1(\omega)+2\varepsilon_m(\omega)|^2+\varepsilon_2^2(\omega)}\right) \quad (2.1)$$

where $\omega=2\pi/\lambda$ is the pulsation of the incident electromagnetic field, c the speed of light, V the volume of single NP, N the density of NPs. And the ε_s, ε_1, ε_2 and ε_m, are the dielectric constant of the surrounding medium, the real part of metal, the imaginary part of metal, and combination of two components ($\varepsilon_m=\varepsilon_1+i\varepsilon_2$), respectively. According to Eq. (2.1), scattering intensity is maximized, when $[(\varepsilon_1(\omega)+2\varepsilon_s(\omega))^2+\varepsilon_2^2(\omega)]$ is zero. This condition is called the localized surface plasmon resonance. Generally, ε_1^2 is much higher than ε_2^2in Ag, the localized plasmon resonance wavelength of a layer integrating NPs occurs $\varepsilon_1(\omega)=-2\varepsilon_s(\omega)$. From this method, the resonance wavelength of NPs can be easily derived. Therefore, the peak of localized surface plasmon resonance can be tuned by changing the material of NPs and surrounding media.

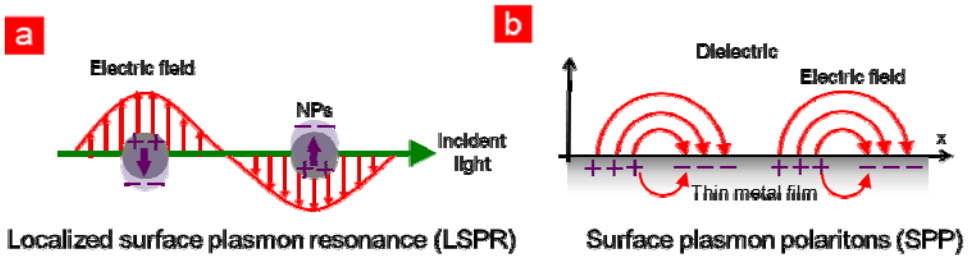

Figure 2.2 Schematic of the plasmon effect of NPs.

It has been already explored that the peak of resonance from NPs surrounded by high ε_s is longer than that enclosed by low ε_s. Additionally, the LSPR frequency depends on the size and shape of the NP, and the NP material. [48] In the case of small sized NP (5-20 nm) the absorption form NPs dominates, while relatively

larger diameter (>50 nm) NPs behave as effective scattering elements[49]. Thus, it is expected that small sized NPs works as antennas, which increase localized electrical field arose from LSPR effect. For effective light absorption, this LSPR should couple with an absorption band of active layer. On contrast, the scattering effect in relative large sized NPs channeled into improved absorption inside active layer of OSCs. In this case, enhanced absorption takes place by an increase of the optical path length inside the photoactive layer, caused by the light being reemitted in different directions with in the device.

2.2 Principles of organic solar cells

2.2.1 Solar Cell Performance Parameters

The solar cell performance can be characterized by current density-voltage(J-V) curve under illumination of a light source. The main parameters to describe the photovoltaic behaviors are maximum power conversion efficiency (PCE), open-circuit voltage (V_{OC}), short circuit current density (J_{SC}), and fill factor (FF). The value of each parameter in J-V curve is shown in Figure 2.3

The short circuit current density (J_{SC}) is the current of device under illumination, when external field is not applied (V = 0 V). The J_{SC} is determined by how many carriers are generated and extracted. It means that J_{SC} is related to optical and electrical properties of organic solar cell. In the optical respect, J_{SC} reflects the amount of light absorption, which is determined by the band gap, absorption spectra, of materials. The other factors to determine J_{SC} is the electrical properties of OSC such as mobility, donor/acceptor phase separation, charge carrier transport, recombination, and collection. Moreover, built in potential and ohmic contact between buffer layer and electrode is one of key factors for J_{SC}. Therefore, in order to achieve high J_{SC}, optical as well as electrical properties should be improved.

The open circuit voltage (V_{OC}) is the voltage where the current is zero. In this point, the amount of injected carriers is the same as the amount of photo generated carriers, so that no current flows through the external circuit. For organic solar cell device, V_{OC} can be estimated by the gap between the highest occupied molecular

orbit (HOMO) of donor and the lowest unoccupied molecular orbit of accepter. The gap between two materials is smaller than 1.5eV for sufficient light absorption spectra, so the V_{OC} of OSC is limited. Additionally, the loss of V_{OC} is happened during the exciton dissociation, approximately 0.3 eV [50]. Moreover, traps and recombination losses decrease V_{OC}. Hence the V_{OC} of OSC is generally less than 1.2 V and the controlling of electrical properties of OSC is needed to gain high V_{OC}.

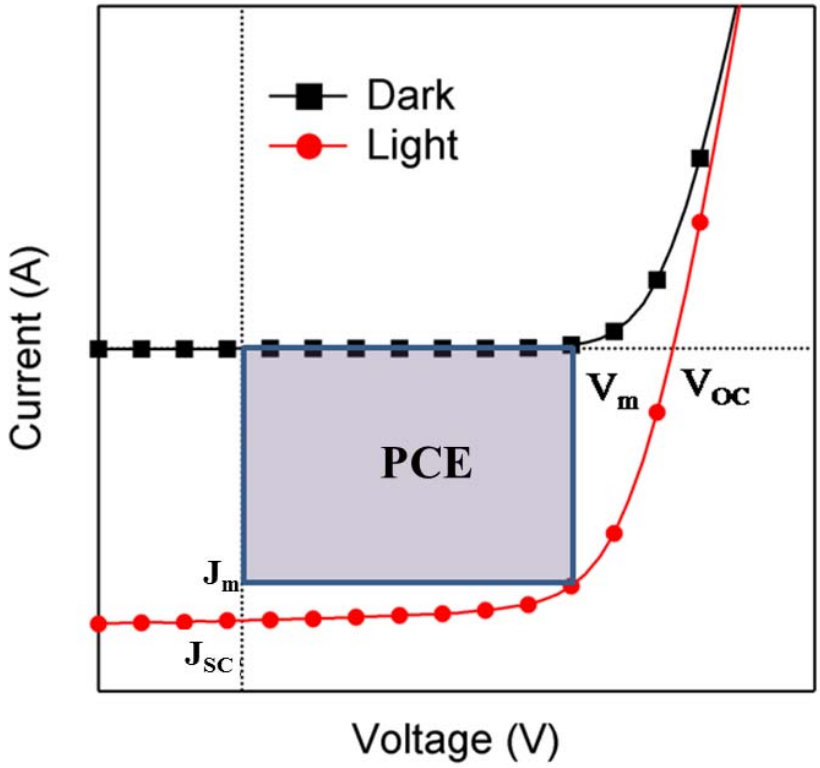

Figure 2.3 Current density-voltage (J-V) curve of organic solar cell.

The maximum power point is the point where the multiplication of current density and voltage is maximized, as shown in Figure 2.3. The maximum power point is the same as the PCE of OSCs.

The last parameters to denote OSC performance is FF. FF is the ratio between PCE and the product of open circuit voltage (V_{OC}) and short circuit current density (J_{SC}). The FF is described by the following equation:

$$FF = \frac{J_{max} \times V_{max}}{J_{SC} \times V_{OC}} \tag{2.2}$$

Where, J_{MAX} and V_{MAX} is the current density and voltage in the point of PC, respectively. In the ideal cases, the FF reaches 1, since all the generated carriers are extracted without losses and the leakage current inside device is perfectly blocked. On the other hand, if there is no diode characteristic in OPVs, the FF will be around 0.25. It means that FF is the index to measure the carrier losses inside device. In OSC with high FF, generated carriers are swept-out to the electrode with small losses, while the most of generated carriers are recombined at the device with low FF. Therefore, it is imperative to high FF for high efficient devices.

As a result, the PCE can be expressed following equation:

$$PCE\ (\%) = \frac{Electric\ Power}{Light\ Power} = \frac{J_{sc} \times V_{oc} \times FF}{P_{light}} \times 100\ (\%) \tag{2.3}$$

.

Meanwhile, the spectral response of each wavelength can be characterized by the incident photon conversion efficiency (IPCE).This value denotes the ratio ofthe number of electrons in external circuit to the number of incident photons at a

specific wavelength. Here, IPCE is generally measured at no external field. IPCE is determined by following equation:

$$EQE(\%) = \frac{n_{electron}}{n_{photons}} = \frac{J_{SC}(\lambda)/e}{P_{in}(\lambda)/(hc/\lambda)} = \frac{J_{SC}(\lambda)hc}{P_{in}(\lambda)e\lambda} \quad (2.4)$$

Where λ is the wavelength, e is the charge, h is the Planck constant and c is the speed of light in vacuum. The measured IPCE reflects the J_{SC} of devices. Additionally, this value points out the spectral response of device, which reveals that the plasmonic effect from NPs. Supposed that, the plasmonic resonance of NPs is 500 nm, then the IPCE of the device at 500 nm will increase compared to that of the device without NPs.

2.2.2 Equivalent circuit model for OSC

The OSC can be analyzed by an equivalent circuit model, which is consisted of current source, diode, series (R_S) and shunt resistance (R_{SH}) (Figure 2.). [51]. Here, R_S describe the loss during the carrier transport, while R_{SH} denotes the losses from leakage. According to the model, the current density of OSC (J) under illumination is the sum of three current sources: dark diode (J_{diode}), leakage (J_{leak}), and photo current density (J_{ph}) (See equation 2.5)

$$J = J_{diode} + J_{leak} - J_{ph} \quad (2.5)$$

Here, the voltage of OSC (V) can be expressed as

$$V = J_{leak} R_{Sh} + JR_S \tag{2.6}$$

Replacing J_{leak} with R_{SH}, R_S, and V terms, the total current is

$$J = J_0 \left[e^{\frac{q}{nk_BT}(V - JR_S)} - 1 \right] + \frac{V - JR_S}{R_{Sh}} - J_{ph} \tag{2.7}$$

Hence, the low R_S and high R_{SH} is essential to realize high PCE of OSC.

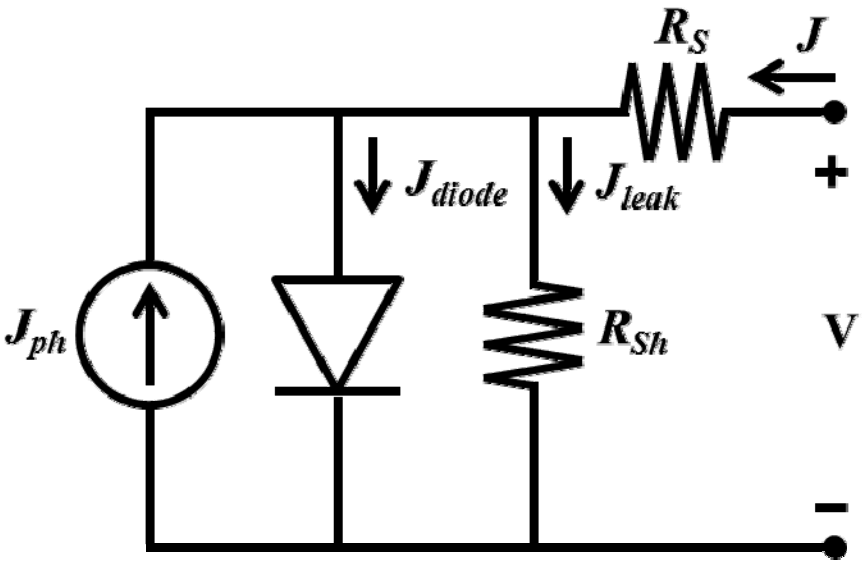

Figure 2.4 Equivalent circuit diagram of solar cell.

2.2.3 Light intensity dependence of OSC

The V_{OC} of OSC is determined by the energy level difference of donor and acceptor. In addition this value is affected by internal losses of carrier during the transport. Considering this factors, an approach based on metal-insulator-metal pictures, to calculate the recombination characteristics of OSC, was suggested by L. J. A. Kosteret al [52]. In this model, the OSC is described as one semiconducting material, whose HOMO level is the same as that of donor and the LUMO level is the same as that of acceptor, which is sandwiched by two electrodes. The number of hole and electron carriers under illumination (n, p) is described

$$n = n_{int}\exp[-\frac{q(V-\varphi_n)}{KT}] \tag{2.8}$$

$$p = n_{int}\exp[-\frac{q(V-\varphi_p)}{KT}] \tag{2.9}$$

Where, n_{int} is the intrinsic of holes and electrons, φ_n, φ_p are the quasi-fermi levels, and K is Boltzman's constant. Using the effective density of states (N_C) and energy gap of material (E_{gap}), n_{int} is

$$n_{int} = N_c\exp[-\frac{E_{gap}}{2KT}] \tag{2.10}$$

According to mass action law in equilibrium [53],$np=n_{int}^2$,the np can be expressed

$$np = n_{int}^2 \exp\left[\frac{qV_{oc}}{KT}\right] \tag{2.11}$$

Since the V_{OC} is equal to φ_p -φ_n. The current in OSC is the sum of drift and diffusion in the external field, where is in the quasi Fermi level. So the equation for current is

$$J_{n(p)} = -q\mu_{n(p)}\, n(p) \frac{\delta}{\delta x}\varphi_{n(p)} \tag{2.12}$$

Here, the continuity equation for electrons and holes can be expressed using the dissociation probability of excitons(P), generation rate of excitons (G), and the Langevin recombination rate of free electrons (R),

$$\frac{1}{q}\frac{\delta}{\delta x}J_n = PG - (1-P)R \tag{2.13}$$

By introducing Langevin recombination constant (γ), the equation 2.13 is derived as

$$G = \gamma np(1-F)/F \tag{2.14}$$

Therefore, the V_{OC} of OSC is

$$V_{oc} = \frac{E_{GAP}}{q} - \frac{KT}{q}\ln\left(\frac{(1-P)\gamma N_c^2}{PG}\right) \tag{2.15}$$

In this equation, P is independent on the light intensity, while G is dependent on the light. So the equation predicts the slope of V_{OC} versus light intensity(S). The S of OSC with small recombination losses is typically ~1, while the S of OSC increases as the trap-assisted recombination increases inside device. Therefore, the recombination behavior of device is derived by measuring the slope of V_{OC}.

2.2.4 Impedance spectroscopy analysis for OSC

Impedance spectroscopy is an analysis system to measure the electrical properties of devices. By applying the ac/dc voltage in device with different frequency, it is possible to calculate the number of carriers inside devices. In the p-n diode based on metal-insulator-metal model [53],the width of depletion region can be calculated as following equation

$$W = \sqrt{\frac{2\varepsilon_s}{q} V_{bi} \left(\frac{N_A + N_D}{N_A N_D}\right)} \approx \sqrt{\frac{2\varepsilon_s V_{bi}}{q N_D}} \qquad (2.15)$$

Where ε_s is dielectric constant of material, V_{bi} is built-in potential between p-n type diode. The number of donor (N_D) and acceptor (N_A) are possible to predict, if one know the length of depletion region. In inorganic semiconductor model, there are only space charges inside the depletion region, where no mobile charge exists. This is similar to the bulk heterojunction organic semiconductor, where the carrier transport is defined by the space-charge limited model. Here, the width of depletion region for equation 2.15 for OSC is the same as the device thickness. Thus, the number of carriers in OSC is possible to calculate.

Since the capacitance (C) of device is the product of thickness and dielectric constant, the C of OSC at specific frequency is

$$C = \frac{\varepsilon_S}{W} = \sqrt{\frac{q\varepsilon_S N_D}{2(V_{bi}-V)}}, \quad \frac{1}{c^2} = \frac{2(V_{bi}-V)}{q\varepsilon_S N_D} \tag{2.16}$$

Under the electrical field, applied voltage is V, it is possible to calculate the capacitance. This equation shows that the capacitance of device is maximized when the applied voltage is the same as built-in potential. Under the AC current, the capacitance of device is changed as the voltage is varied. In that case the number of carrier can be derived by differentiating the capacitance value to the voltage as following equation

$$N_D = \frac{2}{q\varepsilon_S}\left[-\frac{1}{\frac{d\left(\frac{1}{c^2}\right)}{dV}}\right] \tag{2.17}$$

Thus, the number of carrier is defined the inverse proportion to the ratio of $(1/c^2)$ to the applied voltage in the organic device. In the OSC, the number of carrier is determined by three factors: photo-generation, injection from electrode, and recombination losses during transport. If we measured C-V characteristics under dark condition, where the photo-generated carrier is negligible, the decreased number of carrier caused by recombination losses can be estimated.

2.3 Device fabrication method

2.3.1 Materials

Figure 2.5 show the used materials of photoactive organic materials in this thesis.

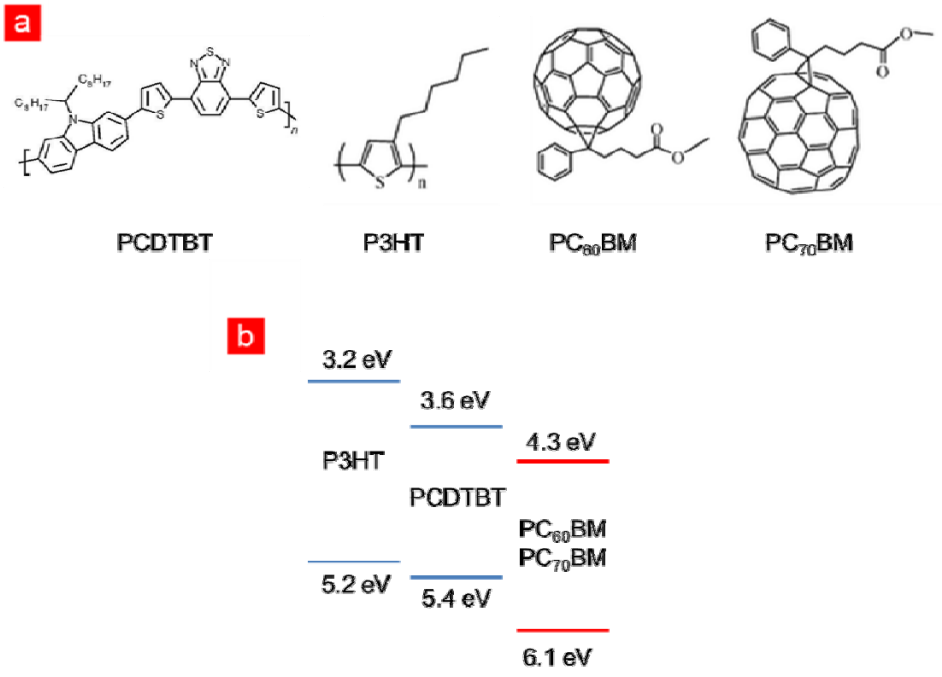

Figure 2.5 Chemical structure and energy diagram of used materials.

The mixture ofPoly[[9-(1-octylnonyl)-9H-carbazole-2,7-diyl]-2,5-thiophenediyl-2,1,3-benzothiadiazole-4,7-diyl-2,5-thiophenediyl] (PCDTBT): ([6,6]-phenyl C_{70}-butyric acid methyl ester ($PC_{70}BM$)is widely used as an active layer of OSC , which absorbs light from 300 nm to 750 nm. And the other polymer blend of Poly(3-

hexylthiophene-2,5-diyl) (P3HT): ([6,6]-phenyl C_{60}-butyric acid methyl ester ($PC_{60}BM$) is also used as photo harvesting layer. Here, the PCDTBT and P3HTwork as donor, while the fullerene based materials $PC_{70}BM$ and $PC_{60}BM$ show good electron accepting properties in bulk hetero junction layer. The energy level of each material is shown in Figure 2.5 [54,55]. All polymers were used as purchased without any purification. These polymer are used as active layer of OSC in the chapter 3,4.

Two different p-type buffer layer were used to implement Ag NP in OSCs. One is vacuum deposited molybdenum oxide (MoO_3) and the other is solution based Poly(3,4-ethylenedioxythiophene) Polystyrene sulfonate (PEDOT:PSS). The work function of each materials (MoO_3: 5.4eV, PEDOT:PSS: 5.2 eV) is laid between the work function of electrode (ITO, 4.8eV) and the HOMO of active layer, which facilitates hole extraction. In this reason, $MoO_3$and PEDOT:PSS are used as a hole transport layer in the OSCs in this chapter 3 and 4.

2.3.2 Device structure

The OSCs were fabricated on a cleaned ITO-coated glass substrate with a sheet resistance of 20 Ω/cm^2. The ITO glass substrates were pre-cleaned with acetone for 15 min and isopropyl alcohol for 15 min and were dried in a vacuum oven. And then, the ITO substrates were treated with UV-ozone. The Ag NPs were deposited on the ITO using the evaporation and condensation method in the nitrogen globe box. After that these NPs are covered by solution based PEDOT:PSS and thermally evaporated MoO_3, respectively. In the case of OSC with MoO_3 as a hole extraction layer, the

oval structure arose from the combination of NPs and MoO_3 layer has an oval shape, Hereafter, the oval structure is denoted as nanobump assembly (NBA). The detail process for Ag NP and MoO_3deposition is discussed in the chapter 3.

Afterwards two different mixtures of the polymer were spin casted on the top of NBA and the other solution based hole extraction layer. The first one is PCDTBT:PC_{70}BM solved in dichlorobenzene (1:4 weight ratio, 20 mg/mL). The thickness of active layer was 80 - 90 nm in thickness. The second one is P3HT:PC60BM in chlorobenzene (1:0.8 weight ratio, 20 mg/mL). In this case, the active layer was 150 nm. All the process was done in the nitrogen filled glove box. The coated polymer blend was annealed at a high vacuum ($<10^{-6}$Torr) chamber for more than two hours, for removing residual solvent. Finally, the device fabrication was completed by thermal evaporation of 0.5 nm lithium-fluoride for electron extraction layer and 100 nm Aluminum as the cathode through shadow masks under high vacuum chamber. For analyzing the effect of NBA on device, the device without silver NPs was also fabricated.

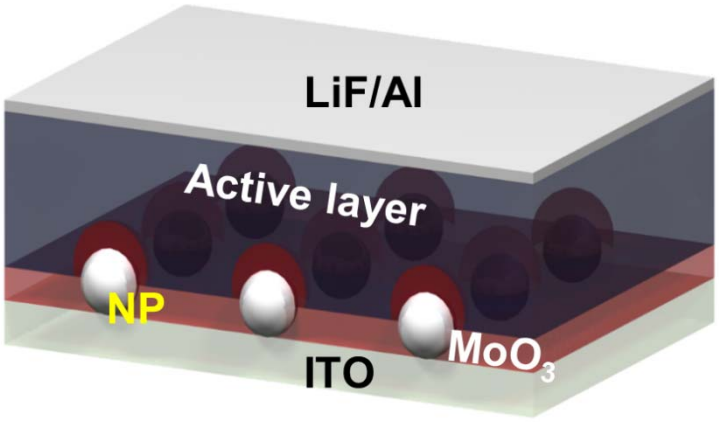

Figure 2.6 Schematic diagram of OSC with NBA.

2.4 Device and film characterization method

2.4.1 Thin film characterization

For the verification of NP's distribution on ITO, the field-emission scanning electron microscopy (FE-SEM) was conducted. For measurement, the NPs are deposited on the top of ITO patterned glass. These films are investigated by SEM without any other treatment. The model for this experiment is Augura, Carl Zeiss. And then the size and distribution of NPs were analyzed by SEM image using commercial graphic analyzing program (ImageJ software (v 1.46r)).

The morphology of NBA is smaller than 100 nm, which is the resolution of SEM, so that transmission electron microscopy (TEM), JEM-2100F(JEOL), was measured to verify the shape of NBA. For measuring the vertical morphology of OSC with NBA, the device was cut by focus-ion beam (FIB). The electron dispersion spectroscopy of atoms for NBA was also measure to ensure the formation of NBA.

To evaluate the encapsulation status of Ag NPs by MoO_3, x-ray photo spectroscopy (XPS) was conducted in the energy of approximately 370 eV, which is consistent with the energy level of Ag 3g 3/2. From this, a quantitative study for encapsulation status of Ag NPs in NBA employing different buffer layer was successfully analyzed.

Transient and steady state photoluminescence (PL) of donor only films with and without NBA are conducted. The intensity of steady state PL is an index to reveal the overlap between plasmonic resonance of NPs and the absorption band of

organic materials. Typically, the higher steady state PL of film represents enhanced light absorption induced from NPs. On the other hand, the lifetime of exciton can be derived from the transient PL. Hence, the PL is very powerful system to analyze the enhanced exciton generation in OSCs.

2.4.2 Device characterization

J-V characteristics of the devices were measured under the dark and light illumination (AM1.5G 100 mW/cm^2 illumination) on the ITO side with a solar simulator (Newport 91160A, KG5 filter), using a Keithley 237 source measurement unit. All the measurement was done in vacuum chamber to prevent OSCs from the degradation. For analyzing electrical and optical effect of NBA on the device, the J-V characteristics was conducted under the different incident light intensity using neutral density filters, whose optical density are from 0.1 to 2.0. In order to clarify the recombination losses, this measurement was also performed in the range of 100 to 300 K, loading OSC on to the cold finger of a closed-cycle He cryostat with LakeShore 331 temperature controller.

To calculate the number of carrier inside device, the impedance spectroscopy of device was measured under dark condition using an impedance analyzer (HP-4192A). Capacitance-voltage (C-V) dependence was measured from -1 to 1 V at 100 KHz.

IPCE spectra of devices were obtained in a nitrogen glove box using Oriel IQE 200 model, which combined monochromator and lock-in amplifier by comparison to a calibrated silicon photodiode.

2.5 The analysis method for Optical properties induced from NBA

For optical analysis induced from NBA in the OSC, A three dimensional finite domain time difference (FDTD) simulation was conducted based on the real device structure. Here, commercialized solution package (Lumerical solutions, version 8.4.3) and open source code. [56]

In FDTD simulation, it is assumed that the incident light source (300 – 800 nm in wavelength) propagates in z-direction with TE polarization. In addition, for simplicity, symmetric boundary for x-,y- axes and perfectly matched layer (PML) condition for z-axis were used. The light source for simulation was total field scatter field (TFSF) one. The ratio of scattering to the absorption was derived by employing two monitor: a total field and a scattered field power monitor. Using these power monitors, power flows induced by the interaction of the incident wave and a particle scatter were estimated. Also, extinction CS was evaluated by adding the absorption CS and the scattering CS. All optical constants for simulation was deduced from the ellipsometer data for our own fabricated films.

For experimental, UV-visible spectroscopy of film with and without NBA was conducted. Here the thickness of active layer for optical analysis film was relative thinner than that for device. For example the thickness for PCDTBT:$PC_{70}BM$ was 40 nm, while the blend thickness for device is almost 100 nm. And to minimize the side effects from reflective cathode, the UV-Vis was done a film without reflective electrode.

Chapter 3

Plasmonic Organic Solar Cells with Nanobump Assembly

The efficiency of OSC is limited by thin thickness of device which is caused by insufficient light absorption arose from thin active layer (several tens of nanometer) for efficient carrier generation and transport. So, efficient light trapping and coupling with the active layer are needed to realize highly efficient device. Among these, metallic nanoparticles (NPs) in OSCs have received much attention due to its superior optical properties with easy process[11] , NPs inside OSCs led to enhanced absorption of OSC, which is attributed to plasmonic effect and prolonged optical paths of the light by scattering[19,57].

Because of concerns about on the possibility of exciton quenchings in the active layer, NPs are mainly incorporated in the interfacial layer of the OSCs,

between active layer and electrode [58-61].The easiest way to employ NPs in OSC is coating method using soluble buffer layer with pre-mixed wet synthesized NPs. However, it is difficult to manage the concentration and distribution of NPs in these wet approaches, which is one of key factors to determine plasmonioc effect. Additionally, this method involves large amounts of solvents and need to use surfactants for preventing NPs from aggregation. Besides, there exist problems such as contamination and impurity of the particles generated. Furthermore, the PEDOT:PSS, widely used as a solution based p-type buffer layer, has acidic and hygroscopic features, resulting in instability of device arising from migration of indium originated from ITO electrode and residual solvent (water) [62]. What's worse, degraded PEDOT:PSS works as an insulator, which lead to the increased series resistance of device and recombination losses of carrier.

For overcoming these issues, NPs generated by deposition process have been also applied to the OSCs, which showed enhanced optical and electrical properties compared to the device without NPs [63-65]. Here, the buffer layer was consisted of metal oxides, such as molybdenum oxide (MoO_3), vanadium oxide and tungsten oxide, which shows higher stability in air and blocking the migration of indium to the active layer [62]. Additionally, this buffer layer, formed by deposition method, conformaly covered underlying structure, which allows us to utilize textured surfaces. However, in these cases, the size of NPs is limited by few nanometer, caused from the trade-off relationship between transmittance of layer and the plasmonic effect. The plasmonic effect from such a small sized NPs is smaller than that of large-sized one. Hence, if the new method, precisely controlled sized NPs covered by vacuum processed buffer layer is introduced, it will be much more beneficial to highly efficient and stable devices.

In this chapter, novel plasmonic OSC with the nanobump assembly (NBA) is demonstrated, which is consisted of aerosol derived NPs and thermally deposited MoO_3. Then, the device performance of device with NBA compared with the device with conventional plasmonic structure, where NPs are incorporated in PEDDOT:PSS. Finally, we discuss the NBA effect depending on the size of encapsulated NPs in terms of the enhanced light trapping and multi-reflection effects through empirical measurement and simulated results.

3.1 Formation of Nanobump Assembly

In this part, the procedure for forming NBA is elucidated. And the nano-morphology of NBA is studied by SEM and TEM. Using this method, the NBA, combination of plasmonic NPs with undulated active layer is successfully demonstrated.

3.1.1 Structure of NBA

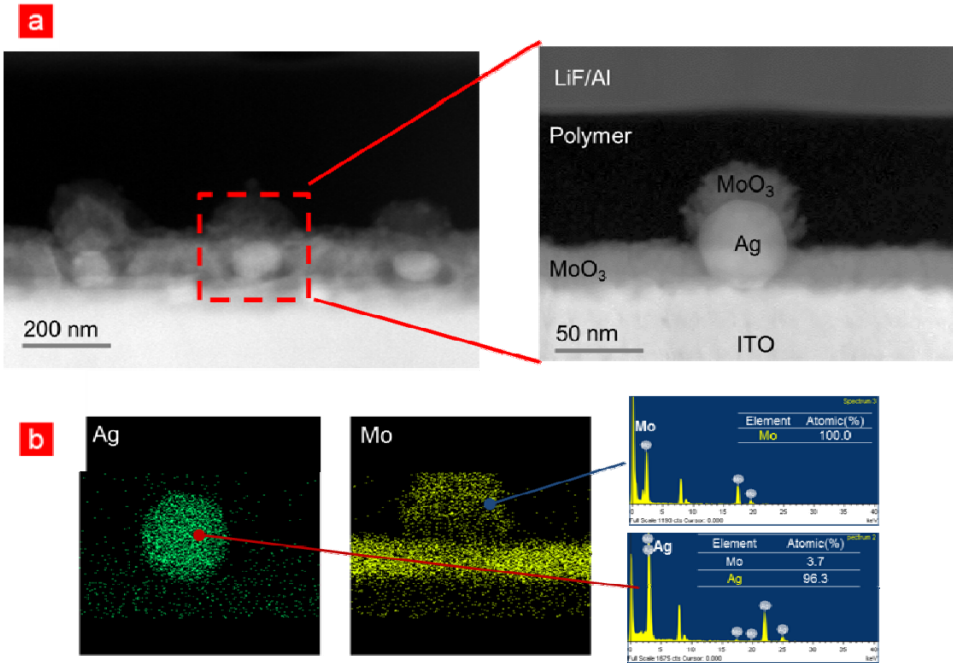

Figure 3.1 (a) Cross-sectional TEM image of OSC with nanobump assembly, consisted of aerosol derived NPs and thermally evaporated MoO_3, (b) Corresponding EDS of NBA showing the elements of Ag and Mo atoms.

Figure 3.1shows the cross-sectional TEM image of the OSC with NBA. To demonstrate the effect of the plasmonic NBA structure on the device performance with PCDTBT:$PC_{70}BM$ or P3HT:$PC_{60}BM$, theMoO_3 layer was thermally deposited on the ITO electrode containing Ag NPs on top of it. The device was finalized with lithium-fluoride and Al. In this figure, it is clearly shown that 40 nm of Ag NPs are fully covered by MoO_3, and the conformal 20nm MoO_3 are deposited on the upper half surface of NPs On the other hand, the side of NPs are barely covered by the hole extraction layer. Thereby, the NBA has an oval shape. This protruded oval shaped NBA forms textured surface, which is origin of undulated active layer. The feature and shape of NBA is confirmed by EDS analysis in Figure 3.1.b, which describe the number of atoms in the structure. The EDS clearly identified the shape of the MoO_3 layer and the Ag NPs in the NBA. Also, EDS revealed that Ag NPs maintained its spherical shape during the deposition of hole extraction layer and active layer. Moreover, NPs are contacted with the electrode, rather than floating inside buffer layer, normally observed in conventional wet-based NPs. Therefore, the cross-sectional TEM image certified that NBA has an oval shape and Ag NPs are covered by MoO_3, following underlying structure.

Figure 3.2 shows the fabrication methods for NBA. First the NPs are deposited on the cleaned ITO via aerosol method. Here, precisely controlled NPs with very small deviation are randomly deposited on the top of ITO. As shown in Figure 3.1, the shape of Ag NPs is close to the perfect sphere. To prevent oxidization and sulfurization of Ag NPs, all process was done in a nitrogen filled globe box. The concentration of NPs on the substrate can be controlled by changing deposition time. In this case the surface coverage of NPs is approximately 1.5%. Such a low

concentration, the chance of NP's aggregation is negligible. From this method, well size defined NPs are generated.

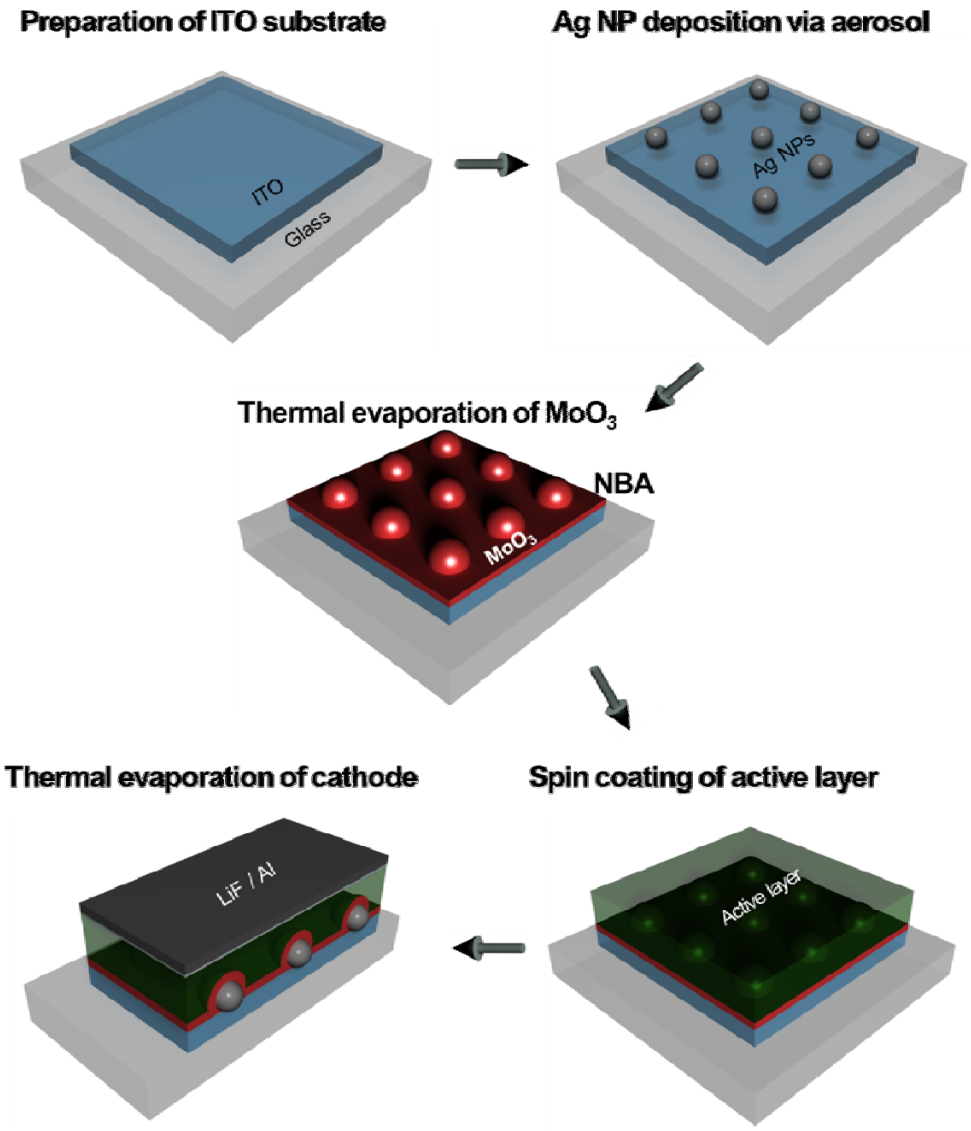

Figure 3.2 The fabrication procedure for nanobump assembly (NBA)

After that MoO_3 was deposited on the NPs at a high vacuum chamber. Here, the deposition rate is in the range of 0.05-0.1 nm/s. The thickness of MoO_3 is monitored by vibrating gold sensor. As aforementioned, this hole extraction layer follows underlying structure, so that the protruded nanostructure is demonstrated. As a result, the plasmonic effect from NPs and nano-sized structure is expected in the OSC with NBA. Moreover, the enlarged surface area from NBA increases the carrier extraction efficiency of the device. It should be noted that this structure is universal to the any kinds of polymer based solar cells. And by changing the materials of NPs and surrounding media, the plasmonic effect can be tuned easily.

After formation of NBA, polymer blend is over-coated on the top of this nano structure. And the device is finalized with reflective electrode. As a result, the device with the combination of plasmonic structure and undulated active layer can be realized.

3.1.2 Aerosol derived Nano particles

To generate metallic NPs and nanostructures in a controlled manner, an aerosol approach utilizing the evaporation and condensation method shas been extensively studied since the work of Scheibel and Porstendörfer, demonstrating various shapes and sizes of generated NPs and local heating control. [66-68]. The advantage of this method is to generating NPs in atmospheric condition, which decrease the manufacturing cost. Additionally, the substrate size can be expanded, so that this method is suitable for large-sized module process. Moreover, H. Kim et al suggested that it is possible to control the deposition position of charged NPs by applying

electric field in substrate [69]. Additionally, it was shown that precisely size controlled NPs are prepared by inert gas condensation [70,71]. Hence, aerosol based evaporation and condensation method is suitable for depositing NPs on the substrate of plasmonic OSCs.

The setup for NP generation is illustrated in Figure 3.3. This is consisted of carrier gas, a furnace, a cooling system, a neutralizer, a nano-differential mobility analyzer, a high voltage power supply, two mass flow controllers (MFCs), and a deposition chamber in a glove box. The procedure for generating NPs is described below. First, a solid silver strip was placed at the quartz tube inside the furnace. (Okdu SiC tube furnace). Once the heat is applied to the silver strip, silver particles start to evaporate. Here, the size of silver is smaller than few nano meters. Then, the small sized silver particle move to the cooling system by using flow of nitrogen gas (99.999%, 1.5 liter per minute) throughout the tube. The flow of gas is controlled by two mass flow controllers. When these small size NPs reaches in the cooling line, the silver particle are tend to aggregate each other, which increase the size of NPs from few nanometers to several tens of nanometer. During this process, the temperature of cooling line maintained 26ºC Since the Gibbs free energy for spherical particle is the lowest level among the variety shapes, the shape of most NPs is sphere one [67]. The ionized poly-dispersive Ag NPs were produced via a neutralizer (HCT Aerosol Neutralizer 4530), where emit β-ray. These ions are brought together with an aerosol carried silver NPs, and then the positively and negatively charged particles are generated. Since the working principle of differential mobility analyzer is the hall effect, the neutralizer changed the ionized status of NPs from randomly distributed multi charged one to uniformly single charged one. Additionally, this process increases the number of deposited NPs on the substrate, where applied high negative voltage. This positively charged mono-

dispersive NPs were classified by the nano-DMA (TSI 308500).The size of NPs was selected by varying the applied voltage according to particle's electrical mobility through the DMA controller. For example, 1.03, 3.93, and 8.42 kV were applied to classify the 20, 40 and 60 nm sized silver NPs, respectively. As a result it is possible to define the size of NPs. Finally, the NPs transport to the deposition chamber using the nitrogen gas flow. The charged particles are attached to the ITO coated glass owing to electrical force from applied high voltage. Here the voltage was fixed -1 KV in this experiment, but it is possible to control the number of deposited particle by changing the electric field. In this case, we set the concentration of NPs as 3.0×10^5 cm^{-3}on average, while the deposition process monitored by condensed particle counter. By controlling the deposition time, the density of NPs on ITO substrate was successfully achieved. The range of the NP's concentration density was from 0.2 to 1.5×10^9 cm^{-2}.

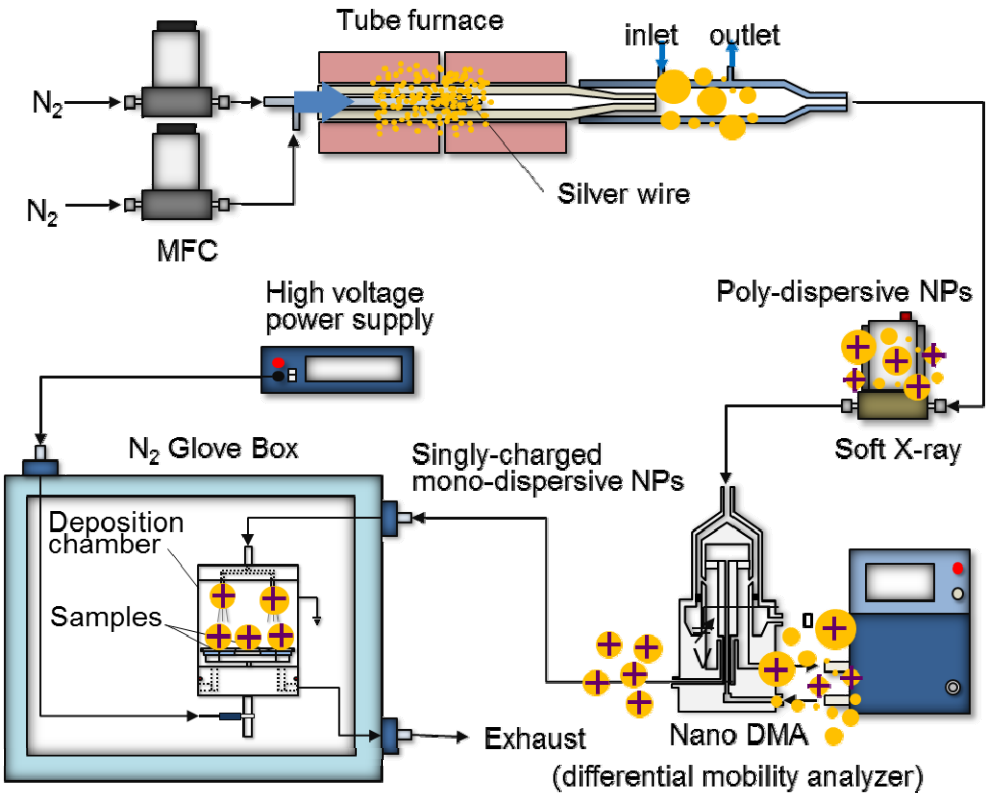

Figure 3.3 The setup for generating NPs based on evaporation and condensation method via aerosol.

To verify the size and distribution of NPs, the FE-SEM was conducted for the film with 40 nm Ag NPs. Figure 3.4 is the FE-SEM image (× 50,000 in magnification, 6.0 μm × 4.2 μm in analysis area) of 20nm. It is confirmed that incorporated 20nm of Ag NPs are uniformly but randomly deposited onto the ITO with small standard deviations of their sizes (σ): σ = 2.3. However, the sub peak for NP size around70 nm was observed in the histogram graph, which increases the deviation of NPs. We believe that this sub peak was mainly originated from the two NPs located very closely, since the analysis program does not support to distinguish such particles.

Table 3.1 summarized the average size and deviation of NPs derived from different method. It has been reported that the NPs generated by thermal evaporation method shows a large deviation value (22-75%) arising from randomly distributed metallic particles. In wet-based synthesis, such as Hydrothermal and polyol method, the deviation value of NP (11- 30 %) decreased in comparison with that produced by evaporation method. However, this value is still high for achieving uniformly efficient plasmnic OSC, since the plasmonic peak and intensity is very sensitive to the size and distribution of NPs. On the other hand, the NPs generated by aerosol method has a very small deviation, only 5%. As a result, aerosol derived NPs are suitable approaches to realize OSC with precisely controlled plasmonic effect.

Table 3.1 The size of NPs and their deviation generated by different method

Synthesis method	NP size (nm)		Ratio	Ref
	Average	Deviation		
Aerosol derived (Ag)	44	2.3	5%	[72]
Thermal deposition (Ag)	8	6	75%	[65]
Thermal deposition (Ag)	87	20	22%	[73]
polyol(Ag)	40	12.6	30%	[74]
Hydrothermal (Au)	45	5	11%	[61]

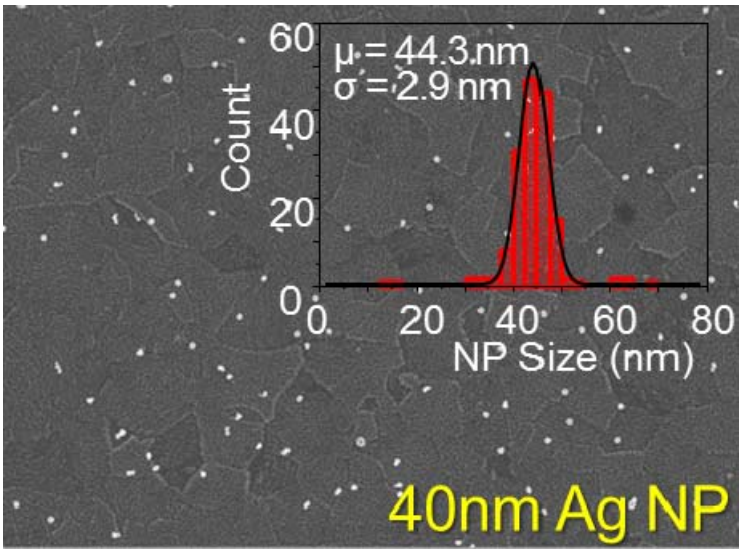

Figure 3.4 The FE-SEM image for the 20nm sized Ag NPs deposited ITO substrate. The inset of image is the histogram analysis of NPs' size with mean (μ) and standard deviation (σ) value of them.

3.2 Device performance of plasmonic organic solar cell with NBA

In this part, we have investigated the effects of plasmonic nanostructure, NBA, on the device performance of OSC. And then, the effect of NBA is compared to the conventional plasmonic structure consisted of Ag NPs embedded in solution processed buffer layer. The result reveals that the plasmonic and electrical effect form NBA is superior to those of conventional method. As a result 16% enhancement in PCE of OSC with NBA was achieved compared to the device without NBA.

3.2.1 P3HT:PCBM based OSC with and without NBA

Figure 3.5 shows the J-V characteristics of OSC with and without NBA. The device structure is followed by aforementioned structure (See Figure 2.6). And the active layer of device is consisted of P3HT:$PC_{60}BM$ blend, which is widely used in OSC, and the NBA is prepared by 40 nm sized Ag NP covered by 20 nm MoO_3. Here the density of NPs is 0.5×10^9 /cm^2, which covers approximately 2% of surface of ITO substrate. As shown in Figure 3.5 the PCE of device with NBA (2.9%) is higher than that of device without NPs (2.7%). The enhancement of device performance is mainly attributed to the improved photocurrent from 7.7 to 8.1 mA/cm^2, while the other factors, V_{OC} and FF, maintain similar values.

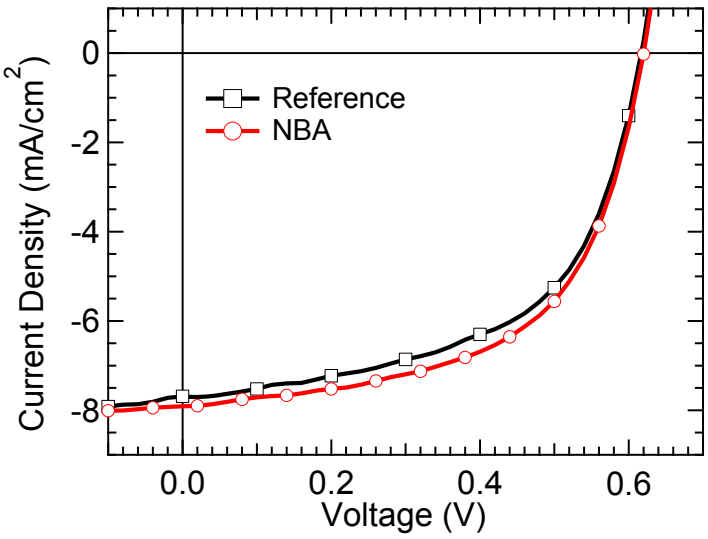

Figure 3.5 J-V characteristics of P3HT:$PC_{60}BM$ based OSC with and without NBA. Here, the size of NP is fixed 40 mn covered by 20 nm MoO_3

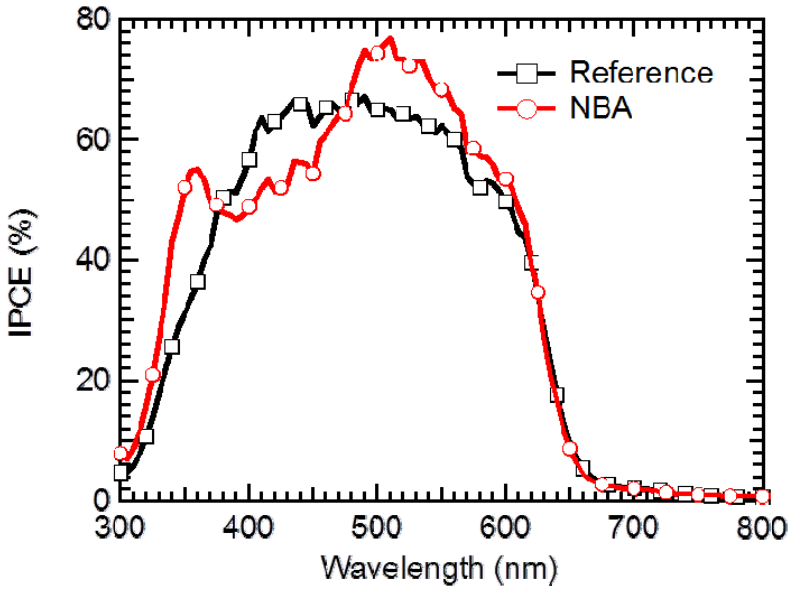

Figure 3.6 IPCE of P3HT:$PC_{60}BM$ based OSC with and without NBA.

Table 3.2 The device performance of P3HT:$PC_{60}BM$ based OSC with and without NBA

	J_{SC} (mA/cm^2)	V_{OC} (V)	FF	PCE (%)	R_s ($\Omega \cdot cm^2$)
w/o NBA	7.7	0.62	0.57	2.7	1.9
NBA	8.1	0.62	0.58	2.9	2.3

The IPCE data clearly illustrates that the enhanced spectral response of device at 500 nm region increases the photocurrent. Especially, the IPCE of device with NBA is 20% higher than that of device without NP at the 520 nm light. This result is coincident with plasmonic peak of Ag NPs and structures [44-46]. Here, the reduction of IPCE at 400 nm may be originated from the decreased light intensity at this region, caused by the absorption of Ag NPs itself. Additionally, the enhanced series resistance of device with NBA is observed, which reflects carrier transport inside device. We believe that the protruded hole extraction layer (HEL) enlarges the interface area between active layer and HEL, which leads to the improvement in carrier extraction without small losses. Therefore, J-V and IPCE data for OSC with NBA clearly point out that the plasmonic and electrical effect from NBA increase photocurrent, thereby resulting in high PCE of device.

3.2.2 PCDTBT:PCBM based OSC with and without NBA

In previous chapter, it is clearly shown that the plasmonic and electrical effect from NBA increase device performance. However, the absorption band of polymer

blend, P3HT:PC60BM is narrow, so that the enhanced light absorption in red and near infra-red region is not studied. Moreover, the thickness of P3HT:$PC_{60}BM$ based OSC is relative thick (~150 nm), which allows active layer to harvest more light compared to recently synthesized polymer, such as PTB7 and PCDTBT [75]. For this subchapter, the effect of NBA on device employing low band gap polymer, PCDTBT:$PC_{70}BM$ is studied.

Figure 3.7 is the J-V characteristic of device with and without NBA under 1 sun condition, whose device structure is ITO/ MoO_3 (20 nm)/ PCDTBT:$PC_{70}BM$ (100 nm)/LiF(0.5 nm)/Al (100nm). The device without NBA showed $J_{SC}$of 9.2 mA/cm^2, V_{OC} of 0.88 V, FF of 0.64 and PCE of 5.16 %. The enhancements in J_{SC} and PCE were achieved by inserting NBA structure without deteriorating FF and V_{OC}. In particularly, the OSC with NBA consisted of 40nm Ag NP covered by 20 nm of MoO_3 showed the maximum OSC performance with J_{SC}= 10.4 mA/cm^2, V_{OC} = 0.88 V, FF = 0.64 and PCE = 6.07 %. It means that NBA structure leads to the 13% and 17% enhancement in JSC and PCE, respectively. This value is higher than case with P3HT:$PC_{60}BM$ based OSC, since the active layerof PCDTBT:$PC_{70}BM$ OSC is thinner that that case.

To verify the plasmonic resonance of NBA, the IPCE analysis for devices was conducted as represented in Figure 3.8.The IPCE data reveals that the OSC with NBA harvest more light at the range from 500 to 640 nm compared to the device without NBA. Especially, the IPCE enhancement ratio, calculated from the dividing the IPCE data of OCS with NBA by that of OSC without NBA, shows its maximum value at the wavelength of 540 nm. This result is in the good agreement with the case of OSC consisted of P3HT:$PC_{60}BM$. Hence it is clear that the plasmonic resonance of 40nm Ag NP enclosed by 20 nm MoO_3 is around 540 nm.

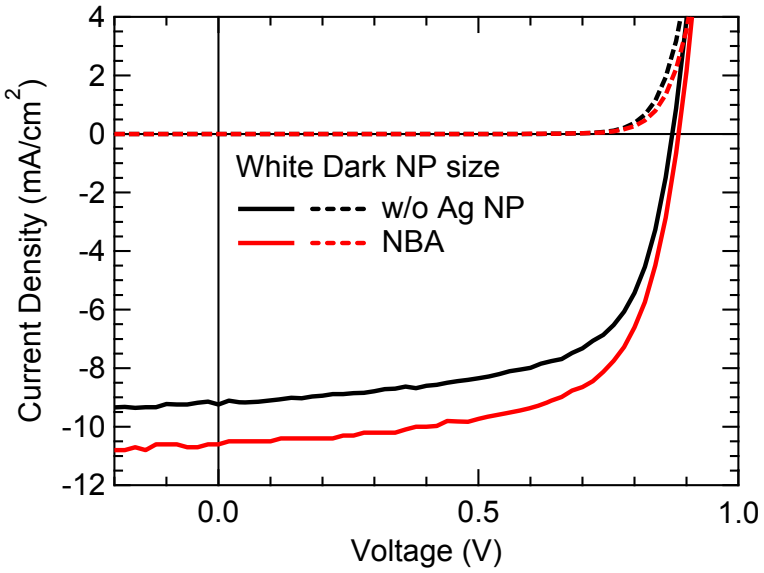

Figure 3.7 J-V characteristics of PCDTBT:$PC_{70}BM$ based OSC with and without NBA. Here, the size of NP is fixed 40 nm covered by 20 nm MoO_3

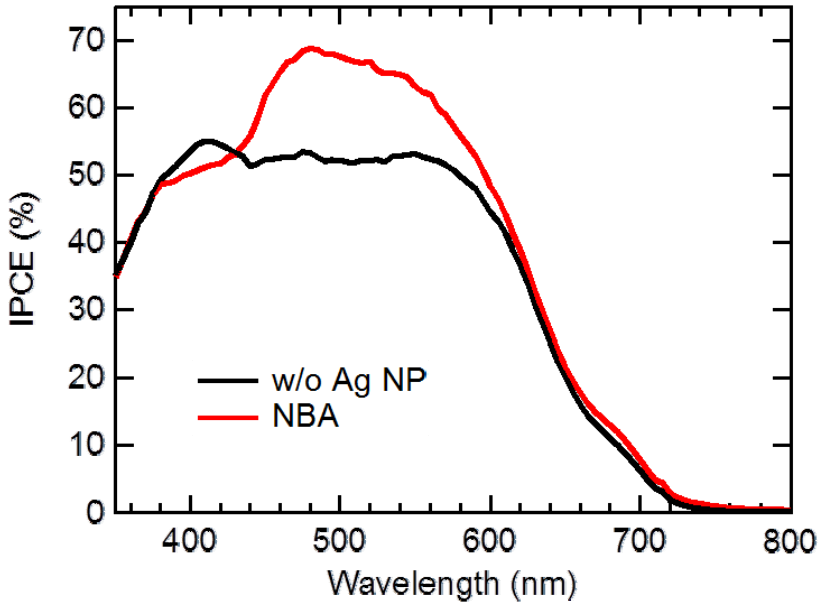

Figure 3.8 IPCE of PCDTBT:$PC_{70}BM$ based OSC with and without NBA

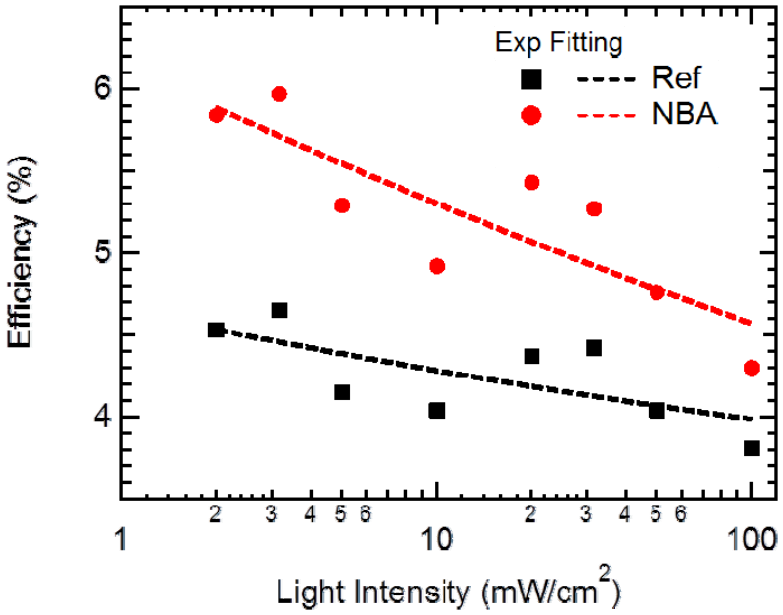

Figure 3.9 Light intensity dependence of PCE of devices with and without NBA.

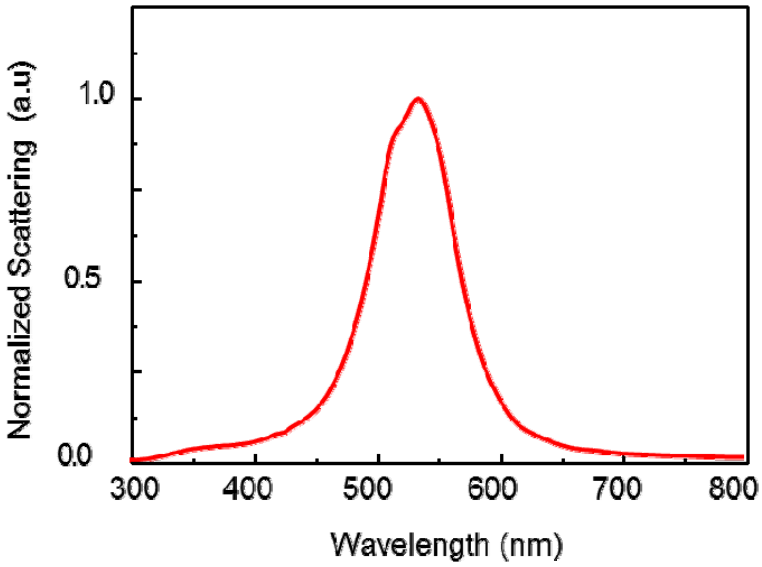

Figure 3.10 Simulated scattering ratio of NBA consisted of 40nm Ag NPs covered by 20nm MoO_3

Moreover, this novel plasmonic structure increases device performance under the weak light intensity, as shown in Figure 3.9. Interestingly, the PCE enhancement ratio increase as the light intensity decrease. That is the plasmonic structure manages light inside OSC to harvest more photocurrent. And this effect is more emphasized when the light intensity decrease. Thus, it is apparent that novel plasmonic structure, NBA is very useful method to convert light into energy more effectively.

For estimating the origin of plasmonic effect, the scattering ratio from NBA is calculated 3D FDTD method. In this simulation, all optical constants (*n, k*) were obtained by the real empirical thin film of materials by measuring ellipsometer. The Figure 3.10 described the simulated scattering ratio at visible light region. The results show that the scattering effect happens at entire visible light. Particularly, the highest scattering ratio is observed at 550 nm, where is accordance with the empirical result of P3HT:PCBM and PCDTBT:PCBM based OSC. Here, the slightly difference of the maximum points for simulation (550 nm) and experimental data (540 nm) is mainly caused by the assumption of NP's periodic distribution in OSC for the simplicity of calculation. Hence it is apparent that the plasmonic effect at 550 nm from NBA increases photocurrent of OSC, which leads to highly efficient devices.

In electrical point of view, the textured HEL structure and undulated active layer is occurred by the NBA as shown in Figure 3.1. This enlarged surface area and the NBA have merits to extraction carrier for the following reasons. First of all, the enlarged surface area allows more generated carrier to extract to the electrode without small losses. Furthermore, the mobility of hole carrier in Ag NP is much more faster than that in MoO_3. What's more, the decreased distance between active layer and electrode arose from the oval shaped nano structure leads to better carrier swept-out to the electrode.

To clarify this effect, the J-V characteristics of OSCs under dark condition were measured as shown in Figure 3.11. In dark condition, the photocurrent is negligible compared to the diode current, which only describes the change of series resistance inside device. In dark current at 1V of OSC with NBA at is 10% higher that of OSC without NBA. Since the surface coverage of NPs derived from SEM image (See Figure 3.4) is around 2 %, so that the enlarged surface area is approximately 5%. Thus, the enlarged surface increases current of device with NBA by 5%, while another 5% may be originated from the aforementioned electrical effect of NBA. Therefore, NBA is not only improving electrical aspect of device, but also the enhanced electrical properties of device can be achieved.

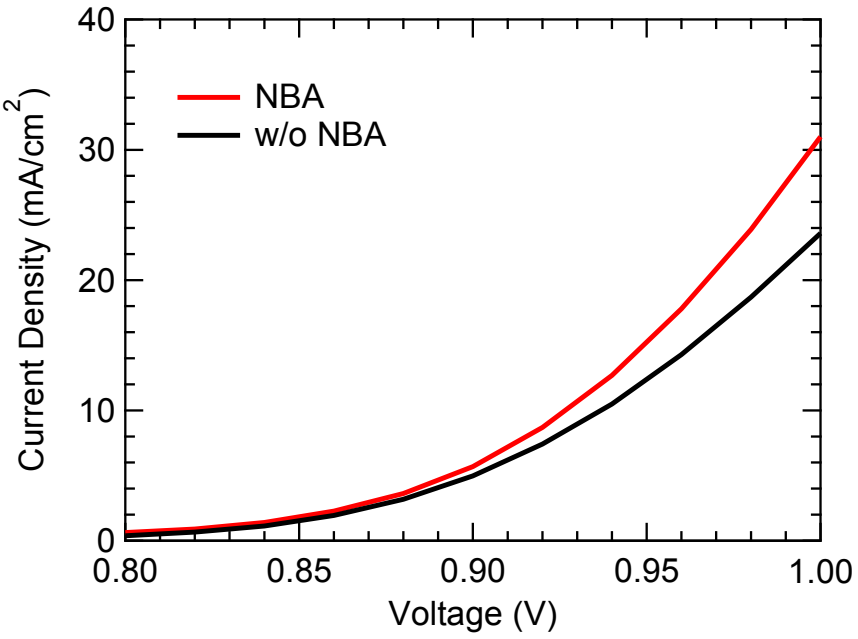

Figure 3.11 J-V characteristic of OSC under dark condition.

For finding out the electrical side effect from inserting NBA, the light intensity dependence of device performance was measured under different light intensity using neutral density optical filter. Figure 3.12 denotes the light-intensity (P_{Light}) dependence of J_{SC} ($J_{SC} = P_{Light}^{\alpha}$) for devices on a double-logarithmic scale. Here, α is a power-law value that represents recombination properties. Several groups have reported that monomolecular recombination dominates the recombination properties of a device when α is close to 1. Meanwhile, whenα = 0.75, there combination loss of a device is controlled by space charges [76, 77]. If the NBA affects the recombination properties of device, the α will be changed. However, in both cases the α is remained unchanged (i.e. OSC with NBA: α= 0.91 and OSC without NBA: α= 0.92). This results show that NBA, NPs are fully covered by dielectric layer, increase photocurrent without changing the recombination losses. Recognizing electrical and optical properties induced by NBA, the NBA is an effective plasmonic approach to enhance the performance of OSC.

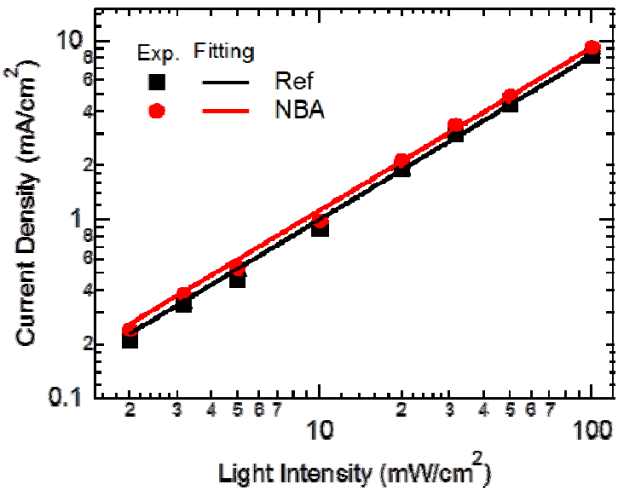

Figure 3.12 Light intensity dependence of J_{SC} and devices with and without NBA

3.3 Comparison of Plasmonic effect induced by NBA and conventional method

In this sub-chapter, the device performance of plasmonic OSC with NBA is compared to that of device with widely using conventional plasmonic structure, where NPs (40 nm) are implemented solution processed hole extraction layer (PEDOT: PSS).The device structure for both cases are shown in Figure 3.13: ITO/ MoO_3 with NBA (20 nm)/PCDTBT:$PC_{70}BM$ (90 nm)/LiF (0.5 nm) /Al and ITO/NPs incorporated PEDOT:PSS (20 nm)/ PCDTBT:PC70BM (90 nm) /LiF (0.5 nm)/Al. For accurate analysis, devices having different hole extraction layer without NPs are also fabricated. The relatively thin PEDOT:PSS (20 nm) was chosen as the HEL for direct comparison with the NBA case [78].And the NPs were generated by aerosol method to minimize the side effects from different distribution of NPs . Moreover, the device structure and all manufacturing procedures except the HEL were exactly the same as those of devices with the NBA. To identify the optical effect of plasmonic structure, IPCE, steady-state PL, UV-Vis spectrum and optical simulation were performed. On the other hand, the electrical effect of them was also studied by the transient PL.

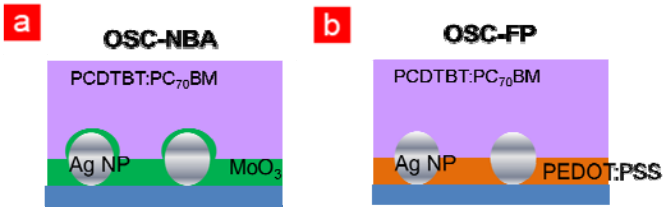

Figure 3.13 Device structure of OSC-NBA and OSC-FP

3.3.1 Device performance of OSCs

Figure 3.4 shows the J-V characteristics of devices with different plasmonic structures and the results are summarized in Table 3.3. The PCE of the device with NPs embedded in flat PEDOT:PSS (OSC-FP) is (5.67%) is improved compared to its counterpart without metallic NPs (5.20%). As the flat PEDOT:PSS is replaced to the NBA structure as a HEL, the PCE of the OSC with NBA (OSC-NBA) further increases to 6.07%. Especially, this enhancement is mainly originated to the enhancement in J_{SC} from 10.24 (OSC-FP) to 10.58 mA/cm^2 (OSC-NBA), while the other photovoltaic parameters, FF and V_{OC}, are a little bit changed. Interestingly, the device performance of the samples without Ag NPs is very similar to each other regardless of different hole extraction layer (5.20% for PEDOT:PSS and 5.16% for MoO_3) types (Table 3.3). It means that the change of buffer layer does not affect carrier extraction of device without NPs. On the other hand, the NBA structure more significantly influences on the photovoltaic characteristic compared to the device with the same sized NPs embedded in the flat PEDOT:PSS.

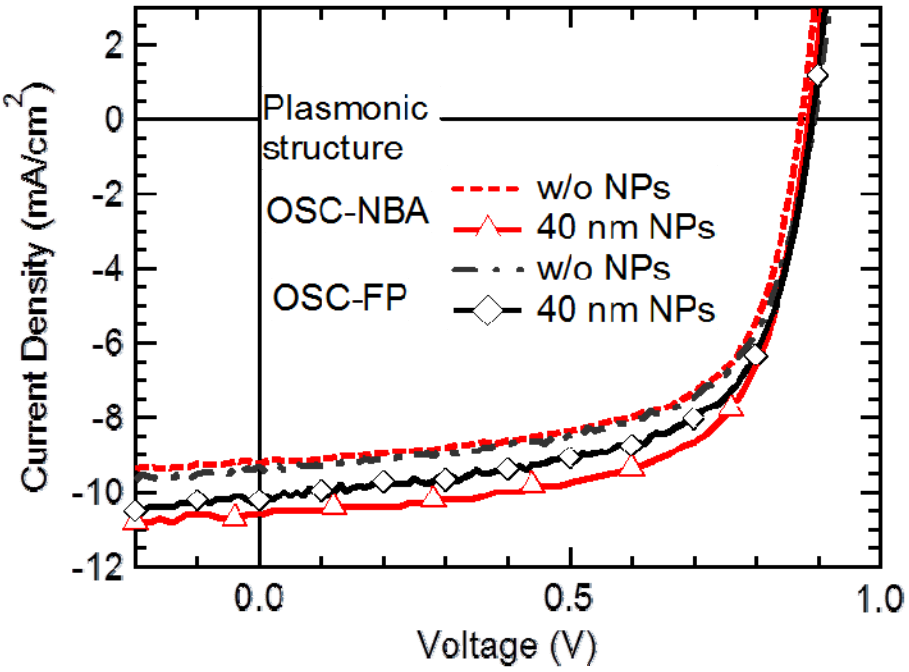

Figure 3.14 J-V characteristics of device with and without plasmonic structure. Here the NBA and NPs incorporated PEDOT:PSS were used as plasmonic structures

Table 3.3 The device performance of OSC with different plasmonic structure

Buffer layer	NPs	J_{SC} (mA/cm^2)	V_{OC} (V)	FF	PCE (%)
Flat PEDOT:PSS	-	9.19	0.89	0.63	5.20
	40 nm	10.24	0.89	0.63	5.63
NBA	-	9.18	0.88	0.64	5.16
	40 nm	10.58	0.88	0.65	6.07

3.3.2 Optical properties of different plasmonic structures

Generally, the J_{SC} is determined by two factors, carrier generation and transport to electrodes. To verify the origin of high J_{SC}, the IPCE measurement was conducted, which reflects the optical properties of different plasmonic structure inside devices at specific wavelength, related with carrier generation. Figure 3.15 is the IPCE spectra of OSC-FP and OSC-NBA. Here, the enhancement ratio of each case is derived by dividing the IPCE of OSC with NPs to that of OSC without NPs. The increase in J_{SC} of the OSC-NBA is caused by the increased spectral response at the wavelength of 450 – 600 nm. On the other hand, the IPCE of OSC is outstandingly improved at a short wavelength (~ 350 nm) ,approximately 10% broad enhancement in IPCE at 400 - 650 nm was observed. This result is similar to the previous reported study, which dealt the plasmonic OSC embedding Ag NPs in PEDOT:PSS by wet synthesis. [30]. Since the spectral response of OSC is relative low (~50 %) at the light with high energy (~ 400 nm), it is clear the OSC-NBA shows higher J_{SC} compared to that of OSC-FP. Therefore, the plasmonic effect arose from NBA, increasing IPCE at longer wavelength than that induced by NPs in PEDOT:PSS, leads to the better device performance of device.

To find out the difference of IPCE between OSC-NBA and OSC-FP, the optical simulation was conducted considering refractive index of materials. For the simplicity, the scattering cross-section from core/shell NPs enclosed by different refractive index material was simulated. Here NPs were surrounded by a material whose refractive index is fixed to 2, similar to the refractive index of PCDTBT:PC_{70}BM polymer blend. Additionally, the size of silver NP is 40 nm, while the shell thickness is 20 nm. As shown in Figure 3.16, the maximum point for

scattering effect induced by core/shell type is red-shifted, as the n of covered dielectric layer increases. Moreover, the intensity of scattering increased in samples with NPs covered by high n material. So, it is apparent that NPs covered by high refractive index shell is much more beneficial than NPs surrounded by low refractive index material. As aforementioned, the n of PEDOT:PSS is ~ 1.6 in the visible light, whereas the refractive index of MoO_3 is almost 2. Hence, the plasmonic effect induced by NPs located inside PEDOT:PSS can be predicted by the simulation result of Ag NPs encapsulated by low refractive (n= 1.5). In this case, the main calculated plasmonic peak is less than 400 nm, which is consistent of empirical IPCE data of OSC-FP. In contrast, the simulated peak for Ag NPs covered by high refractive index (n = 2.0) is red-shifted, approximately 520 nm. And the scattering intensity is 50 % higher than that of NPs located in PEDOT:PSS. That is the LSPR and scattering effect form NBA is well transferred into the active layer. This result is also similar to the experimental IPCE of OSC-NBA. Consequently, the simulation result reveal that the plasmonic effect induced by the NBA, NPs covered by high n material, increase more photocurrent at the longer wavelength compared to the PEDOT:PSS case, which is a good agreement of experimental data.

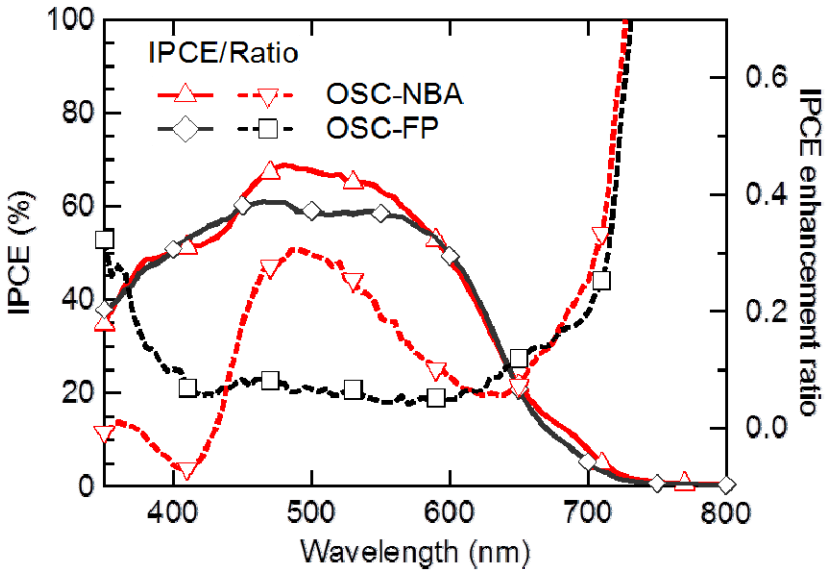

Figure 3.15 The IPCE data of OSC-NBA and OSC-FP as well as their enhancement ratio. Here, the ratio is calculated by comparing the IPCE of the OSC without NPs

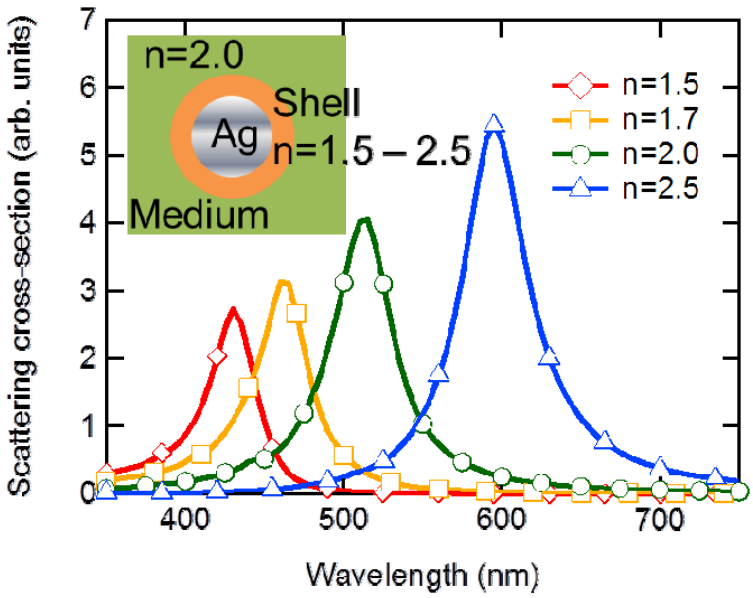

Figure 3.16 The scattering cross section of core/shell Ag NPs (40nm) enclosed by different dielectric layer (20 nm) inside polymer layer (n = 2). Here, the refractive index of dielectric layer is varied from 1.5 to 2.5.

To more accurate analysis, the simulation for near field enhancement and scattering cross-section was also conducted in the real device structure. Figure 3.17 (a) illustrates the schematic for the calculation, where NP were located in the flat PEDOT:PSS buffer layer and bumped MoO_3. The calculated results show that the intensity of scattering induced by NBA is much higher than that of NPs embedded in PEDOT:PSS. (See Figure 3.16(b))And the peak wavelength for scattering cross-section is accordance with that of IPCE for OSC-NBA. That is improvement in scattering features of NBA is the origin of enhanced absorption of film with it.

Meanwhile, it is observed that the near field enhancement by LSPR is well transferred into the active layer in NBA, despite elongated distance between NPs and polymer layer. Compared to the case of PEDOT:PSS, where NPs are partially contacted with polymer layer, the optical properties caused by high refractive index of MoO_3 provided the improved absorption of active layer in NBA. Figure 3.17 (d) shows that this enhancement is attributed to the strong forward scattering of NBA. Therefore, the simulation result shows that superior optical properties of NBA lead to higher photocurrent of OSC in comparison with OSC-FP.

a

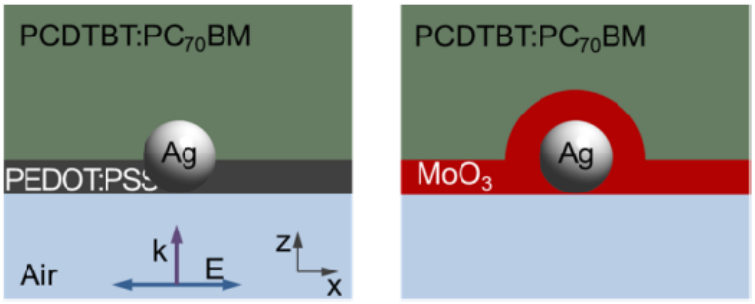
PCDTBT:PC70BM
Ag
PEDOT:PSS
Air
k
E
z
x
PCDTBT:PC70BM
Ag
MoO3

b

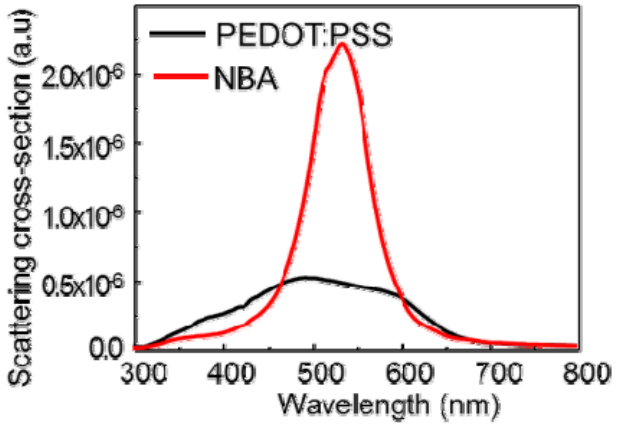
PEDOT:PSS
NBA
Scattering cross-section (a.u)
2.0x10-6
1.5x10-6
1.0x10-6
0.5x10-6
0.0
300
400
500
600
700
800
Wavelength (nm)

c

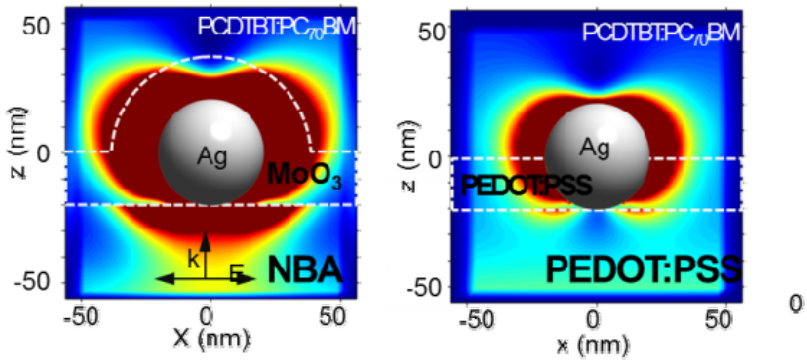
PCDTBT:PC70BM
Ag
MoO3
k
E
NBA
50
0
-50
z (nm)
-50
0
50
X (nm)
PCDTBT:PC70BM
Ag
PEDOT:PSS
PEDOT:PSS
50
0
-50
z (nm)
-50
0
50
x (nm)
0

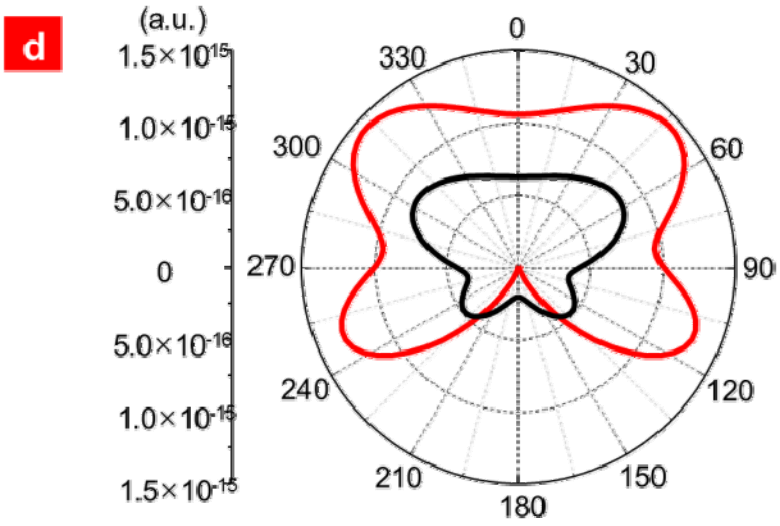

Figure 3.17 (a) Theschematic of plasmonic structure for optical simulation. (b) Scattering cross section induced by the NBA and the PEDOT:PSS containing 40 nm Ag NPs.(c) Near-field simulation of films in xz-plane at the wavelength of 530 nm. (d) FDTD Simulation on far field radiation pattern at the peak at yz --plane

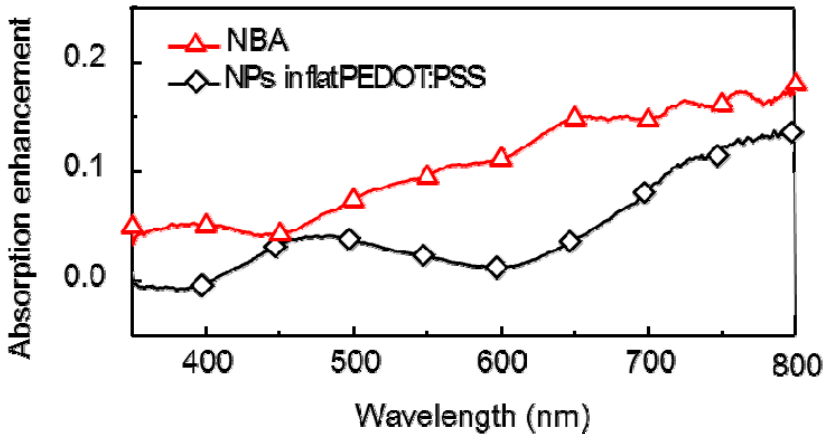

Figure 3.18 The absorption enhancement ratio of PCDTBT:PC70BM films (80 nm) with plasmonic structure including 40 nm sized Ag NPs. Here buffer layers are PEDOT:PSS and thermally evaporated MoO_3

This results are coincided with the simulated result on the scattering CS (Figure 3.17c) and the UV-visible light absorption spectra of the PCDTBT:$PC_{70}BM$ films casted on the both MoO_3 and PEDOT:PSS with Ag NP (See Figure 3.18). Therefore, it is obvious that the enhanced scattering intensity near the green light with a strong forward direction via the NBA makes the photocurrent of device higher compared to the case with flat buffer layers

Another interesting point in IPCE, It is observed that the peak for the IPCE enhancement ratio of both cases occurred over 700 nm wavelength, despite of the change of plasmonic structure. Generally, this wavelength is not matched with the near field enhancement in electrical field induced by scattering and plasmonic effect, as shown in Figure 3.16. Moreover, the enhancement at this region is not exhibited in the film incorporating plasmonic structure without reflective electrode. H. Atwater et al. reported that there are three optical effects of metallic NPs in OSC: scattering, LSPR, and the multiple-reflection between NPs and reflective electrode. Since the resonance wavelength induced by scattering and LSPR is in the region of green and blue light, so that the enhancement in IPCE at red and near infra-red region may be originated from trapped light between the NPs and the Al electrode *via* the multi-reflection similar to the Fabry–Pérot resonator. Typically, this light entrapment elongates the optical path length within active layer of OSC, which leads to the enhancement of light absorption. To estimate underlying mechanism of this peak, the effect of the Al electrode was simulated, because the multi-reflection within the active layer is only occurred at the film sandwiched by two reflective materials. The simulation was conducted based on the NBA incorporated plasmonic OSC with and without the reflective electrode. The absorption enhancement spectra of the plasmonic OSCs relative to the reference cell (without Ag NPs) were

calculated in the spectral range of 350 to 800 nm. In the NBA embedded film without the reflective electrode, the peaks around 750 nm are highly suppressed compared to the case of devices with the Al electrode. Therefore, it is confirmed that the absorption peak at red light region is attributed to the multi-reflection induced by the NBA.

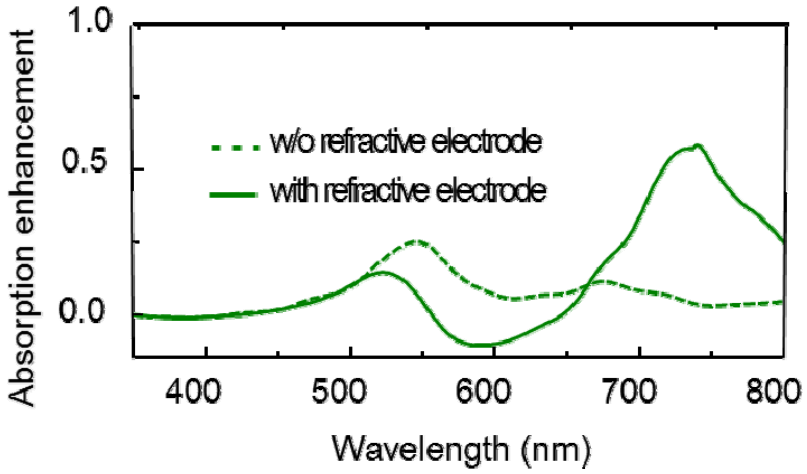

Figure 3.19 The simulated absorption enhancement ratio of PCDTBT:$PC_{70}BM$ films (80 nm) casted on the NBA with and without refractive top electrode

In conclusion, the NBA offers broadly and highly increased plasmonic effect compared to the NPs located PEDOT:PSS. This is mainly attributed to the high refractive surrounded dielectric layer of NBA, MoO_3. This optical feature of NBA leads to the improved light absorption of OSC at green and region, where the absorption band of PCDTBT:$PC_{70}BM$ is well overlapped. Additionally, the multiple-reflection between the NBA and the reflective electrode elongates light paths within the active layer. Therefore, it is apparent that the OSC with NBA shows improved PCE compared to the other plasmonic structures.

3.3.3 Electrical properties of plasmonic structure

The steady-state photoluminescence (PL) of film with plasmonic structure is generally determined by two factors the resonance frequency overlap between the absorption band gap of polymer and the nanostructure induced plasmonic effects, as well as the decay of photo-generated excitons [79]. So, this technique is widely used to investigate optical and electrical effect of plasmonic structure. Figure 3.20 (a) is the steady-state PL of the PCDTBT films (40 nm) casted on the NBA and NPs incorporated in flat PEOD:PSS. Here, the size of NP is 40 nm, which is exactly the same as the NPs in OSC. The result represents that the PL intensity of the film with NBA is enhanced than that of film with NPs incorporated PEDOT:PSS in broad region. It is apparent that the PL of film with NBA is higher than those of film with NP incorporated PEDOT:PSS and film without NPs. This is another supportive evidence to show better optical properties of the NBA. The aforementioned simulation and empirical results already make it a clear that the optical effect induced by the nano structured buffer layer contributes to the enhancement in the steady-state PL. But, the discrepancy of the intensity in the steady-state PL between the film with NBA and one casted-on flat PEDOT:PSS including NPs is bigger than that of the photocurrent of each corresponding devices.

To estimate the electrical effect of different plasmonic buffer layers, transient PLs of both films were measured at the wavelength of 690 nm excited by 405 nm pulse laser (iHR320, Horiba, Ltd.), where the PL intensity of polymer film shows

highest value. (See Figure 3.20 (b)). The exciton lifetime of films including each plasmonic structure were derived by using equation 3.1, [61]

$$I_{PL}(t) - \sum_{i=1}^{n} A_i \exp\left(-\frac{t}{\tau_i}\right) \quad (3.1)$$

Where A_i is the amplitude of the *i*th decay, n is the number of decays, and τ_i is the ith exponential constant. The lifetime of exciton in the films with PEDOT:PSS including NPs, the exciton lifetime is 478 ± 28 ps. On the other hand, the lifetime of exciton in polymer blend coated on the top of NBA is 575 ± 25 ps, which is very similar to that of film without NPs (585± 15ps). Since the polymer layer was fixed among samples, so that the short exciton lifetime of film with NP incorporated PEDOT:PSS is related the exciton quenching induced by plasmonic structure. It has been already reported that the metallic NPs, directly contact with the polymer layers can work as an exciton quenching sites [38,39,.79,80]. In contrast, if NPs are fully covered dielectric layer, carrier losses and exciton quenching from NPs will decrease. So, the NBA, which has NPs isolated form polymer layer by the thermally evaporated MoO_3, prevents the device from recombination losses, while the exciton quenching can occur at Ag NPs placed in the flat PEDOT:PSS. Therefore, the NBA enhances device performance due to its superior optical as well as electrical properties compared to the widely using conventional plasmonic structure.

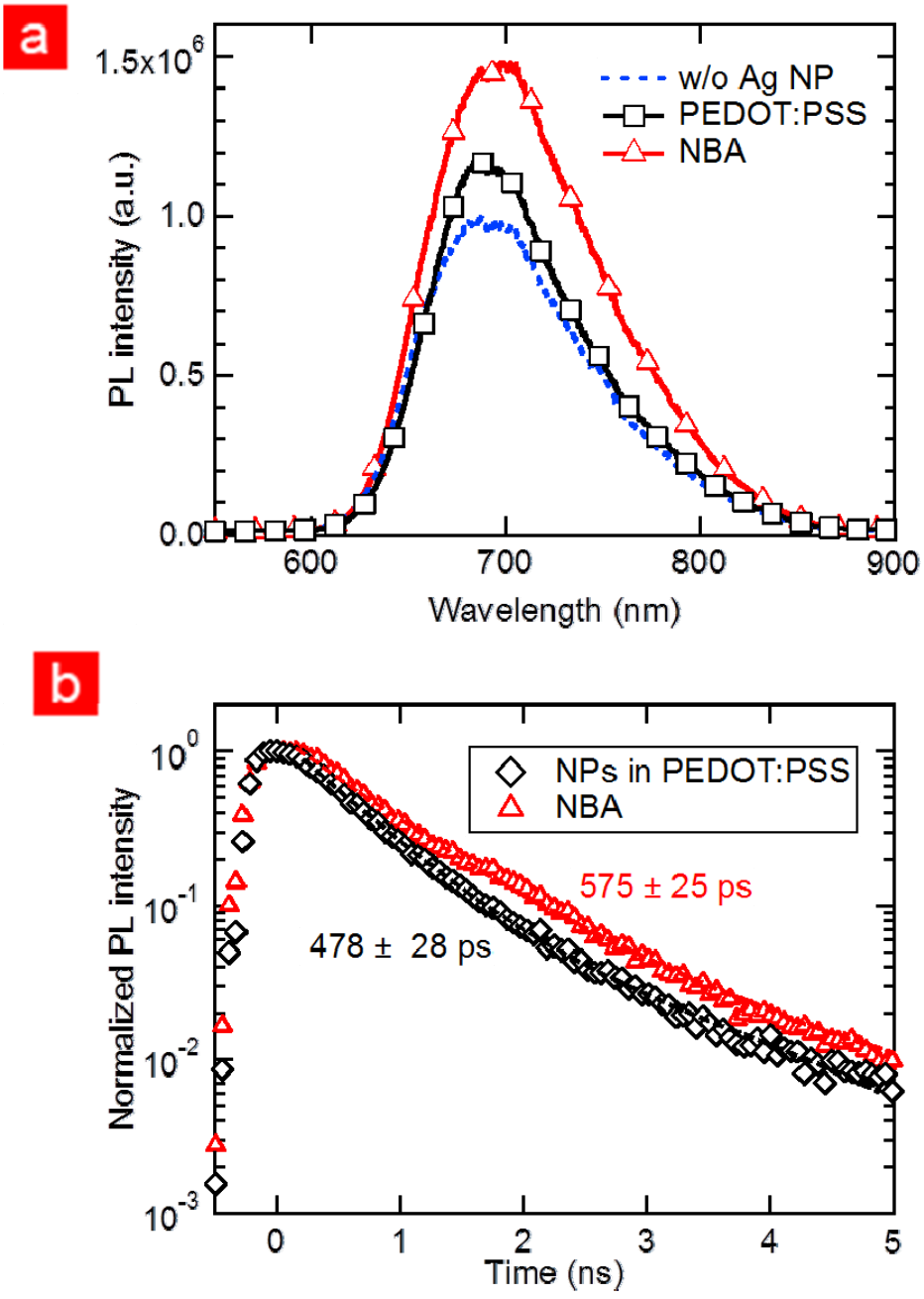

Figure 3.20 The (a) Steady-state and (b) transient PL of PCDTBT film with different plasmonic structure

3.4 The size dependence of plasmonic effect in NBA

It is widely known that the size of plasmonic nano structure is one of the key factors to control the optical properties of them. As a result, it has been studied the size dependence of optical effect in variety of plasmonic structure [57, 73,74].However, in previous work, the size of NPs was not precisely controlled due to inherent difficulty to manage to manage the size of NPs generated by wet-process and/or thermal evaporation method. In this sub chapter, the effect of NP size on device performance of OSC with NBA is studied to maximize the photocurrent improved by plasmonic effect, where NP size is precisely controlled. Here, the NBA are consisted of different sized NPs, 20 (NBA-20), 40 (NBA-40), and 60 nm (NBA-60), covered by 20 nm MoO_3. Then, the optical and electrical properties of the NBA employing different sized NPs were investigated by optical simulation, PL analysis, exciton generation rate and device performance.

3.4.1 Nano morphology of NBA including different sized NPs.

To check the size distribution of NPs for NBA, the Ag NP deposited substrate was examined by FE-SEM (× 50,000). Figure 3.21 is the SEM image of 20, 40 and 60 nm sized NPs deposited on the ITO via aerosol method. The SEM image confirmed that incorporated NPs, whose size are 20, 40, and 60,are uniformly deposited onto the substrate with small deviations of the sizes (σ). For example, σ of NP is 1.9, 2.9, and 2.5 nm for 20, 40, and 60 nm sized NPs, respectively. Compared

to average size of NPs is less than 10%, so that it is expected that the effect of NPs on the optical properties can be accurate exploited in this analysis.

The nano-morphology of NBA having different size NPs is studied by cross-sectional TEM image and their corresponding EDS data, as shown in Figure 3.22. The EDS mapping images of Ag and Mo in the NBA enclosing by 20 nm MoO_3 revealed the successful formation of the NBA regardless of NP's size. The cross-sectional TEM images also have revealed that the 20 nm thick MoO_3 bumps are uniformly deposited over variety sized NP on the ITO surface and well follow the underlying structure of Ag NPs. Small-sized NPs (smaller than 40 nm) were fully enclosed by the 20 nm MoO_3. On the other hand, the lower part of large sized NPs (bigger than 60 nm) was barely covered by the dielectric layer owing to the directionality of a thermal evaporation process. Therefore, the NBAs including different size NPs have an oval shape and NPs are perfectly isolated from the polymer layer.

To clarify the encapsulation status of NPs in NBA, the transient PL analysis was conducted, which reflects the exciton decays in polymer layer. The Figure 3.23 shows the transient PL of PCDTBT film casted on the NBA including 20, 40, and 60 nm size NPs. Here the wavelength of PL is 690 nm and the film is excited by 405 pulse laser. The resolution of this measurement was 55 ps. Exciton lifetimes for all the samples deduced from exponential function1 are similar to each other regardless of the NP's sizes. Additionally, the lifetime of exciton of polymer with NBA is almost the same as that of film without NBA. Previous researches reported that if the NPs were not fully encapsulated by dielectric layer, the exciton lifetime would be shortened because they act as exciton quenching sites [63]. Consequently it is apparent that Ag NPs up to 60 nm are fully covered with 20 nm thermally evaporated MoO_3, which is not a source for deteriorating device performance.

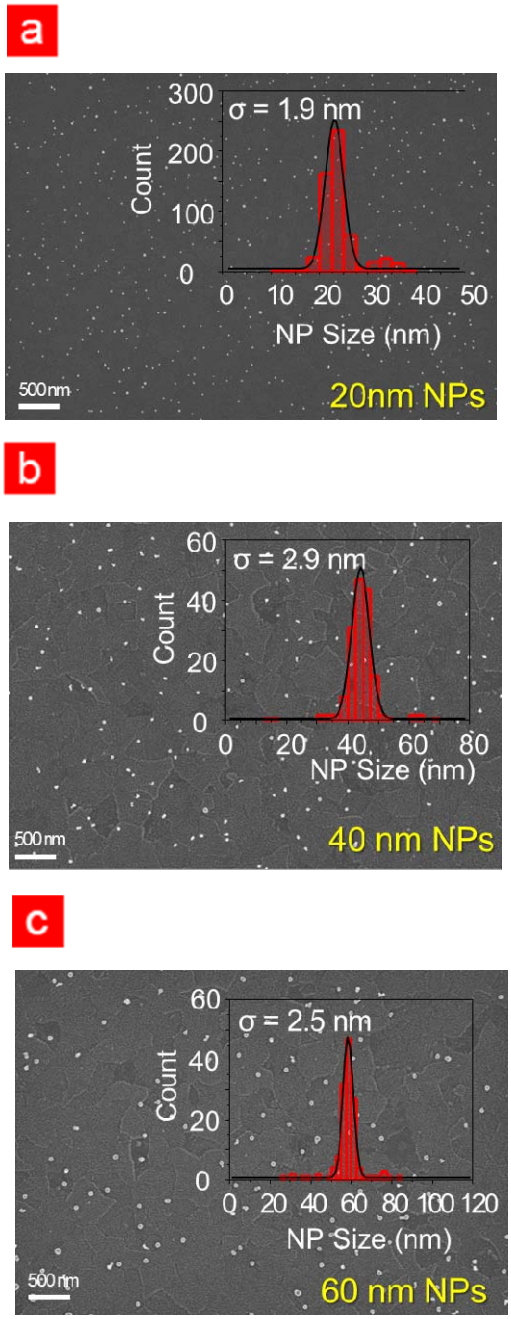

Figure 3.21 FE-SEM images of (a) 20, (b) 40, and (c) 60 nm sized NP deposited substrate. The inset of image is the size distribution of NPs, whose average size is similar to the targeted one

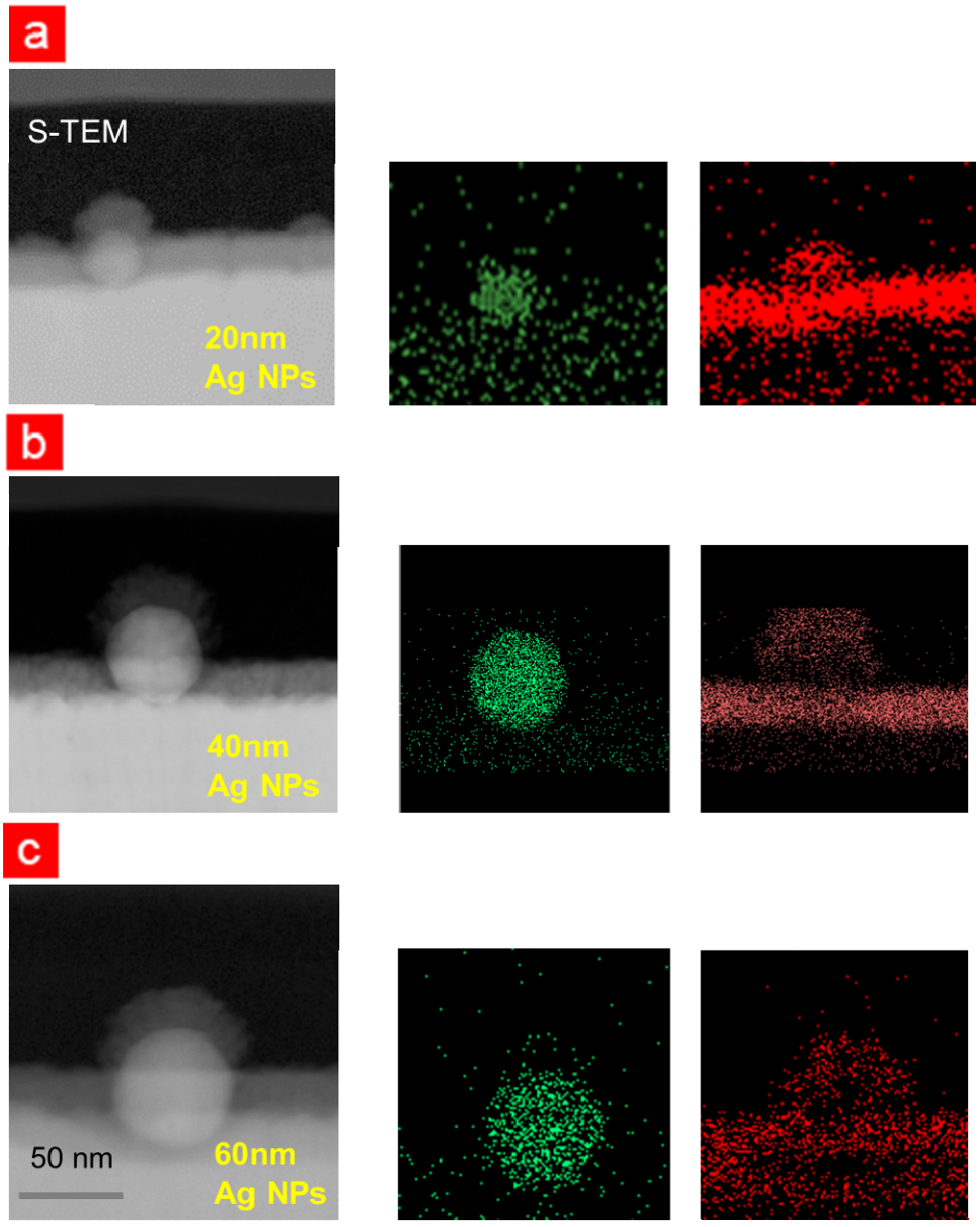

Figure 3.22 Cross-sectional TEM and its corresponding EDS images of NBA consisting of (a) 20, (b) 40, and (c) 60 nm sized NP

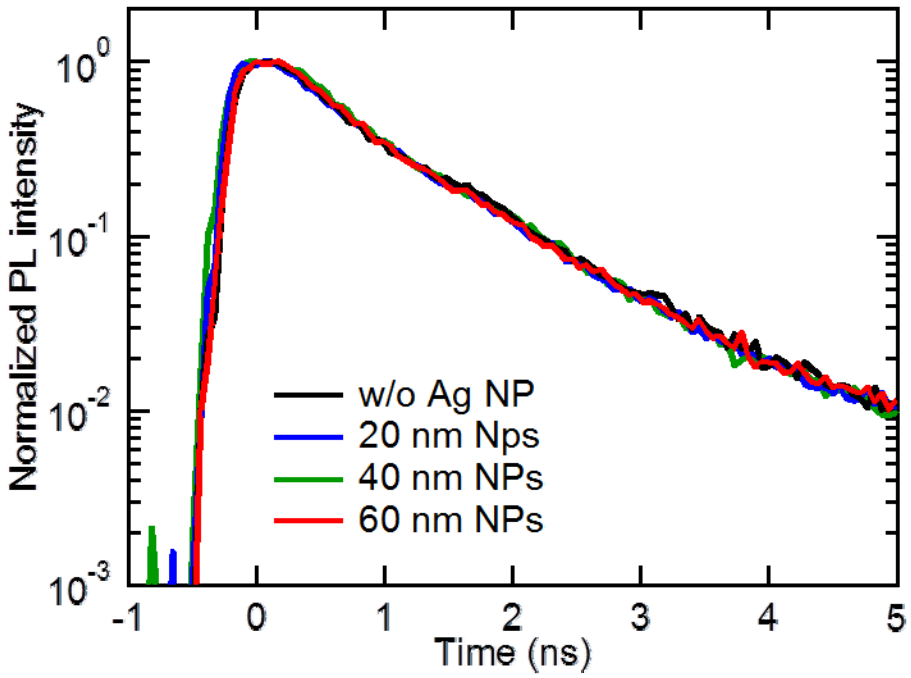

Figure 3.23 Time-resolved PL of film with and without NBA. The size of NPs are 20, 40, and 60 nm

3.4.2 Optical simulation of NBA including different sized NPs.

The plasmonic effect of NBA including different sized NPs was calculated by 3D-FDTD optical simulation considering real device structure. Figure 3.24 illustrates the ratio of scattering (scat CS) to absorption cross-section (abs CS) induced by NBA. The schematic for simulation is shown in Figure 3.24 (a), where the MoO_3 enclosed NPs are located the interface between polymer layer and air. Simulated results denote that the scat CS peaks are red-shifted, as the size of NP is enlarged from 20 to 60 nm. For example, a spectral change of 50 nm in scat CS peak

of the NBA is exhibited as the diameter of NPs increases from 20 to 60 nm, as shown in Figure 3.24 (b). Interestingly, the enhanced scat CS peak is observed in the spectral range of 450 to 600 nm, which is overlapped with the main absorption band of the polymer blend.

Additionally, the ratio of scat CS to abs CS for the NBA containing20, 40, and 60 nm sized NPs are 0.15, 0.61 and 1.20, respectively. (See Figure 3.24 (c)) That is the ratio increase as the size of NP in NBA increase. Generally, the abs CS represents the amount of absorption of light from NP itself, which is not contributed to the photo current. On the other hand, the scat CS is related with the scattering of light by NP, which increase light absorption of surrounded media. Thus, it will be expected that the absorption of polymer layer containing large sized NP is much higher than that of film with small sized NPs.

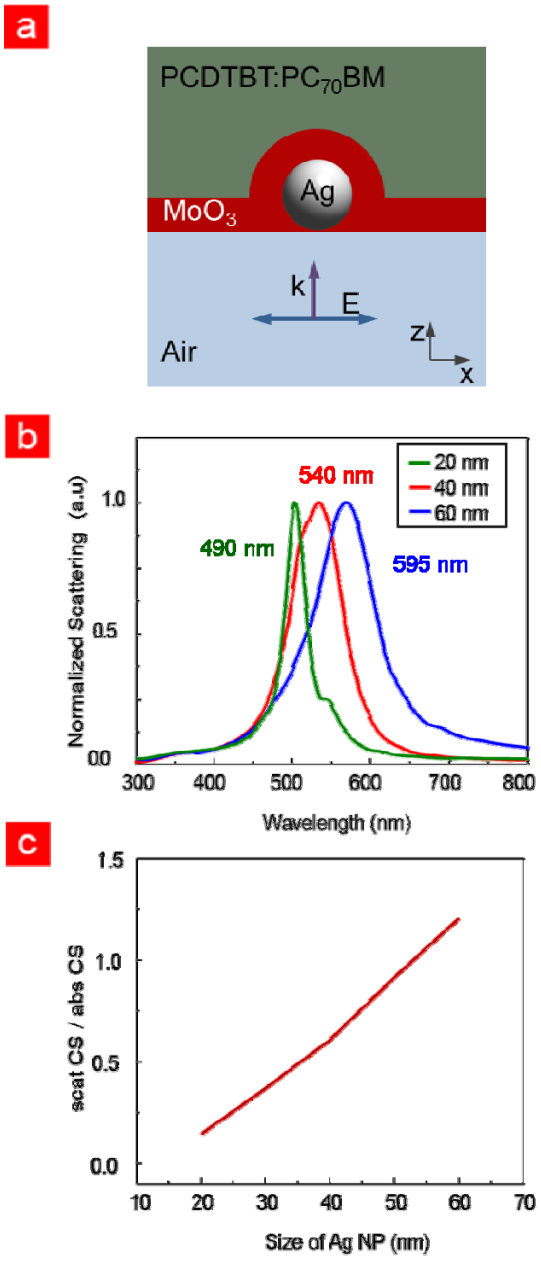

Figure 3.24 (a) The schematic of structure for optical simulation (b) The normalized scattering intensity in the NBA including different sized NPs. (c) The ratio of scattering to absorption CS as a function of NP's size in the NBA , The wavelength marked in (b) is the peak of scattering value

3.4.3 Device performance of OSC with NBA consisted of different sized NPs.

The optical simulation showed that the plasmonic effect from large sized NPs is higher than that induced by small-sized one. To quantify the effect of the NBA on device performance of OSC embedding different sized NPs, 20, 40, and 60 nm, were compared to each other. The Figure 3.25 shows the J-V characteristics of OSCs with and without the NBA taken under1 sun condition (AM1.5G, 100 mW/cm^2 illumination). And the average photovoltaic parameters of OSC with 20, 40, and 60 nm sized NPs, derived from 6 different samples, are summarized in Table3.4. The PCE of the devices with NPs is improved from 5.07% (OSC without NPs) to 5.62% (20nm NPs), 5.87% (40nm NPs), and 5.37% (60nmn NPs), respectively. This enhancement is mainly attributed to the improvement in photocurrent from 9.12in the case without NPs to 10.04 (20 nm NPs), 10.43 (40 nm NPs), and 11.11 mA/cm2 (60nm NPs), accordingly. Particularly, the photocurrent increases proportion to the size of incorporated NPs. The enhancement ratio for each case is 10.0 %, 14.3%, and 21.8% for OSC containing 20, 40 and 60 nm NPs, respectively. This result is consistent to the optical simulation results, the increased scattering cross-section intensity of the NBA structure with larger-size NPs.

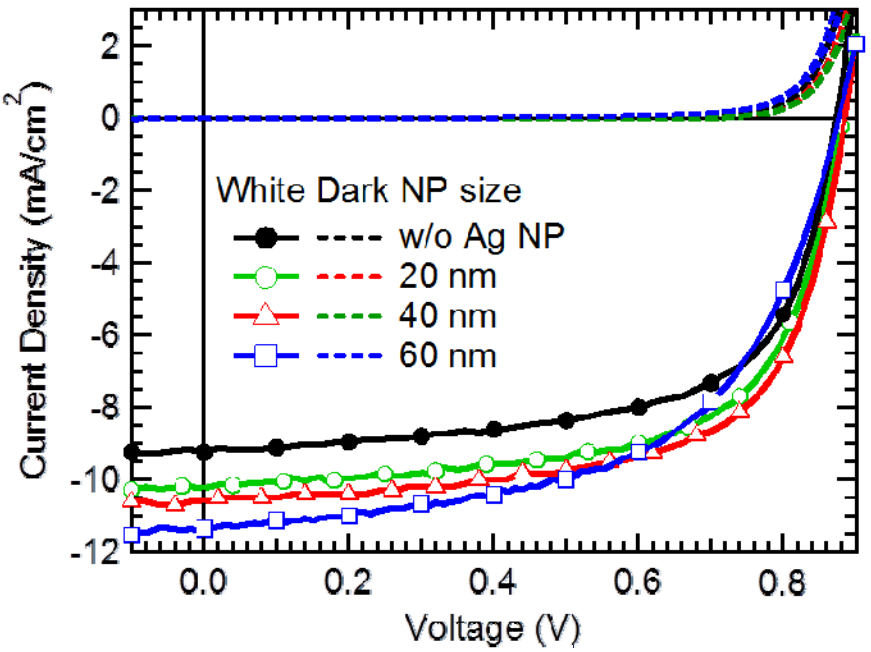

Figure 3.25 J-V characteristics of device with NBA under 1 sun and dark condition. Here the size of NPs in NBA varies from 20 to 60 nm

Table 3.4 The device performance of OSC-NBA with different sized NPs. The average and standard deviation values of the photovoltaic parameters are achieved from 6 different batches

	NPs	J_{SC} (mA/cm^2)	V_{OC} (V)	FF	PCE (%)
OSC-NBA	-	9.12±0.10	0.88±0.01	0.64±0.01	5.07±0.08
	20 nm	10.04±0.09	0.88±0.01	0.64±0.01	5.62± 0.15
	40 nm	10.43±0.12	0.88±0.01	0.64±0.01	5.87± 0.17
	60 nm	11.11±0.24	0.87±0.01	0.55±0.02	5.37± 0.26

To explore the origin of photocurrent, the exciton generation rate in OSC with and without NBA is derived by the relationship between photocurrent (J_{ph}) and effective voltage (V_{eff}), as shown in Figure 3.26 and Table 3.5. The definition of J_{ph} and V_{eff} are following equation

$$J_{ph} = J_L - J_D \tag{3.2}$$

$$V_{eff} = V_o - V_a \tag{3.3}$$

where J_L and J_D are the current density of device under 1sun and dark condition, VO is the voltage when the J_{ph} reaches zero, and V_a is applied voltage. V. D. Miihailetchi et al. reported that the maximum exciton generation rate (G_{MAX}) can be expressed using saturation current (J_{sh}), single electron charge (q) and device thickness (L),

$$J_{sat} = q\, G_{MAX}\, L \tag{3.4}$$

Here, the J_{sat} is the photo current density at high reverse bias.

By applying equation (3.4) to the plasmonic OSC with NBA, the exciton generation inside device is derived. The G_{MAX} for each sample are denoted in Table 3.4. The deduced G_{MAX} increases as the size of NPs in NBA increases. This result is in a good agreement with the J_{SC} enhancement in devices employing the NBA. Therefore, it is apparent that large-sized NPs in OSC increase the generation of exciton by enhancing local electric field.

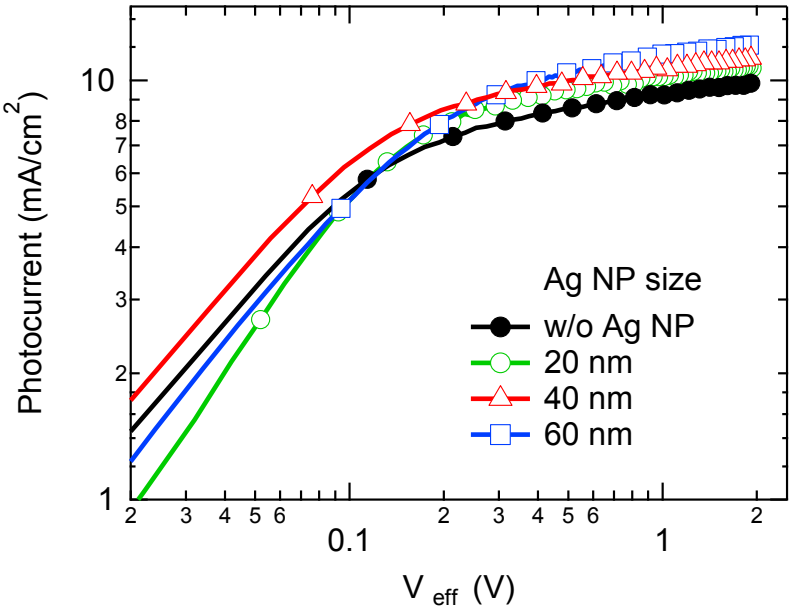

Figure 3.26 Photocurrent vs effective voltage (V_{OC}) of OSC with and without NBA

Table 3.5 Maximum exciton generation rate of OSC and their corresponding enhancement ratio compared to the OSC without NPs

	NPs	Exciton generation rate ($m^{-3}S^{-1}$)	Enhancement ratio
OSC-NBA	-	5.6×10^{27}	
	20 nm	6.1×10^{27}	8.8 %
	40 nm	6.4×10^{27}	14.8 %
	60 nm	6.9×10^{27}	23.4 %

The steady-state PL of films with and without NBA, denoting the overlap between the absorption band of polymer and the plasmonic resonance, is another supporting evidence for increased light absorption in the OSC with NBA. The Figure 3.27 is the steady state PL of PCDTBT film (80nm) casted on the NBA, whose NP's size is varied from 20 to 60 nm. Here the film was excited by 405 nm laser. The intensity of PL increases as the size of NP increases. As shown in Figure 3.20, the lifetime of exciton of film with different sized NBA is so similar among them, that the enhanced steady-state PL is mainly originated from enhanced excitation of PCDTBT film. It means that the plasmonic effect arose from large-sized NP is much higher than that from small-sized NPs. These results coincide with the optical simulation and photo-current of device.

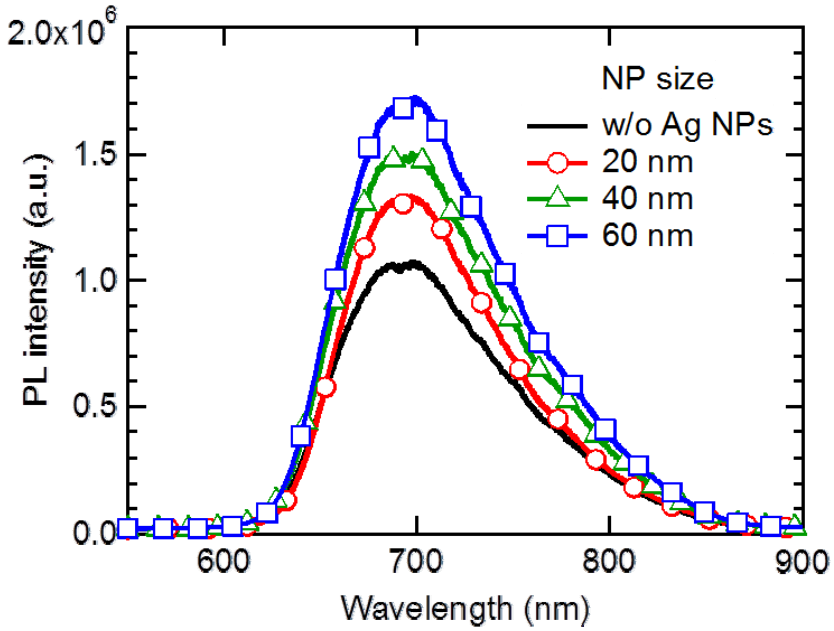

Figure 3.27 Steady state PL of film with and without NBA

For analyzing the spectral response of NBA with different size NPs, the IPCE of device was conducted, as shown in Figure 3.28 (a). The IPCE result shows that higher IPCE of OSCs with the NBA compared to that of reference sample is the origin of the enhancement in J_{SC}. For systematical analysis of plasmonic effect from the NBA with different sized NPS, the enhancement ratio of IPCE is derived by dividing the IPCE of OSC with by NBA that of OSC without NBA as illustrated in Figures 3.28 (b). There are three unique features in the IPCE and its corresponding enhancement ratio of OSC.

First, the wavelength of the peak in IPCE enhancement ratio in the region of 400-650nm, is red-shifted with enlarging NPs. For instance, the peak wave length for OSC with NBA containing 20, 40, and 60 nm sized NPs are 465, 490 and 520 nm, respectively. Despite slightly different distribution of NPs between a calculated model and empirical real device, the IPCE result is well matched with simulated result. The result of the IPCE peak dependence of NP's size has been by the precisely controlled size of NPs with small aggregation in the NBA through the aerosol process.

Second, the enhancement ratio of IPCE in 400- 600 nm wavelength region increases as the size of NPs increases. This result is consistent with the result of simulation, shown in 3.24 (c), which denotes the ratio of scat CS to abs CS increase proportion to the size of NPs. The highest enhancement ratio of each deviceincreasesby21%, 28%, and 30% in OCS with 20, 40, and 60 nm sized NPs, respectively. Since, the electrical enhancement, owing to the combination of an enlarged surface area and undulated active layer, was not considered in the optical simulation, the enhancement ratio in empirical IPCE is higher than that of the calculated one.

Lastly, there is additional enhancement peak at the red region (650 to 800 nm) in the experimental result, which is exhibited in the simulated absorption data shown in Figure 3. 19, which is not observed in the simulation result of the film without reflective electrode. It means that the multi-reflection between the NBA and the reflective electrode is also occurred in the OSC-NBA, regardless the size of NPs However, the absolute increased IPCE of the PCDTBT:$PC_{70}BM$ in this region is too low to improve eJ_{SC} substantially, owing to low absorption of polymer blend at this region. If the OSC-NBA is consisted with near IR absorbing materials, further improvement in photocurrent is expected.

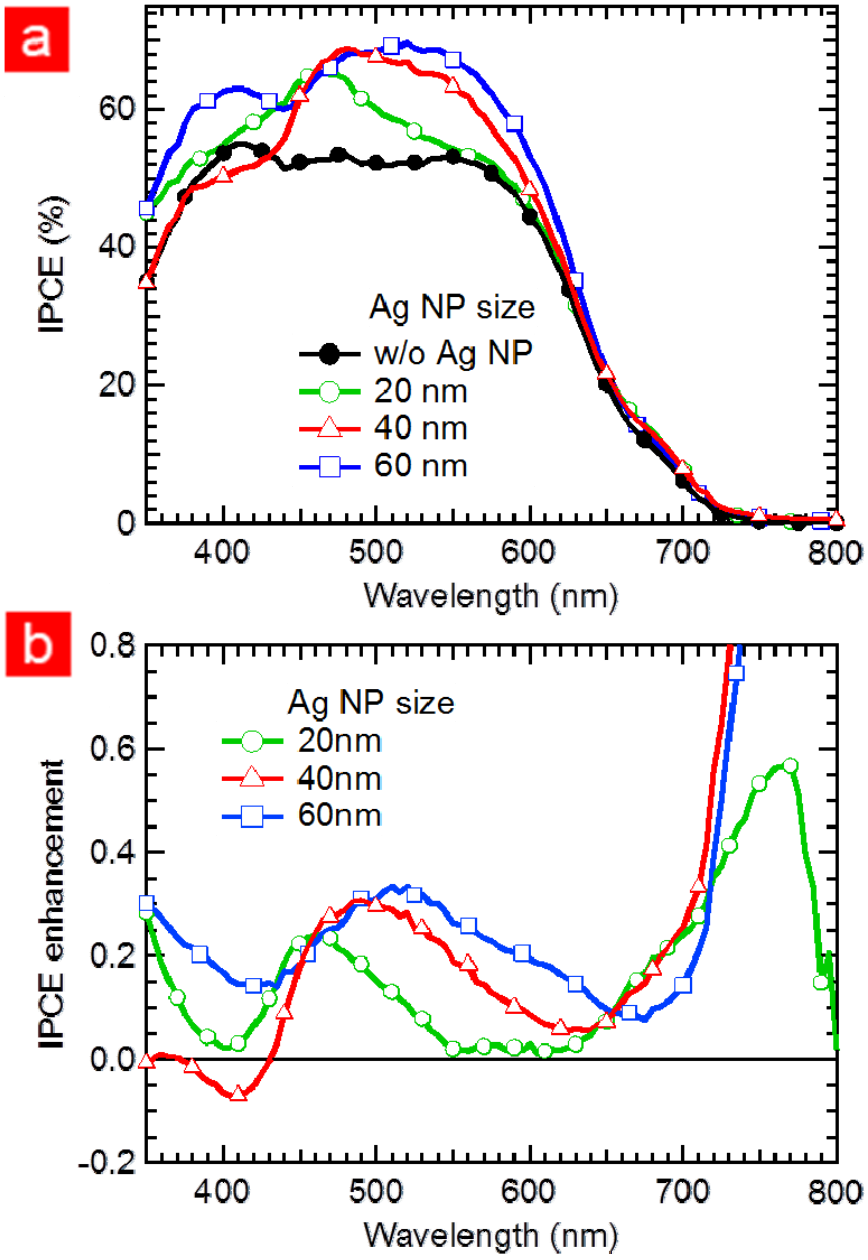

Figure 3.28 (a) IPCE and (b) its corresponding enhancement ratio of OSC with and without NBA. Here, the enhancement ratio is derived the IPCE with OSC-NBA with respect to the OSC without NBA

In spite of excellent optical properties of large sized NPs, leading to the highest J_{SC}, the PCE of OSC-NBA with 60 nm Ag NPs is lower than those of others. This problem is mainly caused by the low FF of OSC-NBA including 60 nm sized NPs. Generally, the FF is determined by leakage and ohmic losses inside device [64]. To find the origin of low FF, the semi-log J-V characteristics under dark condition, reflecting leakage losses, were performed, as shown in Figure 3.29 (a). The dark current of OSC-NBA with 60 nm sized NPs at the high reverse voltage (-1 V) was one-hundred times higher than those of the other devices. Since the NPs are not exposed to the polymer blend, this leakage may be caused by thin active layer (~ 40 nm) on the top of NBA (Figure 3.29 (b)). It has been reported that the drop of FF is observed in plasmonic devices employing highly concentrated NPs[81,82]. For improving FF of OSC-NBA with 60nm Ag NPs, the OPV with low concentrated60nm sized NPs (~0.5% of surface coverage) was compared with that of the OSC-NBA containing high density NPs. The PCE of OSC with low concentrated Ag NPs is 5.67%, arose from the high FF of 0.65. But, in this case, the plasmonic effect decreases owing to decreased number of NPs, resulting in the decreased J_{SC} (10.25 mA/cm^2) compared to the that of OSC-NBA including highly concentrated NPs This is consistent with previously reports based on experimental and simulation data for the OSC incorporating NPs.[66].Consequently, the leakage current arising from the short distance between the cathode and the bumped anode degrades the device performance in spite of the increased Jsc due to the enhanced plasmonic effect from the large-size NPs.

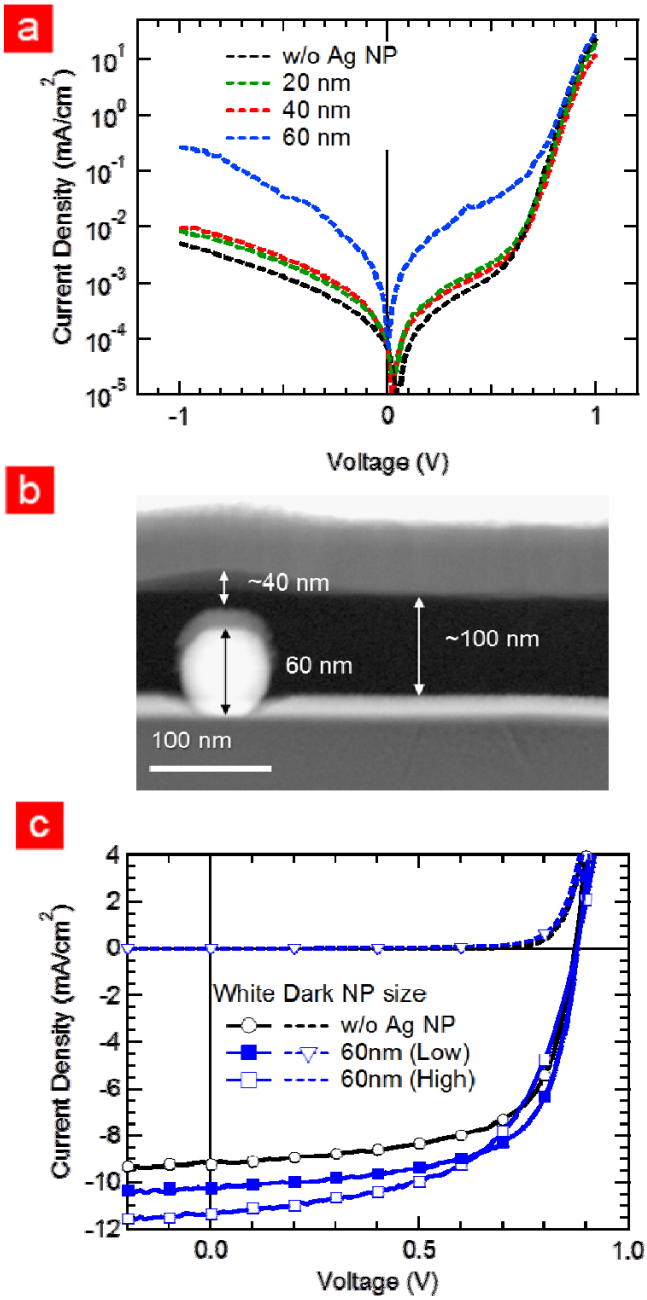

Figure 3.29 (a) Semi-log J-V characteristics of OSC with and without NBA under dark condition. (b) Cross-sectional TEM image of OSC-NBA including 60 nm Ag NPs. (c) J-V characteristics of OSC-NBA with different concentrated 60 nm Ag NPs

3.5 Summary

In this chapter, the novel plasmonic OSC with NBA is demonstrated. The NBA is consisted of the aerosol derived, precisely size controlled, Ag NPs and thermally deposited MoO_3, following the underlying structure, thereby resulting in the combination of NPs and textured buffer layer. The OSC-NBA shows a considerable enhancement in J_{SC} and PCE regardless the active layer materials. The optical simulations, scattering cross-sections and near field distribution inside the active layer, show higher intensities with a strong forward scattering effect in the OSC with the NBA than those with the flat PEDOT:PSS. Additionally, multi-reflection enhances the absorption of active layer sandwiched by the cathode and the nano bumped anode. As a result, the OPV-NBA presents better performance than those with OSC-FP, consisted of PEDOT:PSS incorporating NPs, arose from improved absorption intensity with smaller recombination losses. Furthermore, the J_{SC} of OSC-NBA containing different size increases as the size of NPs increases. Besides, the enhanced wavelength induced by NBA can be controlled by changing the size of NPs. However, the increased leakage losses of device with large-sized NPs negate to transfer enhanced absorption to the enhancement in PCE. Therefore, this approach can be a promising platform to harness light efficiently and to control plasmonic peak easily in diverse OSCs.

Chapter 4

Plasmonic Effect and Carrier Dynamics of Organic Solar Cells with Nanobump Assembly

Implementing noble metallic NPs and nano structure in OSCs is a widely using strategy to enhance light absorption induced by plasmonic effect as well as to improve electrical properties arose from the high carrier mobility of NP and well-aligned energy levels with an active layer [31]. However, the role of NPs and nanostructures is still on debate, since the increased light absorption and electrical improvement caused by them is not always channeled into highly efficient devices [59, 83]. According to previous reports, a direct contact between organic semiconducting layer and metal facilitates non-radiative energy transfer inside active layer, thereby resulting in degraded device performance [79].What's worse,

metal-mediated recombination losses in NPs occur inside the polymer based optoelectronic devices with metallic nanostructures [59,80,83]. Regarding these negative effects induced by implementing metallic nanostructure in organic devices, dielectric encapsulated NPs has been suggested to optimize energy converting efficiency of device by minimizing side effects [35,37].

Nevertheless, it has been reported that the competition between optical field enhancement and carrier annihilation by NPs is still exhibited the plasmonic device with dielectric coated NPs [83]. Besides it is not clear the role of NPs depending on the encapsulation status. Even though, some studies predicted the relationship between the thickness of passivation layer and device performance where the refractive index of encapsulation layer (SiO_2) was lower than that of active layer, but the optical and electrical effects of the NPs enclosed by high refractive index material (MoO_3, n= ~2.0) has not been studied. Thus, in this chapter, the optical and electrical effect of NBA on device performance is analyzed by controlling encapsulation status of NPs. This study will be a guideline to design efficient plasmonic OSCs with NPs.

4.1 The control of NP's encapsulation status

To monitor the control of NP's encapsulating status in NBA depending on thickness of MoO_3 (d_{MoO3}), cross-sectional TEM analysis of OSCs (ITO/ NBA/ PCDTBT:$PC_{70}BM$/ LiF/ Al) was performed. Here, the size of NPs (40 nm) is fixed, while theMoO_3 are varied from 5 to 30 nm, since 40nm NPs shows excellent optical properties without deteriorating device performance, as shown in chapter 3.4.

Figure4.1 illustrated nano morphology of NBA with 5, 10, 20, and 30 nm MoO_3 layer. All cases, the upper parts of NPs are covered by $MoO_3$with targeted thickness. Meanwhile, lower parts of them are partially disclosed when the $d_{MoO3}$is 5 and 10 nm. The ratio of uncovered NP's surface area, exposing to the polymer blend, calculated by cross-sectional TEM image, is approximately 60% and 25% for NBA with 5 and 10 nm MoO_3, respectively. In contrast, NPs in NBA with 20 and 30 nm MoO_3 are fully encapsulated by dielectric layer. Moreover, the side of NPs are barely covered by 4 and 7 nm MoO_3 in the case of NBA with 20 and 30 nm sized MoO_3, respectively. Despite different d_{MoO3}, the shape of NBA is an oval shape due to the shadowing effect of NPs during MoO_3 thermal deposition process. Hence, cross-sectional TEM image guarantees that the encapsulation status of NPs is able to control by managing d_{MoO3}, which is difficult to realize for the case of solution process.

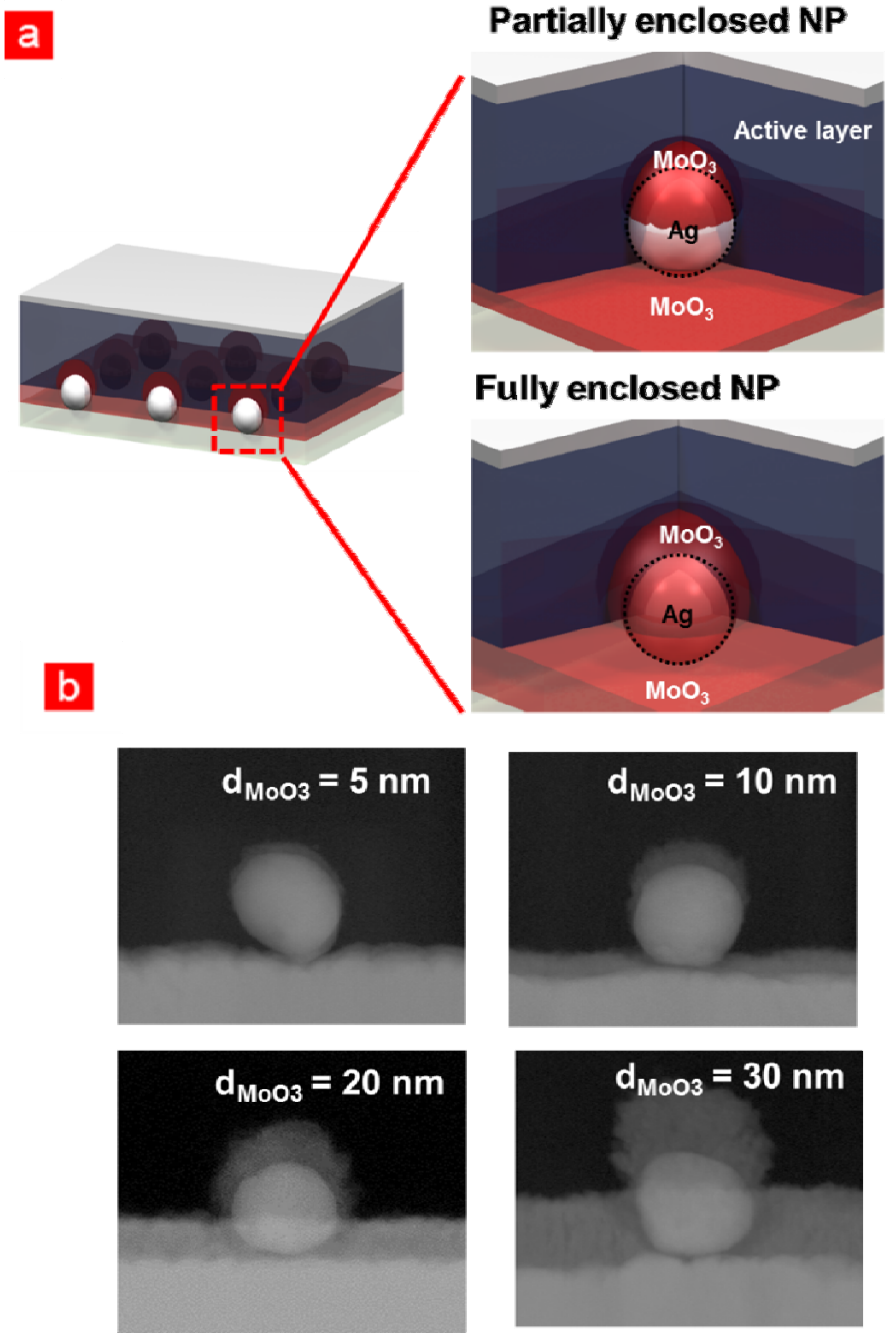

Figure 4.1 (a) Schematic of fully and partially encapsulated NPs (b) Cross sectional TEM image of NBA with different d_{MoO3}

For quantitative investigation of encapsulation status, X-ray photoemission spectra(XPS) were conducted for the NBA with different d_{MoO3}. Generally, XPS denotes the amount of specific atoms in the surface. In this case, the XPS for NBA with different $d_{MoO3}$was performed at the region 365– 375 eV, where is corresponding to the energy of the Ag $3d^{5/2}$ (369 eV) and Ag $3g^{3/2}$(374eV)[84]. As shown in Figure 4.2, the intensity of Ag peak was diminished as the d_{MoO3}increased in both energy level of Ag $3d^{5/2}$ and Ag $3g^{3/2}$. Moreover, it is apparent that the NPs with 20 nm d_{MoO3} was perfectly encapsulated, since the peak intensity for the case of 20 and 30 nm was almost same. The intensity for NBA with thick d_{MoO3} might be not zero, due to the penetration length of X-ray source, which penetrate few nanometers. (less than 10 nm). Consequently, the XPS and TEM analysis clearly shows that the encapsulation status can be controlled by tuning d_{MoO3}.

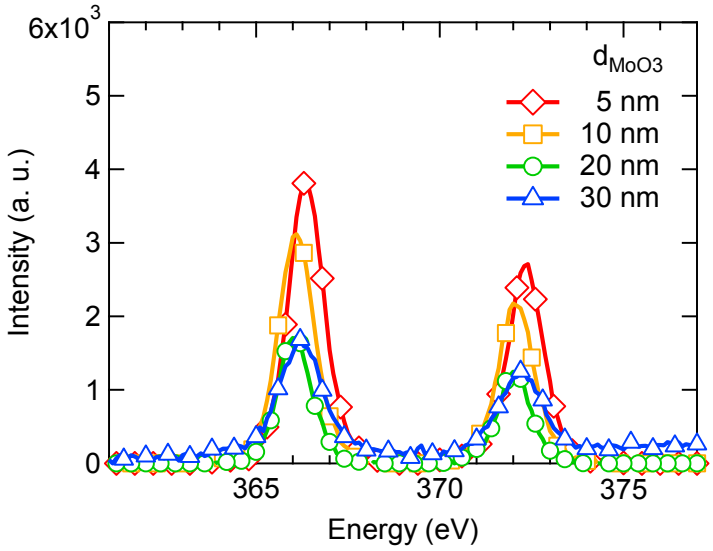

Figure 4.2 XPS spectra of films with NBA including different d_{MoO3}

4.2 Device Performance of OSC with NBA Depending on the Encapsulation Status of NPs

Figure 4.3 shows the J-V characteristics and their trend of OSCs with and without NBA employing different d_{MoO3}. And the photovoltaic parameters, of them J_{SC}, V_{OC}, FF, and PCE, were summarized in Table 4.1. Here the device structure was ITO/ NBA or flat MoO_3 /PCDTBT:$PC_{70}BM$ /LiF /Al. Device parameters of OSCs without NBA are in a similar range when the d_{MoO3} is thinner than 20 nm. In contrast, the PCE of device without NBA including 30 nm d_{MoO3} (4.61 %) was lower than those of the others. This is caused by reduction of FF (0.58). This result is consistent with the previous studies employing P3HT: PCBM, which described the device performance of OSC with thick MoO_3 (thicker than 30 nm) decreased as a result of reduced FF [85].

Meanwhile, the PCE of OSC-NBA containing 20 nm d_{MoO3} (5.79%) is higher than that of OSC including the same d_{MoO3} (5.12%). This enhancement is mainly attributed to the increased $J_{SC,}$ which is already pointed out in Chap 3.2. Also, in the case of OSC-NBA with 30 nm $d_{MoO3,}$ the enhancement in the PCE is exhibited, which arises from enhanced FF (0.62) in comparison with the case of OSC without NBA (PCE: 4.61%, FF: 0.58). However, the OSC inserting partially covered NPs intriguingly shows reduced PCE. For instance, the PCE of OSC with NPs covered by 5 and 10 nm d_{MoO3} were 3.30% and 4.70%, respectively. In these cases, the drop of FF and V_{OC} was exhibited without increasing $J_{SC.}$ It means that these photovoltaic parameters of OSCs embedding partially encapsulated NPs ($d_{MoO3} \leq$ 10 nm) degrade as the d_{MoO3} decreases. The device performance of OSC-NBA with thin

d_{MoO3} is discordance with previous works, demonstrating that the exciton generation increases as the distance between NPs and organic material decreases [86, 87]. To reveal why the device performance was changed depending on the NP's encapsulation status, the optical and electrical properties of OSC induced by NBA were analyzed in aspects of exciton generation, exciton dissociation, and carrier transport.

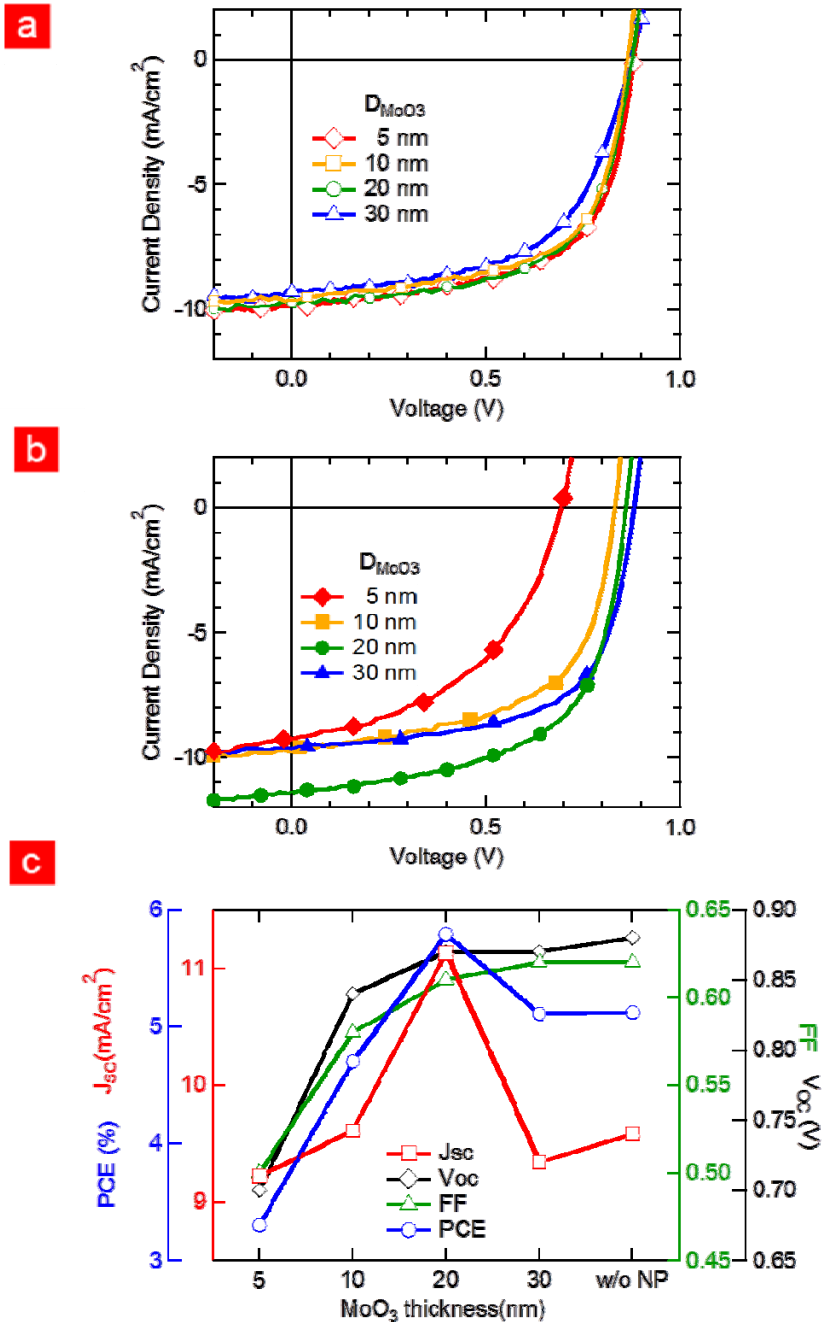

Figure 4.3 J-V characterisitics of the device (a) with and (b) without NBA including d_{MoO3}. (c)The phtovolataic parameters of device as a function of d_{MoO3}.

Table 4.1 Photovoltaic parameters of OSC with and without NBA containing different d_{MoO3}.Here the average and deviation value is achieved from 10 different samples.

D_{MoO3}	NPs	J_{SC} (mA/cm^2)	V_{OC} (V)	FF	PCE (%)
5 nm	-	9.61±0.18	0.88±0.01	0.62±0.01	5.24±0.18
	NBA	9.22±0.13	0.70±0.03	0.50±0.04	3.30± 0.28
10 nm	-	9.55±0.09	0.87±0.01	0.61±0.01	5.11± 0.04
	NBA	9.61±0.18	0.84±0.02	0.58±0.01	4.70± 0.21
20 nm	-	9.58±0.15	0.87±0.01	0.61±0.01	5.12± 0.13
	NBA	11.13±0.24	0.87±0.01	0.60±0.01	5.79± 0.13
30 nm	-	9.19±0.13	0.86±0.01	0.58±0.01	4.61± 0.13
	NBA	9.34±0.24	0.87±0.01	0.62±0.01	5.11 ± 0.27

4.3 Optical Properties of NBA Induced by Partially and Fully Encapsulated NPs

To explore optical effect induced by NPs on the absorption of fim, the UV-visible absorption spectra of polymer films casted on the NBA was compared with that of without NBA, as presented in Figure 4.4 (a). Here, the film was consisted of PCDTBT:$PC_{70}BM$ mixture (100 nm) and the density of NPs was approximately 3.0 $\times$ 10^9 /cm^2. First of all, it is observed that the absorption of film with NBAis higher than that of the film without NBA. Especially, there is distinctive enhancement in the absorption at the range of 450 to 650 nm. This region is consistent with theoretical and empirical results, plasmon resonance of NBA. However, the change of absolute absorption of film without NBA depending on the d_{MoO3} makes it difficult to compare the optical effect from different d_{MoO3}in NBA. For more clear investigation, the integrated enhancement ratio of film absorption induced by NBA (IER) was calculated as shown in Figure 4.4 (b). The ratio was derived by the considering of solar spectra under 1 sun condition (AM 1.5G), as described following equation.

$$\text{Integrated enhancment ratio (IER)} = \frac{\int_{380\,nm}^{720\,nm} Absorrption\ of\ film\ with\ NBA\ (\lambda) \times \text{solar spectrum intnesity}\ (\lambda)\ d\lambda}{\int_{380\,nm}^{720\,nm} Absorbtion\ of\ film\ without\ NBA\ (\lambda) \times \text{solar spectrum intnesity}\ (\lambda)\ d\lambda} \quad (4.1)$$

Interestingly, the IER is inverse proportional to the d_{MoO3}.For instance, the average IER of film with 5, 10, 20 and 30 nm d_{MoO3} are 11, 10, 9, and 3%, respectively. The decrease of IER depending on d_{MoO3}agrees with the previous reports, where NPs were covered by low index material, SiO_2 [88,89]. However, the change of IER was less than that of previous works, which might be caused by the substitution of dielectric layer, covering metallic NP. In this case, relative high refractive index material, MoO_3 (n = ~2.0), was used to encapsulated NPs, while the SiO_2, whose value is approximately 1.5, was covered NPs.

For understanding underlying mechanism, the origin of the enhancement in absorption arose from NBA, optical simulations were also conducted. Figure 4.5 shows the scattering cross section intensity of NBA with different d_{MoO3}. It is apparent that the main scattering peak by NBA is around 550 nm, similar with the empirical absorption peak. Additionally, the broad scattering effect was exhibited in simulation results, which coincides with the empirical absorption data. Interestingly, the intensity of scattering among samples was very similar to each other, despite the differentd_{MoO3}. This result is contradictory with the IER data, which decrease as the d_{MoO3} increase. The refractive indices of MoO_3 and PCDTBT:PC_{70}BM is so modest, that the scattering ratio holds in similar region. Hence, the dependence of IER on the $d_{MoO3}$is not originated by scattering effect of NBA including different d_{MoO3}

Next, the other optical effect arising from NBA, plasmonic effect, was analyzed by using calculated electrical field distribution near NPs by 3D-FDTD method. The Figure 4.5 (b) showed that the electrical field distribution near NPs is also improved, which is mainly originated from the LSPR effect induced by NPs. Differ from the scattering calculation, this enhancement in electrical field occurred only nearby NPs, so that the most of this improvement lies in MoO_3 in the case with thickd_{MoO3} (30 nm). Since, the near field enhancement with LSPR only penetrates a few tens of

nanometers, the LSPR reaches in the vicinity of NPs and its intensity exponentially decays. Thus, the IER from NBA is inverse proportional to the $d_{MoO3.}$

Considering these two simulation results, LSPR and scattering effect induced by NBA incorporating d_{MoO3}, the enhancement in J_{SC} of OSC-NBA with 20 and 30 nm d_{MoO3}can be understood by the increased generating excitons arose from the enhanced absorption by the NBA. However, in the OSC-NBA with thin encapsulation layer (d_{MoO3}= 5 and 10 nm), the improved absorption from plasmonic structure was not transferred into the enhancement in J_{SC}. This means that the degraded device performance of OCS-NBA with thin $d_{MoO3}$is not only explained by the optical properties of the plasmonic structure. In the next chapter, the electrical effect depending on $d_{MoO3}$is investigated.

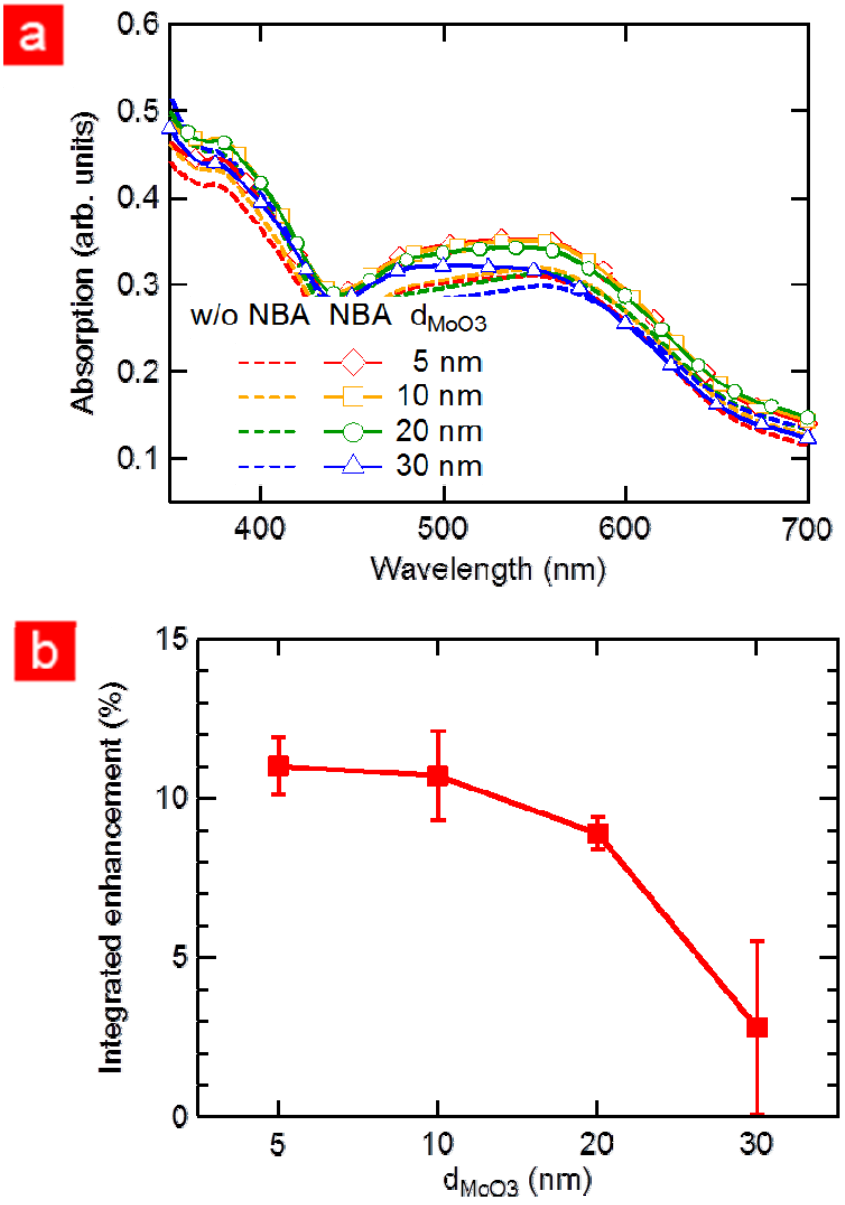

Figure 4.4 (a) The absorption spectra of 80nm PCDTBT:$PC_{70}BM$ film with and without NBA including different $d_{MoO3}$and (b) the absorption enhancement ratio of each case by considering the solar spectrum under 1 Sun condition

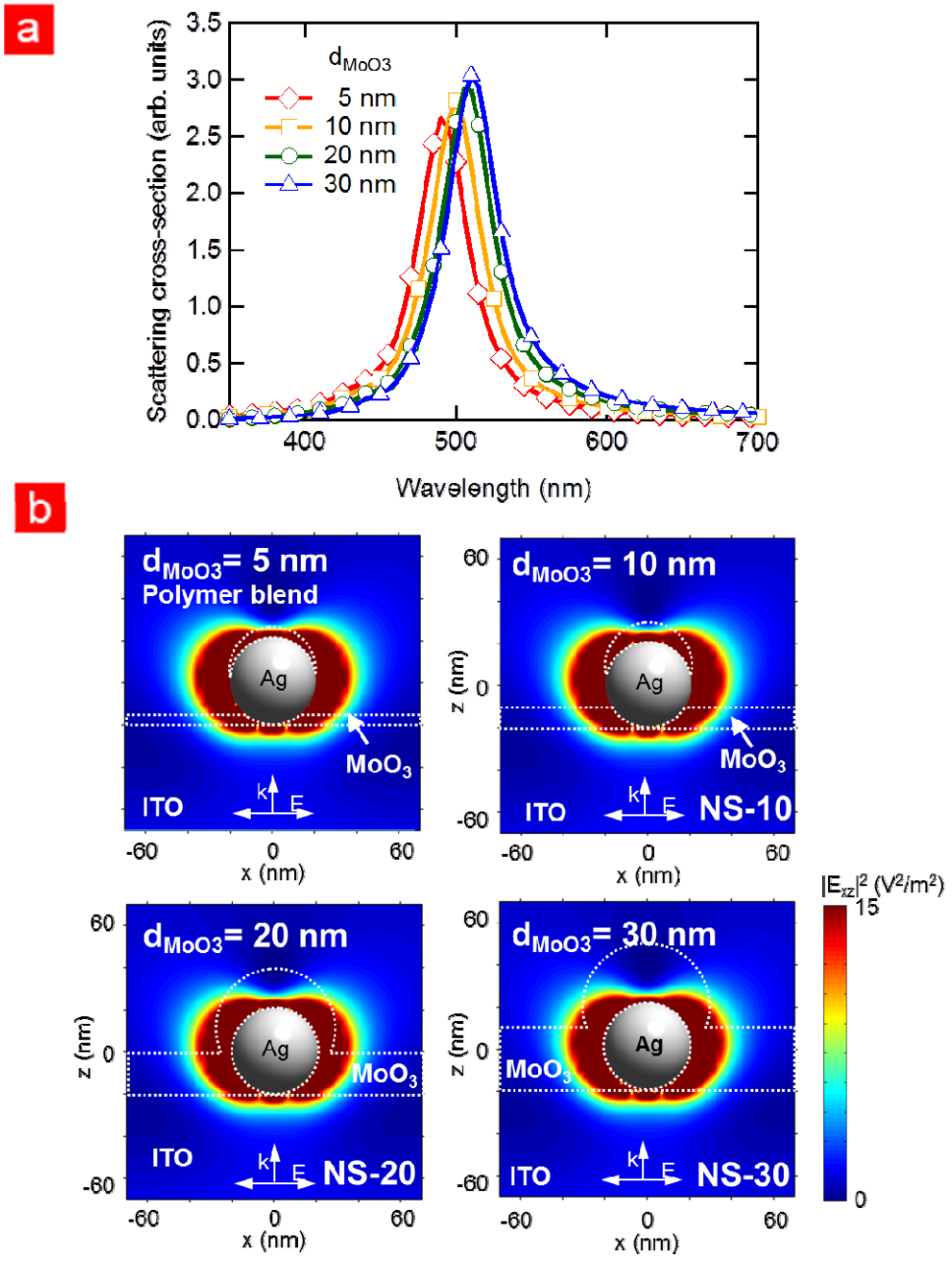

Figure 4.5 Simulated (a) scattering cross-section and (b) electrical field distribution of NBA structure with different d_{MoO3}

4.4 Exciton dynamics in Organic Semiconducting Film with NBA Including Partially and Fully Encapsulated NPs

In previous chapter, the effect of NBA on exciton generation was studied by UV-vis spectrum spectroscopy. This chapter is focused on how increased exciton generation dissociates to the free carriers. According to the Onsager-Braun model, the exciton dissociation only happens in the interface of donor and acceptor molecule as a result of the different HOMO-LUMO energy level [90]. Thus, long diffusion length of exciton is more beneficial to channel the generated exciton to the free carriers. In this chapter, we derived the exciton diffusion length by measuring the lifetime of exciton in the device with NBA. Normally, the diffusion length of exciton in organic semiconducting film is determined by the decay of exciton and diffusion coefficient. Since, the material was fixed among samples, which means the diffusion coefficient lays the similar value, so that exciton lifetime reflects the rate of exciton dissociation inside device.

Figure 4.6 (a) shows the transient PL of PCDTBT film (~40 nm) with NBA including different d_{MoO3}. Here, the PL was obtained at the 690 nm wavelength light, while the films were excited by 405 nm pulse laser. Employing multiple exponential equation, as denoted in Equation 3.1, the exciton decay occurred in the film for each cases were investigated. Exacted lifetimes of film with NBA containing fully encapsulated NP (when d_{MoO3} is 20 and 30 nm) are similar with that of film without NPs (~520 ps). In contrast, lifetimes for the case with partially covered NPs are 378

and 448ps in the case of 5 and 10 nm $d_{MoO3,}$ respectively. Intriguingly, these values are much shorter than that of film without NPs. As the polymer layer was fixed among samples, the faster exciton decay of polymer might be originated form the exciton annihilation inside film with partially encapsulated NPs. In contrast, the insertion of fully covered NPs is not a critical factor to determine the exciton lifetime. Therefore, the transient PL of film clearly shows that the exciton quenching induced by partially covered NPs is one of the sources for decreased device performance by suppressing the transfer of increased exciton generation to the free carriers.

Owing to the difference of exciton decay, the steady state PL of film incorporating partially encapsulated NPs is lower than those of the others, as shown in Figure 4. 6 (b). The steady state PL intensities of film, whose peak is around 690 nm, is broadly improved in the case of d_{MoO3} 20 and 30 nm d_{MoO3}. Meanwhile, those of polymer casted on NBA encapsulated by 5 and 10 nm d_{MoO3} are lower than the case without NBA. The intensity of PL is typically determined by two factors: the exciton lifetime and the plasmonic resonance induced by NPs. As denoted in the Chapter 4.3, partially and fully encapsulated NPs in NBA increase light absorption of film, so that the number of exciton excited in polymer also increased in the film with partially covered NPs. However, the steady state PL of these cases decreases, which reveals the reduced exciton lifetime in the polymer with partially covered NPs. On the other hand, suppressed non- radiative energy transfer in the polymer employing fully covered NP is the origin of higher steady state PL. Thus, the steady state PL also clearly describes that the partially covered NPs works as exciton quenching sites, while the excitons are effectively dissociated into free carriers with small losses in the polymer including fully encapsulated NPs.

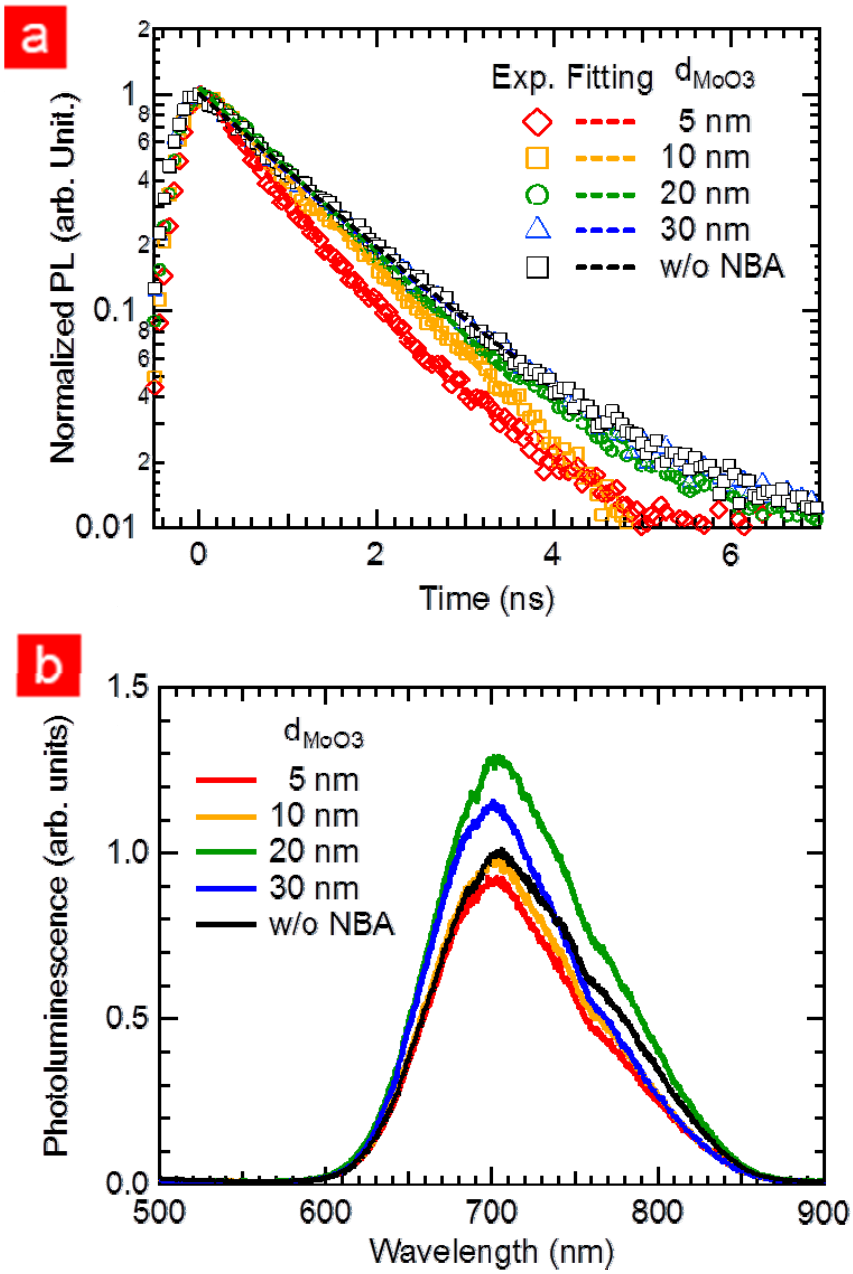

Figure 4.6 (a)Transient and (b)steady state PL of films with and without NBA. Here the polymer film was excited by 405 nm laser

4.5 Carrier dynamics in Organic Solar Cells with NBA Including Partially and Fully Covered NPs

Next, it is explored how the generated carriers extract to the electrode depending on the encapsulation status. First, the losses from the leakage and ohmic contact, the devices were analyzed based on the equivalent circuit model, describe the device introducing shunt (R_{SH}) and series (R_S) resistances [51], as described chapter 2.2.2. Figure.4.7showsthe R_S and R_{SH} of OSCs as a function of d_{MoO3}.The ohmic losses of OSC without NBA, reflected by R_S, increases as the d_{MoO3} increases. It means that the prolonged carrier extraction path from thick flat MoO_3increased losses in OSCs without NBA, thereby resulting in low FF of the OSC. This result is consistent with previous study with P3HT:PC_{60}BM [85]. Thus, the degraded PCE of OSCs without NBA including 30nm d_{MoO3} can be explained by the increased ohmic losses during carrier transport process.

Meanwhile, the R_S of OSC with NBA are lower than those of their corresponding samples including the same d_{MoO3}, except the case with 30nm d_{MoO3}. So, it is clear that the insertion of metallic NPs in dielectric layer in OSCs facilitate carrier swept-out to the electrode, which is mainly attributed by the enlarged interface between the active layer and the HEL, the shorten the distance between the anode and the active layer, as well as the fast carrier mobility of metallic NPs compared to that of the other dielectric and polymer material. Here, the R_S of OSC with NBA containing 5 nm d_{MoO3} is higher than those of the others, since the J-V

characteristics of it shows the non-ideal diode properties. Therefore, the oval-shaped NBA enables carriers to be extracted with small ohmic losses.

The R_{SH}s of OSCs with partially encapsulated NPs (5nm d_{MoO3} = 448 Ω and 10nm d_{MoO3}=511 Ω) sharply decreased compared to that of their corresponding OSC (705-756 Ω), as shown in Figure 4.8. This result denotes that partially encapsulated NPs inside OSCs work as leakage paths, resulting in degraded device performance. On the other hand, R_{SH}s of OSC incorporating NBA with20(665 Ω) and 30 nm (675 Ω) d_{MoO3}, are close to those of device without NPs. Regardless changed distance between the anode and cathode arose from protruded NPs, the leakage properties of device is maintained. It means that carriers in the polymer film with fully covered NPsare effectively moved to the electrode without changing the leakage losses. Figure 4.8 shows the J-V characteristics of device under dark condition, which reflects leakage current of devices. The current density at reverse bias (-1V) of OSC-NBA with 5 nm d_{MoO3} is two order magnitude higher than that of OSC without NBA. Additionally, the current density of OSC-NBA at the reverse bias is inversely proportional to the d_{MoO3}. On the other hand, the current density of OSC-NBA with 20 and 30 nm d_{MoO3} is similar with the OSC without NBA, which denotes that photo generated carriers effectively move to electrode with small losses from the leakage. As a result, the FF of OSC-NBA with 20 (0.60) and 30 (0.61) nm d_{MoO3} is much higher than those of OSC-NBA with 5 (0.50) and 10 90.58) nm d_{MoO3}. Consequently, fully covered NPs in NBA lead to the enhancement in carrier extraction without increasing leakage, whereas the enhanced exciton generation induced by partially covered NPs does not channeled into photocurrent owing to leakage losses.

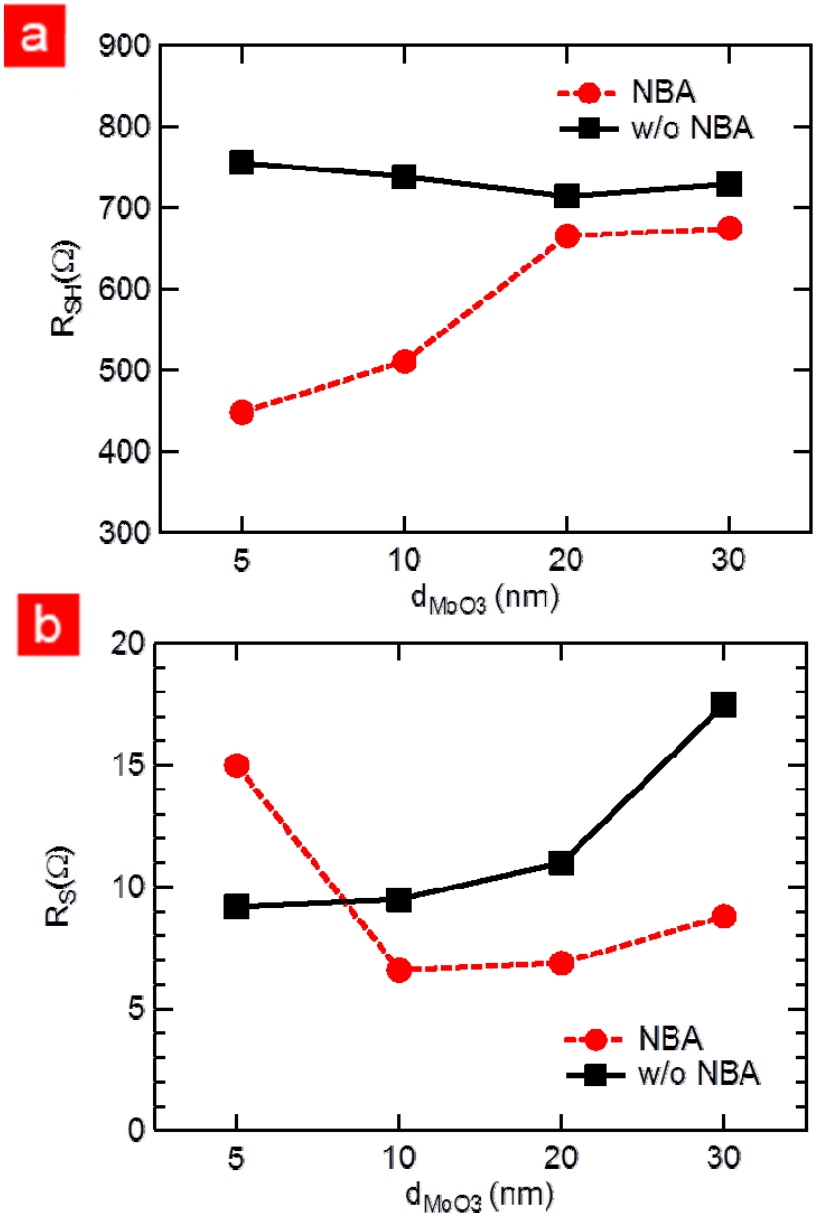

Figure 4.7 (a) Shunt and (b) series resistance of OSC with and without NBA as a function of d_{MoO3}.

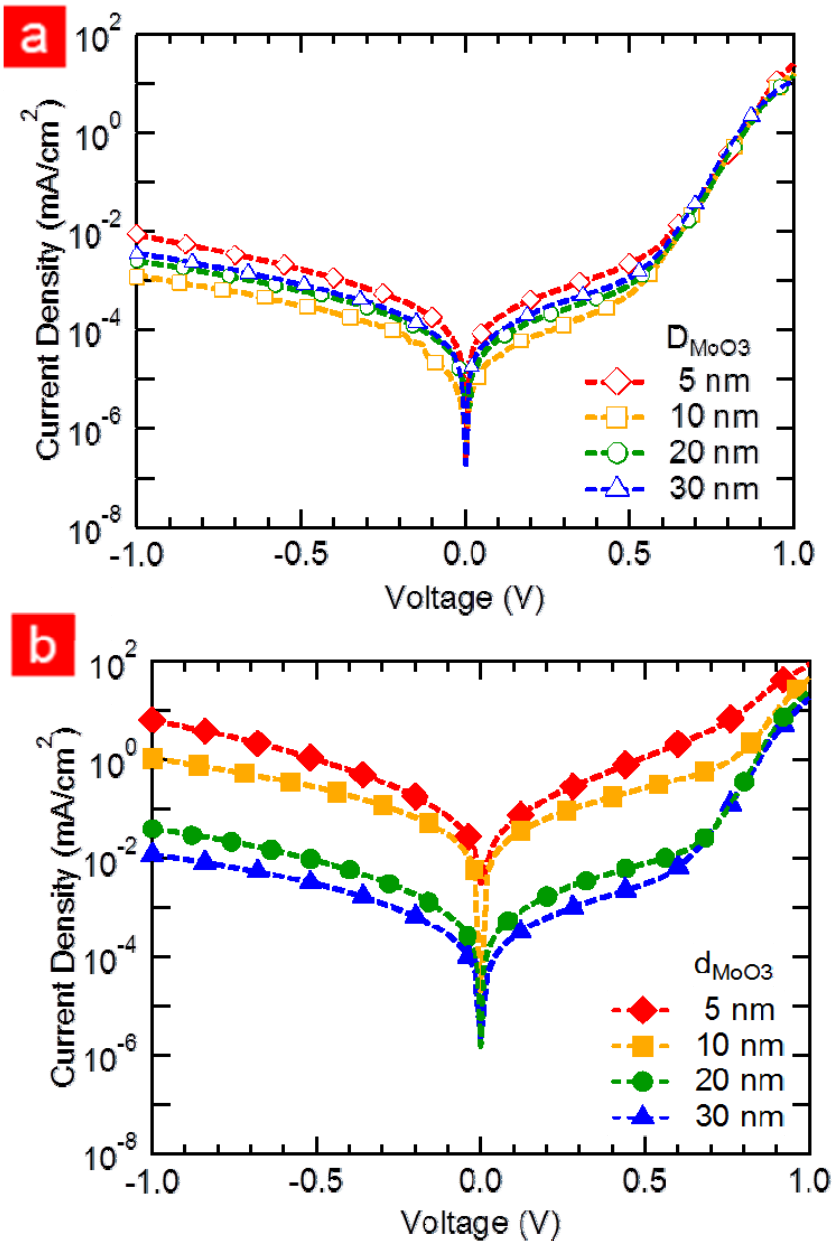

Figure 4.8 (a) The J-V characteristics of OSCs (a) with and (b) without NBA containing different d_{MoO3}.

Second, the carrier recombination in OSC-NBA was investigated by the impedance spectroscopy. Figure4.9 shows the capacitance versus voltage (C-V) characteristics of OSC-NBA at 100 KHz under dark condition. Despite a fixed thickness of active layer among samples, the capacitance of OSC-NBA with 5 and 10 nm $d_{MoO3}$is lower than that of OSC-NBA with fully covered NPs. To derive the carrier density (N_D) inside OSC-NBA, the C-V data was analyzed by the Mott-Schottky model, calculating N_D using the slope of C^2-V ,as denoted in equation 2.17[37, 38, 91, 92]. The ND of OSC-NBA with 10nm d_{MoO3} ($9.8 \times 10^{16} cm^{-3}$) is lower than those of OSC-NBA including 20 ($5.1 \times 10^{17} cm^{-3}$) and 30 nm ($3.8 \times 10^{17} cm^{-3}$) d_{MoO3}. This value lies similar range of previous report using PCDTBT:BC_{70}BM OSC. [54]. However, the N_D of OSC-NBA employing 5 nm d_{MoO3} is not elucidated by this model, due to its non-ideal diode properties. Since this measurement was conducted in dark, so that the photo-generation of carrier is negligible in this case. Moreover, the buffer layer between electrode and active layer was fixed among the samples. Therefore, the recombination losses in OSC-NBA incorporating partially covered NPs leads to the reduction of N_D.

To establish how these recombination losses affect device performance under illumination, the light intensity (P_{Light}) dependence of V_{OC} for OSC-NBA was conducted, as shown in Figure 4.9 (b). According to the equation 2.15, Langevin recombination loss, direct recombination between hole and electron carrier loss, is dominant when a slope of P_{Light}-V_{OC} (s) is near thermal energy (K_BT/q), where K_B is Boltzmann constant, T is absolute temperature, and q is a charge of single electron. Meanwhile, the steeper slope indicates the device performance is governed by trap-assisted (Shockley-Read-Hall) recombination, where the carrier recombines to its counter electrode capture in trap energy level. At room temperature (300K), the s of OSC-NBA with 10 nm d_{MoO3} (1.79) is much steeper than that of device with 20

(1.02) and 30 nm (1.02) d_{MoO3}.It means that the photo-generated carriers in OCS-NBA containing partially covered NPs, annihilated owing to the recombination with their counter carriers captured in traps. In contrast, the carriers effectively transport to counter electrodes with small losses in the OSC-NBA employing fully enclosed NPs. Therefore, it is apparent that partially covered NPs works as trap sites in plasmonic OSCs, resulting in degraded device performance.

Moreover, in the case of OSC-NBA with 10 nm d_{MoO3}, the decreased slope of device at high temperature (333K) (s =1.64) is observed in comparison with the value measured at room temperature. This is another supportive evidence to reveal the role of partially covered NPs in OSC, because the possibility of releasing carriers captured in traps increases at this temperature due to raised thermal energy. In contrast, the slopes of OSC-NBA with 20 and 30nm d_{MoO3} are unchanged regardless the change of given thermal energy. Such trap assisted recombination losses prevent carriers from effectively transporting to electrodes in devices, so that the lower device performance of OSC-NBA with partially covered NPs is exhibited. Therefore, our optical and electrical analyses reveal that the NBA fully covering NPs in OSCs enhance carrier extraction without changing losses, while the increased carrier annihilation by trap-assisted leakage losses in partially covered NPs deteriorates the device performance.

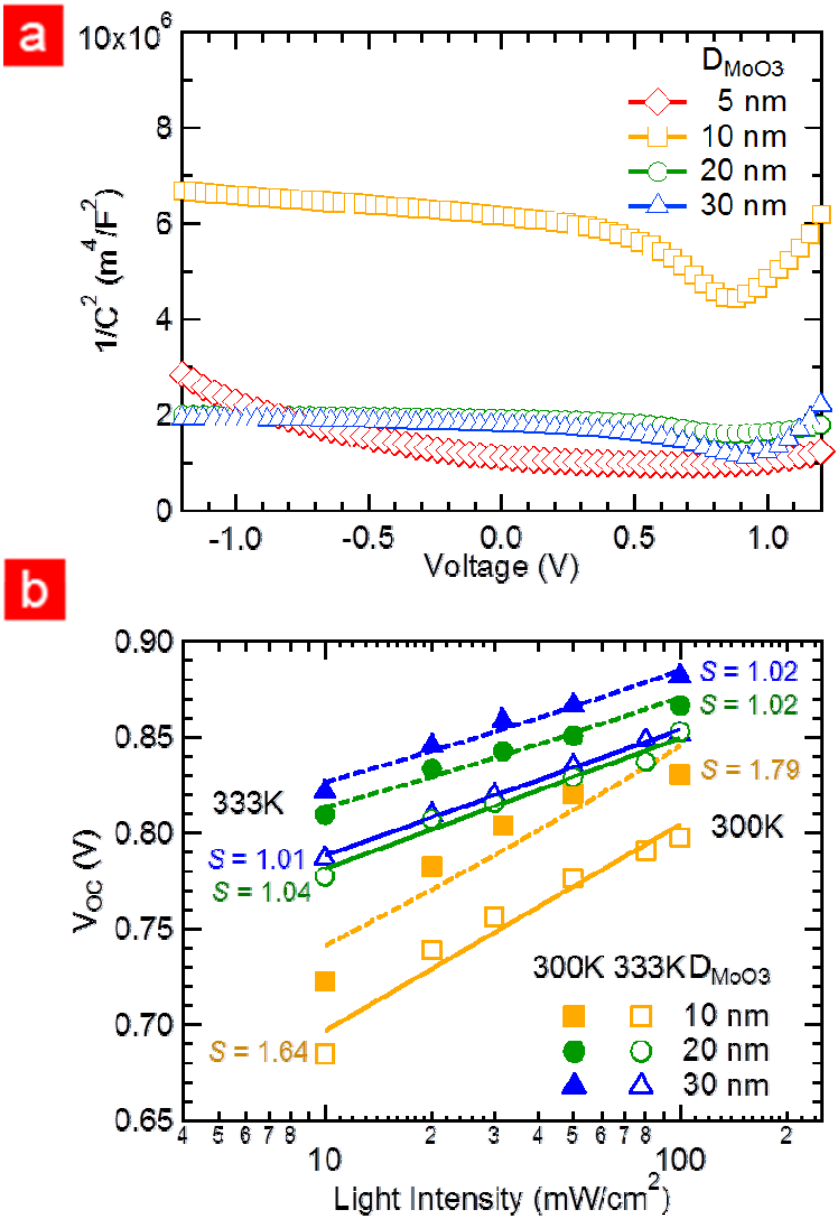

Figure 4.9 (a) C-V characteristics of OSC-NBA under dark condition (b) V_{OC} of OSC-NBA employing different d_{MoO3}as a function of light intensity

4.6 Summary

In this chapter, the role of partially and fully covered NPs in plasmonic OSC is investigated The TEM and SEM data reveal that the encapsulation status of NP can be successfully tailored by managing the overlapped MoO_3 layer thickness. The PCE of OSC-NBA with 20 and 30 d_{MoO3} is improved and the best performance is achieved at d_{MoO3} of 20 nm, whereas the devices with partially uncovered Ag NP by a thin d_{MoO3} of 5 to 10 nm show lower efficiency compared to the OSC without NBA including the same d_{MoO3}. In the respect of absorption, partially covered NPs is much more beneficial to light harvest due to the short propagation length of plasmonic effect. However, the degraded performance of device including NBA with the partially disclosed NPs is caused by the short lifetime of exciton, the trap-assisted recombination, and leakage loss. As a result, this systematic analysis of the NBA on plasmonic OSCs allows one to optimize the device performance through both the optical and electrical enhancements.

Chapter 5

Conclusion

In this thesis, the effect of NBA on the performance of plasmonic OSC has been systematically studied. The NBA is consisted of the Ag NPs and thermally evaporated MoO_3. Here, the size and distribution of aerosol derived NPs is precisely controlled with small chance of aggregation. And the thermally evaporated MoO3 follows underlying structure, so the NBA is oval-shaped one.

The plasmonic OSC with NBA shows the higher efficiency compared to the device without NBA in various kinds of polymer: P3HT:PC_{60}BM (2.7 ➔ 2.9%) and PCDTBT:PC_{70}BM (5.2 ➔ 6.1%). This is mainly attributed the enhancement in the photocurrent without changing other photovoltaic factors. Particularly, the enhanced spectral response at the wavelength around 500 nm is predominant in the device with NBA. The optical simulation shows that the scattering, the localized surface plasmon, as well as the multiple reflection between NPs and reflective electrode leads to the increased light absorption in the film. Moreover, the protruded structure of hole extraction layer provides effective carrier transport to the electrode. Therefore, the insertion of NBA allows us to improve device performance in the electrical and optical points.

Compared the plasmonic effect from the widely using plasmonic structure (10%), Metallic NPs mixed in the solution buffer layer, the enhancement induced by NBA (17%) is higher. Since, NPs are surrounded by high refractive index material (~2.0) in the NBA, the plasmonic effect from NBA penetrate into active layer effectively, while the optical effect from conventional effect is confined in to the low refractive index of solution buffer (~1.8) , PEDOT:PSS. Moreover, the exciton lifetime in the film with NBA is similar with that of film without NBA, whereas the faster decay of exciton in the film with conventional structure is observed. Consequently, the NBA provides better optical and electrical properties, resulting in high efficient devices.

Meanwhile, the enhanced photo-current induced from plasmonic effect of NBA is proportion to the size of NPs. The simulation results show that this is attributed increased scattering ration compared to the absorption form NPs. Additionally the maximum enhanced wavelength can be tuned by controlling the size of NPs. However, the increased leakage current is observed in the OSC-NBA with 60 nm NPs owing to the limitation of active layer's thickness (~100 nm). Regarding all this factors, maximum PCE is achieved at the OCS-NBA with 40 nm NPs, which is 17% higher than that of OSC without NPs.

Next, the effect of encapsulation layer in NBA is investigated in the optical and electrical point. By changing the thickness of MoO3 in NBA from 5 to 30 nm, the encapsulation ratio of NPs is varied from 100 to 40 %. Especially in the case of NBA with 40 nm NPs, NPs with thicker than 20 nm MoO_3 are fully covered, whereas NPs with thinner than 10 nm MoO_3 are partially isolated from polymer layer. In the optical point of view, the polymer with partially covered NPs absorbs more light compared to the film with fully covered one because of short penetration depth of plasmonic effect. On the other hand, the transient PL of film with NBA

shows that partially covered NPs work as exction quenching sites. Moreover, partially covered NPs are considered as trap-assisted recombination center, thereby resulting in reduced device performance. Therefore, the plasmonic effect induced by partially covered NPs are negated by negative electric effect from them, while the plasmonic effect arose from fully covered NPs is channeled into increased photo-current without deteriorating device performance.

In conclusion, this work suggests a novel approach, NBA, to increase light absorption and carrier extraction in the plasmonic organic solar cells. Furthermore, the role of NPs depending on their passivation status is systematically studied for finding out the way to maximize device performance. This novel plasmonic structure could apply to the variety of types of opto-electronic devices, such as thin film solar cells, light-emitting diodes and transistors.

Bibilography

[1] A. Watson, S. Lefevre, M. I. McCormick, P. Domenici, G. E. Nilsson and P. L. Munday, " Marine mollusc predator-escape behaviour altered by near-future carbon dioxide levels" Proc. R. Soc. B **281**, 1774 (2014)

[2] C. Mora, "The projected timing of climate departure from recent variability" *Nature*, **502,** 183 (2013)

[3] N. S. Lewis, "Toward Cost-Effective Solar Energy Use," *Science*, **315**, 798 (2007)

[4] C. N. Hoth, P. Schilinsky, S. A. Choulis and C. J. Brabec, "Printing Highly Efficient Organic Solar Cells", *Nano Lett*, **8**, 2806 (2008)

[5] S. E. Shaheen, R. Radspinner, N. Peyghambarian and G. E. Jabbour "Fabrication of bulk heterojunction plastic solar cells by screen printing", *Appl. Phys. Lett*, 79, 2996 (2001)

[6] C. J. Brabec, N. S. Sariciftci and J. C. Hummelen "Plastic Solar Cells", *Adv. Funct. Mater*, **11**, 15 (2001)

[7] C. W. Tang, "Two-layer organic photovoltaic cell" *Appl. Phys. Lett.***48**, 183 (1986)

[8] J. You, L. Dou, K. Yoshimura, T. Kato, K. Ohya, T. Moriarty, K. Emery, C.-C. Chen, J. Gao, G. Li and Y. Yang, "A polymer tandem solar cell with 10.6% power conversion efficiency", *Nat. Commun*, **4**, 1, (2013)

[9] C. -C. Chen, W.-H. Chang, K. Yoshimura, K. Ohya, J. You, J. Gao, Z. Hong, and Y. Yang, "An efficient triple-Junction polymer solar cell having a power conversion efficiency exceeding 11%", *Adv. Mater*, **26**, 5670 (2014)

[10] N. Espinosaa, , R. García-Valverdea, A. Urbinab, F. C. Krebs, "A life cycle analysis of polymer solar cell modules prepared using roll-to-roll methods under ambient conditions", *Sol. Energy Mater. Sol. Cells*. **95**, 1293 (2011)

[11] Q. Gan, F. J. Bartoli, and Z. H. Kafafi, "Plasmonic-Enhanced Organic Photovoltaics: Breaking the 10% Efficiency Barrier", *Adv. Mater*. **25**, 2385 (2013)

[12] S. Baroni and R. Resta, "Ab initio calculation of the macroscopic dielectric constant in silicon", *Phys. Rev. B*,**33,** 7017 (1986)

[13] P. E. Shaw , A. Ruseckas, I. D. W. Samuel, "Exciton diffusion measurements in Poly(3-hexylthiophene)", *Adv. Mater*.**20**,3516. (2008)

[14] M. A. Baldo, D. F. O'Brien, Y. You, A. Shoustikov, S. Sibley, M. E. Thompson, S. R. Forrest, *Nature* "Highly efficient phosphorescent emission from organic electroluminescent devices", **395**, 151 (1998)

[15] P. Peumans and S. R. Forrest, "Separation of geminate charge-pairs at donor–acceptor interfaces in disordered solids" *Chem. Phys. Lett*.**398**, 27 (2004)

[16] H. Bässler, "Charge transport in disordered organic photoconductors a Monte Carlo simulation study" *Phys. Status Solidi B***175**, 15 (1993)

[17] K. S. Nalwa, J. -M. Park , K.-M. Ho, and S. Chaudhary, "On realizing higher efficiency polymer solar cells using a textured substrate platform", *Adv. Mater*.**23**, 112 (2011)

[18] D. Myers, W. Cao, V. Cassidy, S.-H. Eom, R. Zhou, L. Yang,. W. You and J. Xue "A universal optical approach to enhancing efficiency of organic-based photovoltaic devices"*Energy Environ. Sci.*, **5**, 6900 (2012)

[19] H. A. Atwater and A. Poleman, "Plasmonics for improved photovoltaic devices", *Nature Mater.***8**, 205 (2010)

[20] A. J. Morfa , K. L. Rowlen , T. H. Reilly , III , M. J. Romero , Jao van de Lagemaat, "Plasmon-enhanced solar energy conversion in organic bulk heterojunction photovoltaics", *Appl. Phys. Lett.***92** , 013504 (2008)

[21] S.-S. Kim , S.-I. Na , J. Jo and D.-Y. Kim , Y.-C. Nah, "Plasmon enhanced performance of organic solar cells using electrodeposited Ag nanoparticles",*Appl. Phys. Lett.***93**, 073307 (2008)

[22] J. H. Lee , J. H. Park , J. S. Kim , D. Y. Lee and K. Cho, "High efficiency polymer solar cells with wet deposited plasmonic gold nanodots",*Org. Electron*. **10**, 416 (2009)

[23] W. J. Yoon , K. Y. Jung , J. Liu , T. Duraisamy , R. Revur , F. L. Teixeira ,S. Sengupta and P. R. Berger, "Enhanced organic light emitting diode and solar cell performances using silver nano-clusters", *Solar Energy Mater. Solar Cells*, **94**,128 (2012)

[24] F. C. Chen , J. L. Wu , C. L. Lee , Y. Hong , C. H. Kuo and M. H. Huang, "Plasmonic-enhanced polymer photovoltaic devices incorporating solution-processable metal nanoparticles", *Appl. Phys. Lett.***95**, 013305, (2009).

[25] J. Yang, J. You, C.-C. Chen, W.-C. Hsu, H.-R. Tan, X. W. Zhang, Z. Hong and Y. Yang, "Plasmonic Polymer Tandem Solar Cell", *ACS Nano*,**5,** 6210(2011)

[26] R. S. Kim, J. Zhu, J. H. Park, L. Li, Z. Yu, H. Shen, M. Xue, K. L. Wang, G. Park, T. J. Anderson, and Q. Pei, "E-beam deposited Ag-nanoparticles plasmonic

organic solar cell and its absorption enhancement analysis using FDTD-based cylindrical nano-particle optical model", *Opt. Express*, **20**, 12649 (2012).

[27] X. Wang, J. W. Ho, Q. Yang, H. L. Tamb, G. X. Li, K. W. Cheah and F. Zhu, "Performance enhancement in organic photovoltaic devices using plasma-polymerized fluorocarbon-modified Ag nanoparticles", *Org. Electron*. **12,** 1943 (2011)

[28] D. Zhang, W. C. H. Choy, F. Xie, W. E. I. Sha, X. Li, B. Ding, K. Zhang, F. Huang, and Y. Cao, "Plasmonic Electrically Functionalized TiO2 for High-Performance Organic Solar Cells", *Adv. Funct. Mater.***23**, 4255 (2013)

[29] M. Heo, H. Cho, J.-W. Jung, J.-R. Jeong, S. Park, and J. Y. Kim "High-performance organic optoelectronic devices enhanced by surface plasmon resonance" *Adv. Mater.***23**: 5689 (2011)

[30] Lu, L.; Luo, Z.; Xu, T.; Yu, L. Cooperative Plasmonic Effect of Ag and Au Nanoparticles on enhancing performance of polymer solar cells. *Nano Lett.***13**, 59 (2013)

[31] D. H. Wang, D. Y. Kim, K. W. Choi, J. H. Seo, S. H. Im, J. H. Park, O O. Park and A. J Heeger "Enhancement of donor–acceptor polymer bulk heterojunction solar cell power conversion efficiencies by addition of Au nanoparticles" *Angew. Chem. Int. Ed* **123**, 5633 (2011)

[32] D. H. Wang, K. H. Park, J. H. Seo, J. Seifter, J. H. Jeon, J. H. Park, O O. Park and A. J. Heeger, "Enhanced power conversion efficiency in PCDTBT/PC_{70}BM bulk heterojunction photovoltaic devices with embedded silver nanoparticle clusters", *Adv. Energy Mater.***1**, 766 (2011)

[33] C.-H. Kim, S.-H. Cha, S. C. Kim, M. Song, J. Lee, W. S. Shin, S.-J. Moon, J. H. Bahng, N. A. Kotov and S.-H. Jin, "Silver nanowire embedded in P3HT:PCBM for high-efficiency hybrid photovoltaic device applications", *ACS Nano*, **5**, 3319 (2011)

[34] D. H.Wang, J. K. Kim, K. H. Park, O O. Park and J. H. Park “Enhanced light harvesting in bulk heterojunction photovoltaic devices with shape-controlled Ag nanomaterials: Ag nanoparticles versus Ag nanoplates”, *RSC Advances*, **2**, 7268 (2012)

[35] V. Jankovic, Y. Yang, J. You, L. Dou, Y. Liu, P. Cheung, J. P. Chang, and Y. Yang “Active layer-incorporated, spectrally tuned Au/SiO2 core/shell nanorod-based light trapping for organic photovoltaics” *ACS Nano,***7**, 3815 (2013)

[36] F.-X. Xie, W. C. H. Choy, C. C. D. Wang, W. E. I. Sha and D. D. S. Fung, “Improving the efficiency of polymer solar cells by incorporating gold nanoparticles into all polymer layers”, *Appl. Phys. Lett.* **99**, 153304 (2011)

[37] H. Choi, J.-P. Lee, S.-J. Ko, J.-W. Jung, H. Park, S. Yoo, O. Park, J.-R. Jeong, S. Park, and J. Y. Kim “Multipositional slica-cated slver nanoparticles for high-performance polymer solar cells”, *Nano Lett.***13**, 2204 (2013)

[38] C. Min , J. Li , G. Veronis , J. Y. Lee , S. Fan and P. Peumans , “Enhancement of optical absorption in thin-film organic solar cells through the excitation of plasmonic modes in metallic gratings” *Appl. Phys. Lett.***96**, 133302 (2010)

[39] J. You , X. Li , F. Xie , W. E. I. Sha , J. H. W. Kwong , G. Li ,W. C. H. Choy and Y. Yang , “Surface Plasmon and Scattering-Enhanced Low-Bandgap Polymer Solar Cell by a Metal Grating Back Electrode”, *Adv. Energy Mater.***2** , 1203 (2012)

[40] D. H. Wang , J. Seifter , J. H. Park , D.-G. Choi , and A. J. Heeger “Efficiency Increase in Flexible Bulk Heterojunction Solar Cells with a Nano-Patterned Indium Zinc Oxide Anode”, *Adv. Energy Mater*. **2**, 1319 (2012)

[41] S. Kim, C.-H. Kim, S. K. Lee, J.-H. Jeong, J. Lee, S.-H. Jin, W. S. Shin, C. E. Song, J.-H. Choi and J.-R. Jeong, “Highly efficient uniform ZnO nanostructures for an electron transport layer of inverted organic solar cells”, *Chem. Commun.***49**, 6033 (2013)

[42] W. Luhman , S. Lee , T. Johnson , R. Holmes and S. Oh, “Self-assembled plasmonic electrodes for high-performance organic photovoltaic cells” *Appl. Phys. Lett.***99**, 103306 (2011)

[43] B. Wu , T. Oo , X. Li , X. Liu , X. Wu , E. Yeow , H. Fan , N. Mathews and T. Sum, “Efficiency enhancement in bulk-heterojunction solar cells integrated with large-area Ag nanotriangle arrays”, *J. Phys. Chem. C*, **116**, 14820 (2012)

[44] X. Li, W. C. H. Choy, L. Huo, F. Xie, W. E. I. Sha, B. Ding, X. Guo, Y. Li, J. Hou, J. You andY. Yang, “Dual plasmonic nanostructures for high performance inverted organic solar cells”, *Adv. Mater.***22**, 3046 (2012)

[45] R. Josep; J. Molera; P. Sciau; E. Pantos and M. Vendrell-Saz, “Copper and silver nanocrystals in lustre lead glazes: development and optical properties". J. Euro. Ceramic Soc. **26**, 3813 (2006)

[46] G. Mie, “Beiträge zur Optik trüber Medien, speziell kolloidaler Metallösungen”, *Annalen der Physik*, **330**, 377 (1908)

[47] D. Duchea, P. Torchioa, L. Escoubasa, F. Monestiera, J.-J. Simona, F. Floryb, G. Mathian, “Improving light absorption in organic solar cells by plasmonic contribution”, *Sol. Mater. Sol. Ener. Cells*, **93**, 1377 (2009)

[48] K. L. Kelly, E. Coronado, L. L. Zhao, G.C. Schatz,”The Optical Properties of Metal Nanoparticles: The Influence of Size, Shape, and Dielectric Environment” *J. Phys. Chem. B***107**, 668 (2003)

[49] S. Pillai, K. R. Catchpole, T. Trupke and M. A. Green, “Surface plasmon enhanced silicon solar cells”, *J. Appl. Phys.***101**, 093105 (2007)

[50] H. Hoppe, and N. S. Sariciftci, “Organic solar cells: An overview”, *J. Mater. Res.***19**, 1924 (2004)

[51]A. Moliton and J.–M. Nunzi, “How to model the behavior of photovoltaics cells”, *Polym. Int.***55**, 583 (2006)

[52] L. J. A. Koster, V. D. Mihailetchi, R. Ramaker and P. W. M. Blom, “Light-intensity dependence of open-circuit voltage of polyemer:fullerene solar cells”, *Appl. Phys. Lett.***86**, 123509 (2005)

[53] B. G. Streetman and S. Benerjee, “Solid state electronic devices”, 5th edition, Princeton hall, New York, 2000

[54] Y. Zhang, H. Zhou, J. Seifter, L. Ying, A. Mikhailovsky, A. J. Heeger, G. C. Bazan andT.-Q. Nguyen, “Molecular Doping Enhances Photoconductivity in Polymer Bulk Heterojunction Solar Cells”, *Adv. Mater,* **25**, 7038 (2013).

[55] J. Y. Kim, K. Lee, N. E. Coates, D. Moses, T.-Q. Nguyen, M. Dante and A. J. Heeger“Efficient Tandem Polymer Solar Cells Fabricated by All-Solution Processing”, *Science,***317,** 222 (2007)

[56] B. K. Juluri, J. Huang; L. Jensen (2014), "Extinction, Scattering and Absorption efficiencies of single and multilayer nanoparticles," https://nanohub.org/resources/nmie. (DOI: 10.4231/D37W6765J)

[57] X. Yang, C.-C. Chueh, C.-Z. Li, H.-L. Yip, P. Yin, H. Chen, W.-C. Chen, A. K.-Y. Jen, “High-Efficiency Polymer Solar Cells Achieved by Doping Plasmonic Metallic Nanoparticles into Dual Charge Selecting Interfacial Layers to Enhance Light Trapping” *Adv. Energy Mater.* **3**, 666 (2013)

[58] D. Spyropoulos, M. M. Stylianakis, E. Stratakis, E. Kymakis, “Organic Bulk Heterojunction Photovoltaic Devices with Surfactant-free Au Nanoparticles Embedded in the Active Layer.” *Appl. Phys. Lett.***100**, 213904 (2012)

[59] M. Xue, L. Li, B. J. Tremolet de Villers, H. Shen, J. Zhu, Z. Yu, A. Z. Stieg, Q. Pei, B. J. Schwartz, K. L. Wang, “Charge-carrier Dynamics in Hybrid Plasmonic Organic Solar Cells with Ag Nanoparticles.” *Appl. Phys. Lett.***98**, 253302. (2012)

[60] N. Kalfagiannis, P. G. Karagiannidis, C. Pitsalidis, N. T. Panagiotopoulos, C. Gravalidis, S. Kassavetis, P. Patsalas, S. Logothetidis, "Plasmonic Silver Nanoparticles for Improved Organic Solar Cells." *Sol. Energy Mater. Sol. cells***104**, 165 (2012)

[61] J. -L. Wu, F.-C. Chen, Y.-S. Hsiao, F.-C. Chien, P. Chen, C.-H. Kuo, M. H. Huang, C.-S. Hsu, "Surface Plasmonic Effects of Metallic Nanoparticles on the Performance of Polymer Bulk Heterojunction Solar Cells." *ACS Nano***5**, 959 (2011)

[62] Y. Sun, C. J. Takacs, S. R. Cowan, J. H. Seo, X. Gong, A. Roy, A. J. Heeger, "Efficient, Air-Stable Bulk Heterojunction Polymer Solar Cells Using MoOx as the Anode Interfacial Layer" *Adv. Mater.***23**, 2226 (2011)

[63] P.-P.Cheng, G.-F. Ma, J. Li, Y. Xiao, Z.-Q. Xu, G.-Q. Fan, Y. -Q. Li, S. -T. Lee, J. -X. Tang, "Plasmonic Backscattering Enhancement for Inverted Polymer Solar Cells" *J. Mater. Chem.***22**, 22781 (2012)

[64] P.-P.Cheng, L. Zhoi, J.-A Li, Y. Q. Li , S. -T. Lee, J. -X. Tang, "Light Trapping Enhancement of Inverted Polymer Solar Cells with a Nanostructured Scattering Rear Electrode." *Org. Electron.***14**, 2158 (2013)

[65] Z. Su, L. Wang , Y. Li , G. Zhang , H. Zhao , H. Yang , Y. Ma , B. Chu, and W. Li, Surface Plasmon Enhanced Organic Solar Cells with a MoO_3 Buffer Layer", *ACS Appl. Mater. Interfaces*, **5**, 12847 (2013)

[66] H. G. Scheibel and J. Porstendörfer, "Generation of Monodisperse Ag- and NaCl-Aerosols with Particle Diameters between 2 and 300 nm" *J. Aerosol Sci.***14**, 113 (1983).

[67] M. H. Magnusson,; K. Deppert, J. -O. Malm, J. -O. Bovin and L. Samuelson, "Gold Nanoparticles: Production, Reshaping, and Thermal Charging", *J. Nanopart. Res.***1**, 243 (1999)

[69] J. H. Jung, H. C. Oh, H. S. Noh, J. H. Ji and S. S. Kim, "Metal Nanoparticle Generation Using a Small Ceramic Heater with a Local Heating Area"*J. Aerosol Sci.***37**, 1662 (2006)

[70] H. Kim, J. Kim, H. Yang, J. Suh, T. Kim, B. Han, S. Kim, D. S. Kim, P. V. Pikhitsa and M. Cho, "Parallel patterning of nanoparticles via electrodynamic focusing of charged aerosols", Nature Nanotechnology **1**, 117 (2006)

[71] K.-M. Lee, D.-J. Lee and H. Ahn, "XRD and TEM studies on tin oxide (II) nanoparticles prepared by inert gas condensation", *Mater. Lett*, **58**, 3122 (2004)

[72] K. Jung, H.-J. Song, G. Lee, Y. Ko, K. Ahn , H. Choi, J. Y. Kim, K. Ha, J. Song, J.-K. Lee, C. Lee, and M. Choi, "Plasmonic Organic Solar Cells Employing Nanobump Assembly via Aerosol-Derived Nanoparticles", ACS Nano **8**, 2590 (2014)

[73] T. Jägeler-Hoheisel, F. Selzer , M. Riede , and K. Leo, "Direct Electrical Evidence of Plasmonic Near-Field Enhancement in Small Molecule Organic Solar Cells", *J. Phys. Chem. C*, **118**, 15128 (2014)

[74] S.-W. Baek, J. Noh, C.-H. Lee, B. S. Kim, M.-K. Seo, and J.-Y. Lee, "Plasmonic Forward Scattering Effect in Organic Solar Cells:A Powerful Optical Engineering Method", *Sci. Reports*, **3**, 1726 (2013)

[75] Y. Liang and L. Yu, "A New Class of Semiconducting Polymers for Bulk Heterojunction Solar Cells with Exceptionally High Performance", *Acc. Chem. Res*. **43**, 1227 (2010)

[76] L. J. A. Koster, V. D. Mihailetchi, H. Xie, and P. W. M. Blom,"Origin of the light intensity dependence of the short-circuit current of polymer/fullerene solar cells"*Appl. Phys. Lett.***87**, 203502 (2005)

[77] P. Schilinsky, C. Waldauf, and C. J. Brabec, “Recombination and loss analysis in polythiophene based bulk heterojunction photodetectors”*Appl. Phys. Lett.***81**, 3885 (2002)

[78] G. Dennler, M. C. Scharber andC. J. Brabec, “Polymer-Fullerene Bulk-Heterojunction Solar Cells” *Adv. Mater.***21**, 1323 (2009)

[79] J. Wang, Y.-J.Lee, A. S. Chadha, J. Yi, M. L. Jespersen, J. J. Kelley, H. M. Nguyen, M. Nimmo, A. V. Malko, R. A. Vaia, W. Zhou, and J. W. P. Hsu, “Effect of Plasmonic Au Nanoparticles on Inverted Organic Solar Cell Performance”*J. Phys. Chem. C*, **117**, 85 (2013)

[80] M. Salvador, B. A. MacLeod, A. Hess, A. P. Kulkarni, K. Munechika, J. I. L. Chen and D. S. Ginger, “Electron Accumulation on Metal Nanoparticles in Plasmon-Enhanced Organic Solar Cells”*ACS Nano*, **6**, 10024 (2012)

[81] X. Li, W. C. H. Choy, F. Xie, S. Zhang andJ. Hou, “Room-temperature Solution-processed Molybdenum Oxide as a Hole Transport Layer with Ag Nanoparticles for Highly Efficient Inverted Organic Solar Cells” *J. Mater. Chem. A***1**, 6614 (2013)

[82] D. Qu, F. Liu, Y. Huang, W. Xie and Q. Xu, “Mechanism of Optical Absorption Enhancement in Thin Film Organic Solar Cells with Plasmonic Metal Nanoparticles” *Opt. Express***19**, 24795 (2011)

[83] B. Wu, X. Wu, C. Guan, K. Fai Tai, E. K. L. Yeow, H. Jin Fan, N. Mathews and T. C. Sum, “Uncovering loss mechanisms in silver nanoparticle-blended plasmonic organic solar cells” *Nat. Commun.*, **4**, 2004 (2013)

[84] A. Barrie and N. E. Christensen, “High-resolution x-ray photoemission spectra of silver”, *Phys. Rev. B*, **14**, 2442 (1976)

[85] S. Noh, C. K. Suman, D. Lee, S. Kim and C. Lee. “Study of buffer layer thickness on bulk heterojunction solar cell”, *J. Nanosci. Nanotechnol,* **10**, 6815, (2010)

[86] J. C Ostrowski, A. Mikhailovsky, D. A Bussian, M. A. Summers, S. K. Buratto and G. C. Bazan, “Enhancement of Phosphorescence by Surface-Plasmon Resonances in Colloidal Metal Nanoparticles: The Role of Aggregates”*Adv. Funct. Mater.***16,** 1221 (2006)

[87] H. Chew, “Transition rates of atoms near spherical surfaces”, *J. Chem. Phys.*87, 1355 (1987)

[88] H. Shen, P. Bienstman, and B. Maes, “Plasmonic absorption enhancement in organic solar cells with thin active layers” *J. Appl. Phys.***106**, 073109 (2009)

[89] X. Xu,1 Q. Du, B. Peng, Q. Xiong, L. Hong, H. V. Demir,T. K. S. Wong, A. K. K. Kyaw, and X. W. Sun “Effect of shell thickness on small-molecule solar cells enhanced by dual plasmonic gold-silica nanorods” *Appl. Phys. Lett.***105**, 113306 (2014)

[90] C. Deibel, T. Strobel, and V. Dyakonovref, “Origin of the Efficient Polaron-Pair Dissociation in Polymer-Fullerene Blends”, *Phys. Rev. Lett.***103**, 036402 (2009)

[91] W. Brütting, H. Riel, T. Beierlein and W. Riess “Influence of trapped and interfacial charges in organic multilayer light-emitting devices” *J. Appl. Phys.***89**, 1704 (2001)

[92] P. P. Boix, G. Garcia-Belmonte, U. Muñecas, M. Neophytou, C. Waldauf and R. Pacios, “Determination of gap defect states in organic bulk heterojunction solar cells from capacitance measurements” *Appl. Phys. Lett.***95**, 233302 (2009)

Publication

International Journals

1. J. Y. Kim, H. Lee, J. H. Park, D. Lee, **H.-J. Song**, J. Kwak, C. Lee, "Effect of Sol-Gel Derived ZnO Interfacial Layer on the Photovoltaic Properties of Polymer Solar Cell", *Japanese Journal of Applied Physics* **51**, 10NE29 (2012)

2. T. Kim, H. Yoon, **H.-J. Song**, N. Haberkorn, Y. Cho, S. H. Sung, C. Lee, K. Char, P.Theato,"Toward Mass Producible Ordered Bulk Heterojunction Organic Photovoltaic Devices", *Macromolecular Rapid Communications* **33**, 2035 (2012)

3. **H.-J. Song**, J. Y. Kim, D. Lee, J. Song, Y. Ko, J. Kwak, and C. Lee, "Origin of the Mixing Ratio Dependence of Power Conversion Efficiency in Bulk Heterojunction Organic Solar Cells with Low Donor Concentration", *Journal of Nanoscience and Nanotechnology* **13**, 7982 (2013)

4. M. Thambidurai, J. Y. Kim, J. Song, Y. Ko, **H. -J Song**, C. -M. Kang, N. Muthukumarasamy, D. Velauthapillaic and C. Lee "High performance inverted organic solar cells with solution processed Ga-doped ZnO as an interfacial

electron transport layer", *Journal of Material. Chemistry. C*, **1**, 8161 (2013)

5. K. Jung*, **H. -J. Song***, G. Lee, Y. Ko, K. Ahn, H. Choi, J. Y. Kim, K. Ha, S. Song, J. -K. Lee, C. Lee and M. Choi, "Plasmonic organic solar cells employing nanobump assembly via aerosol-derived nanoparticles", *ACS Nano*, **8**, 2590, (2014) *: Those authors are equally contributed.

6. M. Thambidurai, J. Y. Kim, C. -M. Kang, N. Muthukumarasamy, **H. -J. Song**, J. Song and C. Lee "Enhanced photovoltaic performance of inverted organic solar cells with In-doped ZnO as an electron extraction layer", *Renewable Energy*. **66**, 433, (2014)

7. M. Thambidurai, J. Y. Kim, Y. Ko, **H.-J. Song**, H. Shin, J. Song, Y. Lee, N. Muthukumarasamy, D. Velauthapillai, C. Lee, "High-efficiency inverted organic solar cells with polyethylene oxide-modified Zn-doped TiO2 as an interfacial electron transport layer", *Nanoscale* **6**, 8585 (2014)

8. **H.-J. Song**, J. Y. Kim, Y. Kwon, Y. Ko, D. Lee, H. J. Syn, J. Song, J. Kwak, C. Lee, "Improvement in the efficiency of organic solar cells using a low-temperature evaporable optical spacer", *Japanese Journal of Applied Physics* **53**, 08NJ04 (2014)

9. M. Thambidurai, J. Y. Kim, **H.-J. Song**, Y. Ko, N. Muthukumarasamy, D. Velauthapillai, V. W. Bergmann, S. A. L. Weber and C. Lee, "Enhanced power conversion efficiency of inverted organic solar cells by using solution processed Sn-doped TiO2 as an electron transport layer", *Journal of Materials Chemistry A* **2**, 11426 (2014)

10. **H.-J. Song***, G. Lee*, K. Jung, J.-K. Lee, M. S. Jang, J.–H. Sohn, M. Choi, C.

Lee “Comphrehensive analysis of Nanobump structure for efficient plasmonic organic solar cells”, *Nanoscale* ,To be submitted *: Those authors are equally contributed.

11. **H.-J. Song**, J. Roh, and C. Lee, “Phase separation in bulk heterojunction organic photovoltaic cells induced by substrate heating and controlling mixing ratio”, *Journal of Nanoscience and Nanotechnology,* Submitted

12. **H.-J. Song**, H. Lee, G. Lee, M. Choi and C. Lee, “Ultra-thin, dopant free, all vacuum processed highly efficient organo-metal halide perovskite solar cells”, *Applied Physics Letter,* To be submitted

한글초록

빛의 파장보다 작은 금속 나노 입자 및 구조체는 빛과 상호작용을 통해 입자 주변에 특정 파장의 전기장을 변화시키는 플라즈모닉스 효과가 나타난다. 이러한 플라즈모닉스 현상을 유기 박막 태양전지에 적용하여 유기 박막에서 광 흡수를 증가하고자 하는 많은 연구가 이루어져왔다. 하지만 대부분의 기존 연구는 용액 공정이 가능한 박막에 나노 입자를 함께 넣는 방식이라 막내 금속 입자 분포 제어에 한계가 있었다. 또한 나노 입자간의 결합을 방지하기 위해 입자를 다른 물질로 둘러쌓아야만 하는 문제가 발생한다. 이에 본 논문에서는 에어로졸 방식으로 형성되어 입자의 크기와 분포 조절이 용이한 나노 입자와 이로 발생하는 플라즈모닉 현상이 광 흡수층으로 잘 전달되기 위해 높은 굴절률을 가진 몰리브덴 산화물로 형성된 나노범프 구조를 이용한 고 효율 태양전지 구현 방법에 대해 연구하였다.

나노범프 구조를 적용한 유기 태양전지는 (효율 6.07%)나노 입자가 용액공정에 가능한 고분자 정공 수송층에 포함된 경우 (효율 5.63 %)효율 대비 더 높은 에너지 변환 효율을 나타낸다. 이러한 효율 개선은 나노범프구조에 의해 증가되는 광 흡수 파장이 (~550 nm) 고분자에 포함된 나노 입자대비 (~400nm) 장 파장쪽 더 강한 크기로 이동된다. 광학 계산 결과 높은 굴절률과 타원 모양의 나노범프 구조로 인하여 증가된 입사광의 전기장이 태양전지 내부로 넓은 범위에 전달되는 현상이 나타났다. 또한 나노범프 구조의 경우 나노 입자가 금속 산화물로 완전히 둘러 쌓여서 엑시톤의 수명이

나노입자로 인해 감소가 되지 않아서 생성된 엑시톤이손실없이 전하로 변환된다.

나노범프 구조에서 나노 입자의 크기를 변화시키면서 광학적, 전기적 특성을 연구한 결과, 나노 입자의 크기가 커짐에 따라 플라즈모닉 현상이 일어나는 파장이 장파장으로 이동되고 그 크기가 증가되는 현상을 관찰하였다. 즉 입자 크기 증가에 비례해서 생성되는 광 전류 상승이 나타났다. 이는 금속 입자의 크기가 증가됨에 따라 입자에서 발생하는 산란 비율의 증가에서 이루어졌다. 하지만 입자 크기 증가에 따라 입자와 음극 사이의 거리가 감소되어 이로 인한 누설 전류로 인해 태양전지 효율이 감소되었다. 이를 통해 40nm 크기의 나노 입자를 20nm 의 산화 몰리브덴 막으로 절연시킨 경우 최고 효율을 나타내는 특성을 발견하였다.

마지막으로 나노 입자 페시베이션 상태에 따른 전기적 광학적 특징을 40nm 금속 은 입자에서 산화 몰리브덴 막 두께를 변경해 가면서 분석해 보았다. 얇은 산화 몰리브덴 막으로 금속 입자의 일부가 고분자 층에 노출된 경우 금속 입자에서 형성된 플라즈모닉 현상이 잘 전달되어 막 자체의 흡수도가 높게 나타난다. 하지만 생성된 엑시톤이 일부만 페시베이션 된 나노 입자에서 소멸되고, 전자-정공 사이에 재결합 손실이 증가되어 증가된 흡수가 광전류로 전달되지 못하는 문제점이 발생한다. 반면, 완전히 페시베이션 된 경우 광 흡수 증가는 일부만 페시베이션 된 경우 대비 낮으나 생성된 전하가 손실없이 추출되어 태양전지 효율 상승으로 연결되었다.

이러한 나노범프 구조를 적용한 플라즈모닉 유기 태양전지 대한 연구는 다양한 태양전지 종류에 적용이 가능하며, 나노 구조체를

통한 전기장 조절이 가능하여 광 통신, 디스플레이 소자, 센서 등으로 널리 사용될 것으로 예상된다.

주요어: 유기 태양전지, 플라즈모닉스, 광학설계, 금속 나노 입자, 나노범프 구조, 엑시톤 소멸, 재결합 손실, 다중반사, 에어로졸
학번: 2011-30238